THE UNIVERSITY *of* EDINBURGH

Investigations of Nuclear Reactions Relevant to Stellar γ-ray Emission

David James Mountford

Thesis submitted for the degree of
Doctor of Philosophy
at
The University of Edinburgh

September 2013

Abstract

The detection of γ-rays from explosive astrophysical scenarios such as novae provides an excellent opportunity for the study of on-going nucleosynthesis in the Universe. Within this context, this work has addressed an uncertainty in the destruction rate of the ^{18}F nucleus, thought to be the primary source of 511 keV γ-rays from novae. A direct measurement of the ^{18}F(p,α)^{15}O cross section has provided the opportunity to extract resonance parameters through the R-Matrix formalism. The inferred parameters of populated states in ^{19}Ne include the observation of a broad $^1/_2{}^+$ state, consistent with a recent theoretical prediction, which will have a significant impact on the rate of destruction of this γ-ray producing radioisotope.

The ^{18}O(p,α)^{15}N reaction follows similar nuclear and kinematic processes and is expected to occur in the hydrogen burning layers of AGB stars. Resonance widths have been extracted from a direct measurement in the region around a poorly constrained broad state close to the Gamow window. This has produced a new parameter set for future reference and provides new information on the reaction rate.

The complex R-Matrix formalism used in these analyses is a crucial tool in the study of nuclear astrophysics reactions, and many codes have been written to implement the complex mathematics. This thesis presents a comparison of two publicly available codes from the JINA collaboration and a code used extensively by the University of Edinburgh. For this, the recent results of the ^{18}F destruction reaction, presented here, have been used. A minor error was found within one of the codes, and corrected. The final parameters extracted, and the resulting cross sections calculations, are shown to be consistent between the three codes.

A further γ-ray line of interest at 1.809 MeV, characteristic of ^{26}Al decay, has been observed throughout the interstellar medium. If, however, this isotope is

formed in a known isomeric state, its decay bypasses the emission of this γ-ray, thus complicating the interpretation of observed γ-ray fluxes. To this end, an experiment has been carried out, providing proof of principle of a direct measurement of the ^{26m}Al(p,γ)^{27}Si reaction. The calculation of the isomeric intensity is presented here.

Lay Summary

The formation of the chemical elements can be traced back, through nuclear reactions, to several astrophysical phenomena. The earliest, and simplest, of these reactions was the fusion of protons and neutrons in the expanding gas following the Big Bang. This gas became the material from which the first stars were formed. It is similar reactions, fusing lighter elements into heavier ones, that power stars today. These stars will eventually evolve to the point that their lives end in one of many possible scenarios, including explosions such as novae and supernovae, which release energy and matter into the universe.

A number of observations show that these processes are continuing in the Universe today. The elements produced can be formed in stable or unstable configurations, and if they are unstable they inevitably adapt to a stable configuration in a process that is often accompanied by the emission of energy in a gamma-ray. This energy, observed through specifically designed telescopes, provides a monitor of the elements that are being produced and destroyed in the stars today. In order to understand these observations, the rates of production and destruction through nuclear reactions must be measured.

This thesis reports on the design, performance and results of some experimental procedures that address these questions. The destruction rate of ^{18}F, an unstable type of fluorine produced in stars, has been measured and it was found that this rate is likely to be higher than previously thought. Thus the abundance of this type of fluorine in stars is likely to be lower than previously expected and observations of gamma-rays associated with it are, therefore, less likely. Furthermore, this work has proved useful in a comparison of analysis tools, demonstrating consistency across many techniques. Confidence, therefore, has been maintained in many sets of experimental results obtained through the years. Finally, the unstable form of aluminium, ^{26}Al, is of great interest as the gamma-ray associated with it has been observed in our galaxy, and since it has a half-life

of only 700,000 years, this gives further evidence for the present activity of the processes discussed above in the solar system. The nucleus itself, however, can be formed in two similar but different configurations. Included here is the crucial contribution of distinguishing between each form in the study of the destruction of this nucleus.

Declaration

I declare that this thesis was composed by myself, that the work contained herein is my own except where explicitly stated otherwise in the text, and that this work has not been submitted for any other degree or professional qualification except as specified.

Parts of this work have been published in [1].

(*David James Mountford, September 2013*)

Acknowledgements

First of all, I must thank my supervisor, Dr. Alex Murphy. Without his inspiring me to move into nuclear physics and his constant support and advice, I would not be where I am today. In addition, my thanks go to every member of the nuclear group, particularly Tom Davinson, Phil Woods and Gavin Lotay who have all contributed to the work in this thesis and who without it would not have been possible. I also thank my collaborators and friends from other institutions for their contributions and support while making conferences and summer schools as entertaining as they could be.

So to the students of the nuclear group, thank you to all for indulging my distractions, and for providing the required light relief, deliberately or otherwise. In particular, Daniel Doherty, Jennifer Wallace, Helena David, Lea Reichhart, Philip Salter, Pauline Hall-Barrientos, David Scott, Jamie Fleming and Chris Murphy (may as well be a student) who have made office life a lot more fun than its supposed to be! Elsewhere in the dark corridors of JCMB, thanks to Ben Wynne, James Carrington, Craig Wilson and Andy Schofield for turning 11am coffee break into essentially lunchtime! I would also like to thank every member of E=MCC for all the booze and cricket fuelled fun!

Thank you to my oldest and closest friends: Bruce Golding, Katherine Golding, Mike Thorpe, Anna Jordanous, Siobhan Liddle, Donna Morton, Katie Davies and Cheryl Lowans. Your support has meant a lot through these past four years and more, without it my mind would be weaker and my liver would be stronger!

I thank my family, particularly Mum, Dad and Chris, for their unyielding support and understanding during the past four years and the last few months in particular. Last but not at all least, to Alison. Thank you for all your support in the past few years and putting up with me while I get this thing finished, I could not have done it without you. Onto the next challenge!

Contents

List of Figures

List of Tables

Chapter 1

Introduction to Nuclear Astrophysics

"All we ever see of stars are their old photographs."

- Alan Moore, Watchmen

1.1 Introduction

The observation of γ-rays in the interstellar medium, by space-borne telescopes such as INTEGRAL, is a clear indication of ongoing nucleosynthesis in the Universe [2]. While they are yet to be observed, 511 keV γ-rays are expected from nova explosions, generated by the β^+ decay of ^{18}F that is produced through the ^{17}O(p,γ)^{18}F reaction in hydrogen burning and the decay of ^{18}Ne in explosive scenarios. Destruction of ^{18}F proceeds through the ^{18}F(p,α)^{15}O and ^{18}F(p,γ)^{19}Ne reactions in both quiescent and explosive hydrogen burning. Since the two ^{18}F+p reactions have the largest impact upon ^{18}F synthesis, and hence γ-ray detectability, from nova explosions [3], achieving a better determination of the ^{18}F(p,α)^{15}O reaction forms a substantial part of this thesis.

The data collected were in the form of nuclear excitation functions, the interpretation of which is significantly aided by the R-Matrix formalism. This allows the complex parameterisation of the strong nuclear binding force to be bypassed in the estimation of the extracted resonance parameters. This formalism

and its implementation has been studied by myself in collaboration with the JINA group at the University of Notre Dame. Making use of the data extracted in the direct measurement of the ^{18}F(p,α)^{15}O reaction presented here, three implementation codes used in the nuclear astrophysics community are compared. This is a crucial task to give confidence to past, present and future studies making use of these techniques.

The first observation of γ-rays confirming ongoing nucleosynthesis was the observation of the 1809 keV γ-ray associated with the β^+ decay of ^{26}Al to an excited state of ^{26}Mg [4]. This system is complicated by the existence of a low-energy isomeric state in ^{26}Al, from which a decay directly to the ground state of ^{26}Mg is much more favourable, bypassing the emission of the γ-ray. It has been suggested that the two associated radiative capture reactions, on the ground and isomeric states, responsible for the destruction of ^{26}Al, should be entered into reaction network codes separately.

The first direct measurement of the ^{26m}Al(p,γ)^{27}Si reaction has been carried out with the DRAGON experiment at TRIUMF and the process of normalisation forms the final part of this thesis.

1.2 Stellar Evolution

Given that the motivation for the nuclear reaction studies in this thesis come from the observation of γ-rays emitted from explosive astrophysical scenarios, it is appropriate to summarise the processes building up to these. In the following sections, nucleosynthesis stages are described through the evolution of the Universe from soon after the big bang to the relevant final scenarios for this work.

1.2.1 The Hertzsprung-Russell Diagram

In 1914, a survey of stars by astronomers Hertzsprung and Russell found that the relationship between the surface temperature and luminosity of a star was not a uniform distribution as had been previously expected [5]. Instead, they found some very distinct features on the scatter plot that would become known as the Hertzsprung-Russell (HR) Diagram, shown in figure 1.1.

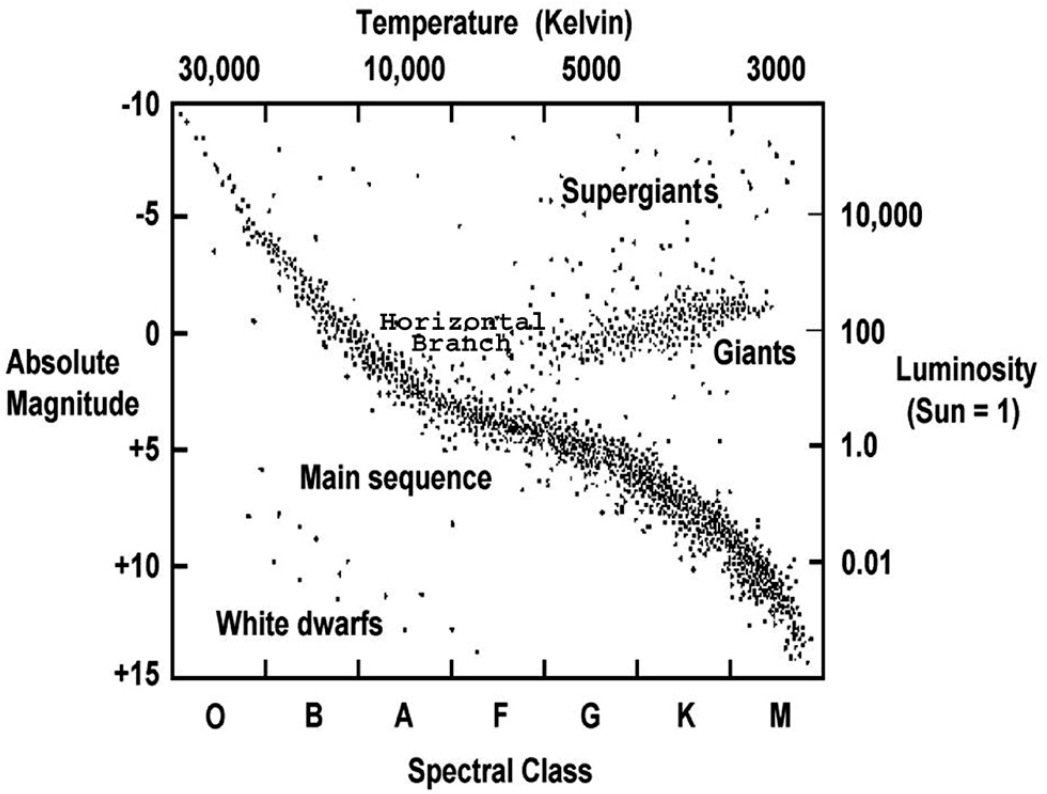

Figure 1.1 *The Hertzsprung-Russell diagram showing the relationship between luminosity and temperature of a star. The diagram can be used to explain the (expected) life cycle of every star in the universe.[6]*

Over time, it became apparent that stellar evolution, through a number of stages of nucleosynthesis, could explain the features of the HR diagram.

1.2.2 Before the Stars

The idea of stellar nucleosynthesis was set out in the famous paper by Alpher, Bethe and Gamow [7]. They hypothesised that the elements must have been formed as a results of a gradual "building up process" of neutron captures. While it later became apparent that nucleosynthesis was not as simple as thought here, this early theory still holds for the early formation of hydrogen and helium. This early stage is summarised in figures 1.2 and 1.3.

The relevant stages of nucleosynthesis begin about 10^{-3} seconds after the big bang, at which point quarks have combined to form protons and neutrons, leaving a gas containing the nucleons, neutrinos, antineutrinos, electrons and positrons, plus, potentially, dark matter particles. Here, the temperature is

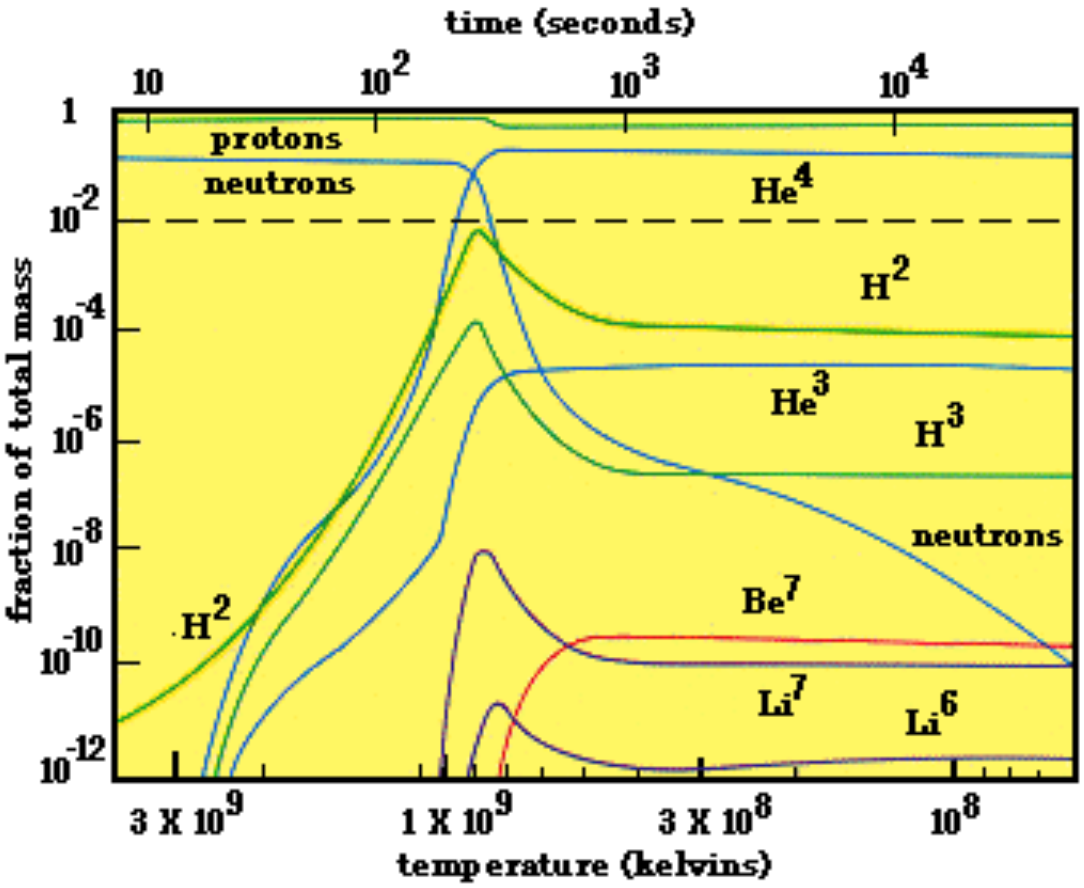

Figure 1.2 *Evolution of the constituents of matter in the universe as the temperature cools with time after the big bang. [8]*

about 10^{12} K and protons and neutrons are formed and destroyed through weak interactions, leading to a neutron to proton ratio of $\sim 2/5$ [10]. As the temperature reduces, the lower mass protons are more favourably formed and eventually, at around 7.5×10^9 K, the electron capture on protons slows to a halt, stopping the production of neutrons. This is the neutron "freeze-out" and the abundance ratio of neutrons to protons becomes $\sim 1/7$ [11].

Eventually, the temperature reduces so that heavier nuclei can begin to be formed without being immediately photo-disintegrated. At around 3×10^9 K, deuterium is formed through the fusion of protons and neutrons, see figure 1.2. From here, ever-heavier elements can be formed through capture and transfer reactions as the temperature continues to decrease. The full cycle is shown in figure 1.3.

This leads to a primordial gas cloud consisting of mainly hydrogen and helium, with the neutrons now absorbed into the helium ions. This gas cloud begins to collapse under gravity in localised regions. This collapse leads to increased

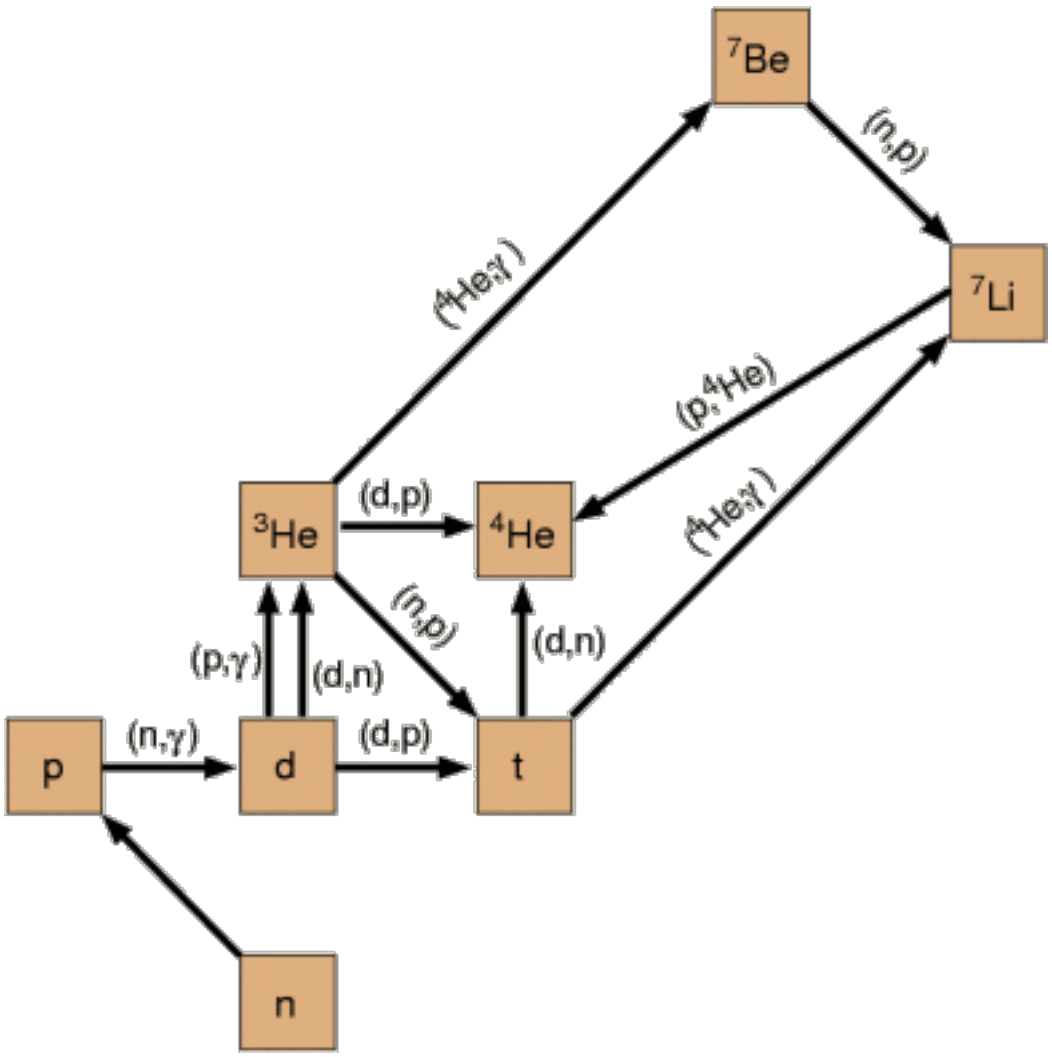

Figure 1.3 *The network of nuclear reactions leading to the nucleosynthesis described by figure 1.2. [9]*

density and temperature causing the cloud to become more and more opaque to its own radiation. Eventually, no more energy can radiate away from the fragment and the collapse halts due to thermodynamic equilibrium, leaving behind the beginnings of a star. The proto-star continues to accrete matter from the rest of the cloud, increasing the temperature until the hydrogen and helium have fully ionised [12, 13].

1.2.3 Hydrogen Burning

The formation of a star begins with this gas of hydrogen and helium. As more mass is accreted onto the surface, it continues to contract due to the additional gravitational potential energy. The conversion of this energy into thermal energy

keeps the protostar in hydrostatic equilibrium and when the temperature in the core reaches around 4×10^6 K, hydrogen burning begins [13] and a star is born. At this point the contraction halts as hydrostatic equilibrium is maintained through the energy produced by these fusion reactions. This ignition temperature is only attainable for stars which gain a minimum mass of around 0.08 $M_\odot$, below which the protostar will remain as a "brown" dwarf.

As hydrogen burning begins, the star appears on the main sequence on the HR diagram, figure 1.1. The burning then proceeds through one of two sequences. The higher the mass of the star, the faster the core heats up leading to a faster energy production and, through thermal equilibrium, a higher luminosity. The remnant of the initial hydrogen burning cycles is helium. The helium, however, is unable to fuse to the unburned hydrogen in the star as there is no stable mass five isotope [14].

The pp-chains

The net effect of the pp-chains is the fusion of four protons into an alpha particle making up to 26.731 MeV of energy available. The three chains are shown in the diagram in figure 1.4 and the first one follows the path given in equation 1.1,

$$p(p,e^+\nu)d(p,\gamma)^3He(^3He,2p)^4He. \tag{1.1}$$

The neutrino is produced with a fraction of the available energy in the hydrogen burning process, meaning the total energy available to the star is less than that stated above, 26.19 MeV on average [12]. If the star is massive enough, and enough thermal energy is garnered from the gravitational contraction, hydrogen burning can continue into the second or third chain where the ^{3}He and ^{4}He can fuse, as shown in equation 1.2,

$$p(p,e^+\nu)d(p,\gamma)^3He(^4He,\gamma)^7Be(e^-,\gamma)^7Li(p,\alpha)\alpha \tag{1.2a}$$

$$p(p,e^+\nu)d(p,\gamma)^3He(^4He,\gamma)^7Be(p,\gamma)^8B(e^+\nu)^8Be^*(\alpha)\alpha. \tag{1.2b}$$

While the average energy produced in the second chain is close to that produced in the first at 25.65 MeV, the production of another neutrino in the third chain

reduces the available energy to 19.75 MeV [12].

The CNO Cycle

The pp-chains are not the only possible process in hydrogen burning, however. If the star is from population I or II, that is not in the very first stars produced, population III, then it is likely to have heavier elements left over from previous evolutions. As such, an alternative mechanism of hydrogen burning can begin if the temperature in the core reaches around 15×10^6 K [13], the CNO-cycles [15]. There are three such cycles, shown in figure 1.5 and equation 1.3, featuring a series of proton captures and beta decays which have the same overall effect on the constituents of the star, the fusion of four protons into a helium ion with the release of some energy:

$$^{12}C(p,\gamma)^{13}N(e^+\nu)^{13}C(p,\gamma)^{14}N(p,\gamma)^{15}O(e^+\nu)^{15}N(p,\alpha)^{12}C \tag{1.3a}$$
$$^{14}N(p,\gamma)^{15}O(e^+\nu)^{15}N(p,\gamma)^{16}O(p,\gamma)^{17}F(e^+\nu)^{17}O(p,\alpha)^{14}N \tag{1.3b}$$
$$^{15}N(p,\gamma)^{16}O(p,\gamma)^{17}F(e^+\nu)^{17}O(p,\gamma)^{18}F(e^+\nu)^{18}O(p,\alpha)^{12}C \tag{1.3c}$$
$$^{16}O(p,\gamma)^{17}F(e^+\nu)^{17}O(p,\gamma)^{18}F(e^+\nu)^{18}O(p,\gamma)^{19}F(p,\alpha)^{12}C. \tag{1.3d}$$

The heavy elements of carbon, nitrogen and oxygen act as catalysts for the conversion of four protons into an alpha particle. Again, higher mass stars are able to enter higher cycles as larger Coulomb barriers are overcome.

Further Hydrogen Burning

In newer stars with high-mass seeds it is possible for hydrogen burning to proceed in even higher mass cycles with A$\geq$20 [16]. This further hydrogen burning requires a high initial mass to provide enough energy through gravitational contraction for these reactions to be energetically enabled.

1.2.4 Helium Burning and the Formation of Giants

Energy production in the core slows to a halt as hydrogen burning ends. Hydrostatic equilibrium is maintained by further gravitational contraction of the

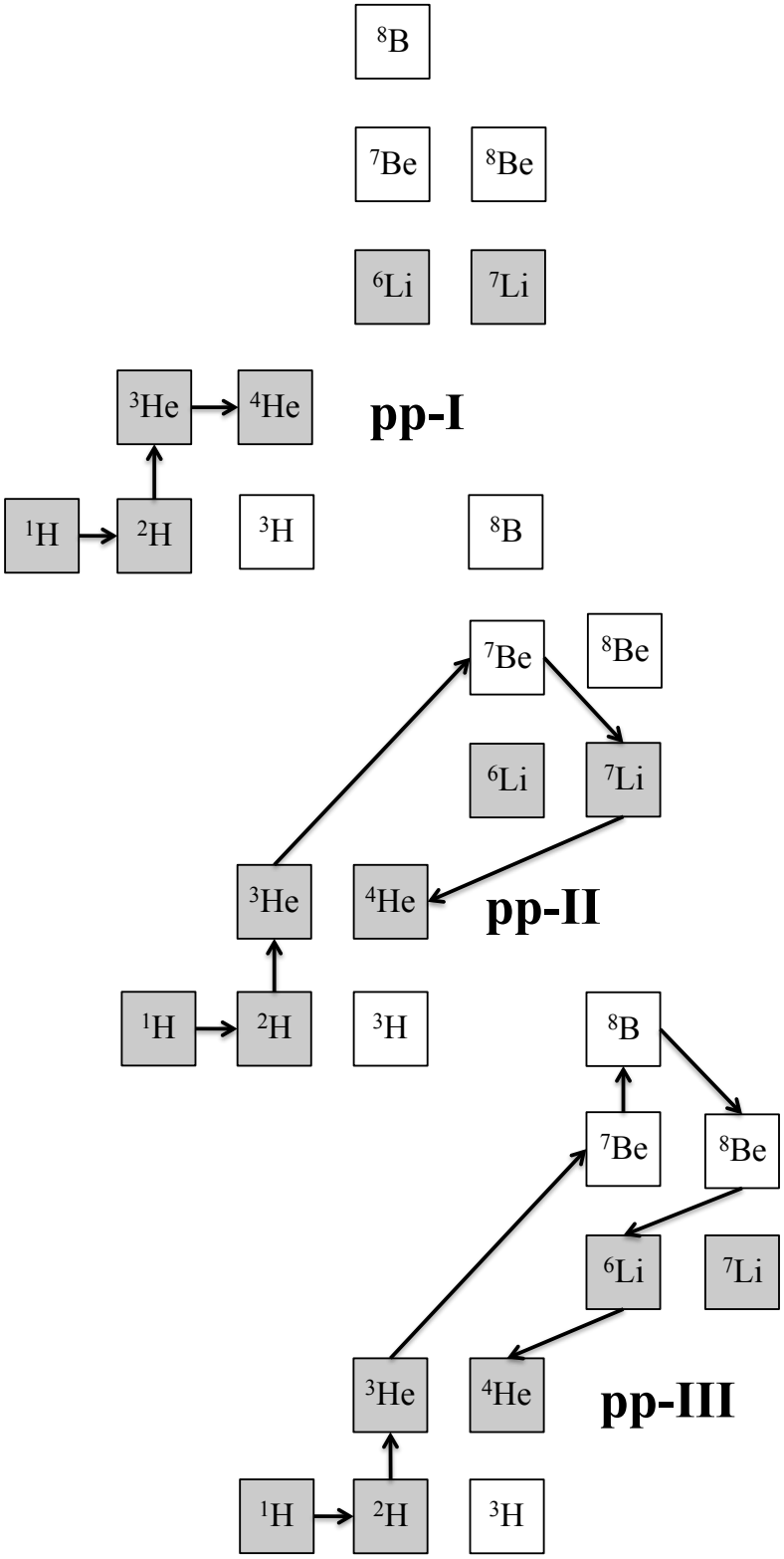

Figure 1.4 *The reaction networks constituting the early stages of stellar nucleosynthesis, the pp-chains.*

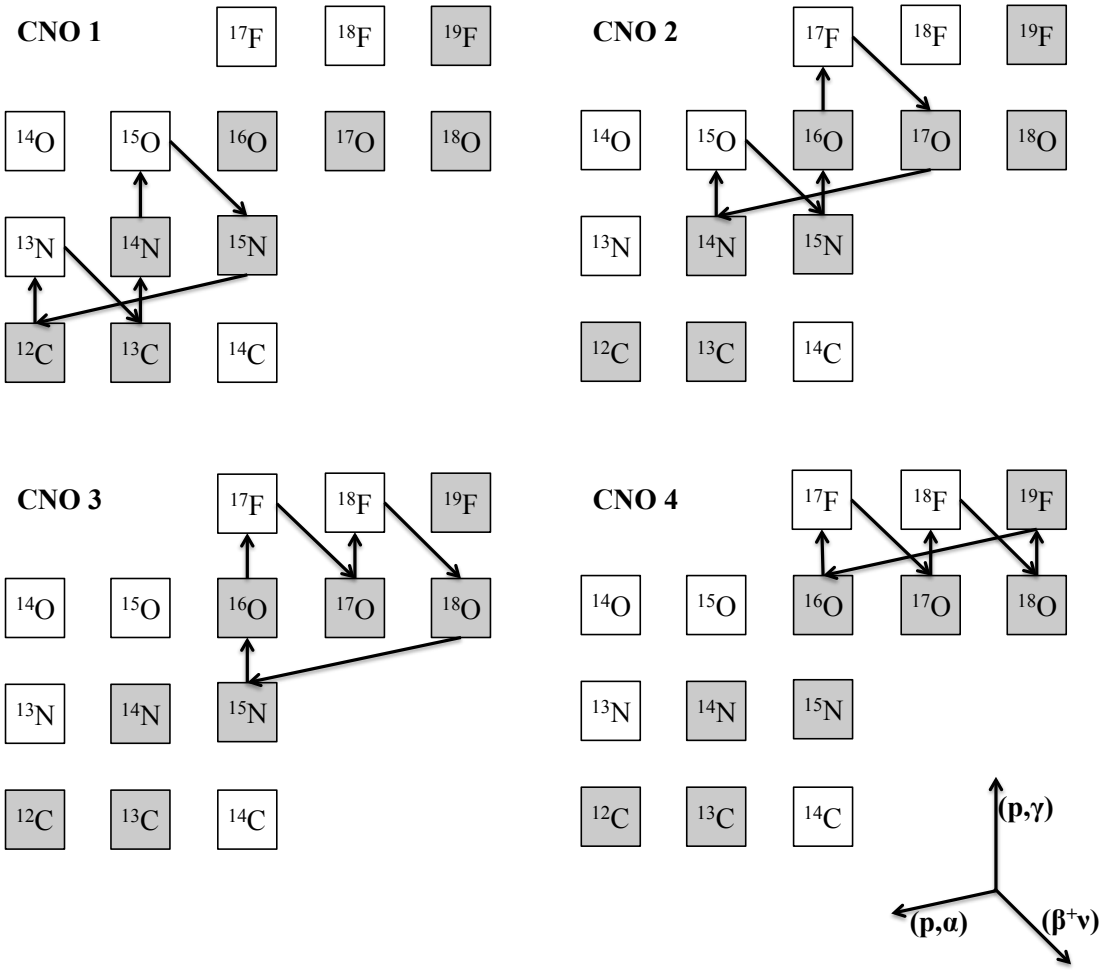

Figure 1.5 *The CNO cycles, so named due to their seed nuclei; carbon, nitrogen and oxygen. These form the latter stages of hydrogen burning in almost all stars of population-II and later.*

core, converting gravitational potential energy into thermal energy, increasing the temperature of the core until sufficient for the next stage of nucleosynthesis to begin, helium burning. During this contraction the core heats up, radiating this heat into the adjacent shells of hydrogen. This causes these shells to expand.

As the star's surface moves further from the heating core it will cool, while also increasing its surface area. This results in a decreased surface temperature and increased luminosity from the hydrogen burning reactions in the shell and, hence, the star is now located in the "giants" area of the HR Diagram. At this first stage, the star is known as a "red giant", referring to the relatively cool and, therefore, red surface [11].

Once the core reaches a temperature of around 10^8 K [10], the triple alpha process begins [15]. Firstly ^{8}Be is formed from the fusion of two ^{4}He isotopes. This is

strongly unbound, with a half-life of $\sim 10^{-17}$ s [17], and disintegrates rapidly to two alpha particles again. There is, however, a small, non-negligible probability of the ^{8}Be capturing another alpha particle to form ^{12}C. ^{12}C could then either disintegrate back to alpha particles and ^{8}Be isotopes or de-excite to the ^{12}C ground state. The abundance of carbon in the universe implies the latter occurs at a significant rate.

Famously, Sir Fred Hoyle FRS was able to calculate the required properties of a state which could be populated by alpha capture on the ^{8}Be nucleus and would then be likely to de-excite to the ground state and leave the observed abundance of carbon [18]. He deduced that there must exist a $J^{\pi}=0^{+}$ resonance at an excitation energy of 7.65 MeV which would emit a γ-ray in de-exciting to the 4.44 MeV 2^{+} resonance and then to the ground state or by pair production directly to the ground state. This state was observed experimentally soon after [19], although studies continue to obtain a full understanding of its properties [20, 21].

At high enough temperatures in the core, much like in hydrogen burning, further helium burning is also possible where helium is captured by the carbon to form oxygen and then neon and so on. Depending on the age of the star and the environment in the core, isotopes as heavy as ^{24}Mg can be synthesised in this process [22].

Once helium burning has discontinued in the core, it will, once again, contract. The same effect is seen as after hydrogen burning finished with the core heating and the outer shells, now hydrogen and helium, expanding. The helium shell also continues to burn providing energy to the cooling surface, moving the star back into the giant region of the HR Diagram. This path is almost perfectly parallel to the previous red giant path and so is named the Asymptotic Giant Branch, or AGB, and the star is known as an "AGB Star" [11]. This process, as it is expected to continue for our Sun, is shown in figure 1.6.

For all stars of initial mass up to about 8 $M_{\odot}$, and some more massive stars of up to 11 $M_{\odot}$, further gravitational contraction is not sufficient for further burning to take place [12]. This is the beginning of the end of the star's evolution.

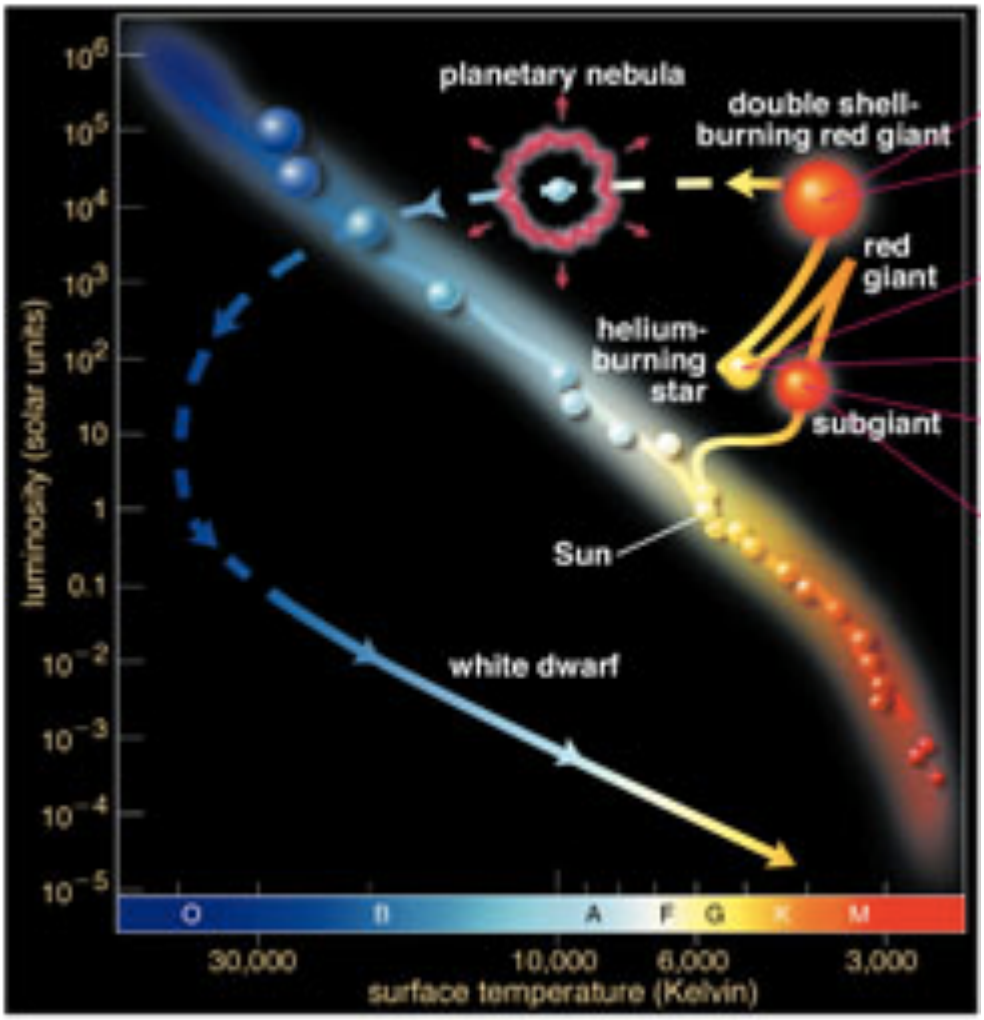

Figure 1.6 *The expected path of our Sun through the HR diagram[23]*

1.2.5 White Dwarves

Once all fusion has finished in the star, leaving only remnants behind, the star will again contract to maintain hydrostatic equilibrium. It can now be thought of as just a core as it is made up of the same constituents across its whole mass.

As gravitational contraction becomes insufficient to allow further nuclear reactions, no additional energy is provided to the surface, and hence, the luminosity of the star decreases. Eventually, the contraction is halted as hydrostatic equilibrium is maintained by electron degeneracy pressure. At this point, the electrons now occupy the lowest energy states possible and so cannot be compacted any more, this degeneracy pressure acts against the gravitational contraction. The contraction ceases and the inert star slowly cools. As such it now occupies the bottom left region of the HR Diagram and is a "white dwarf" [11]

with reference to its "white hot" appearance with temperatures of more than 10^4 K on the surface.

Stars of initial mass less than 0.4 $M_\odot$ cease nuclear burning after hydrogen burning and so become helium white dwarves. Stars heavier than this, up to about 11 $M_\odot$ will have completed helium burning, and as such consist of carbon, oxygen, neon and magnesium in some combination. The heavier the star, the higher mass the elements.

These heavier stars will have lost a lot of their mass through a solar wind at the AGB stage of their evolution. This contributes to the increased surface temperature by stripping away shells and exposing higher temperature matter. As a result, the white dwarf has a significantly smaller mass than the early age star from which it evolved. Indeed, as a white dwarf is supported by electron degeneracy, it can only exist up to a certain mass. This mass was calculated to be 1.44 $M_\odot$, the Chandrasekhar limit [24].

1.2.6 Core Collapse Supernovae

Stars evolving from an initial mass of more than around 8 $M_\odot$ can continue burning fuel beyond the helium burning stage. As more burning is ignited the star will evolve into an onion-like structure with many shells comprising gas at different burning stages, as shown in figure 1.7. The surface remains as hydrogen yet to ignite, with progressively heavier burning stages throughout the star to its core.

The final stage of nuclear burning to occur before collapse is silicon burning. The Coulomb barrier of ^{28}Si fusion is so high that photo-disintegration of the silicon occurs first, providing an abundance of α-particles. These α-particles are then captured by the heavier nuclei resulting in a building up process up to ^{56}Ni.

Relatively rapid electron capture processes then follow resulting in the formation of ^{56}Fe, the ash of silicon burning. Further nucleosynthesis is not possible due to ^{56}Fe having the highest binding energy of all isotopes. Higher mass ions can, however, be formed through the s-process, a series of relatively slow neutron captures and β^- decays [22], mainly occurring in AGB stars.

Eventually a star reaches the stage of an inert iron core with lighter mass burning occurring in the outer shells. As no more nuclear burning is taking

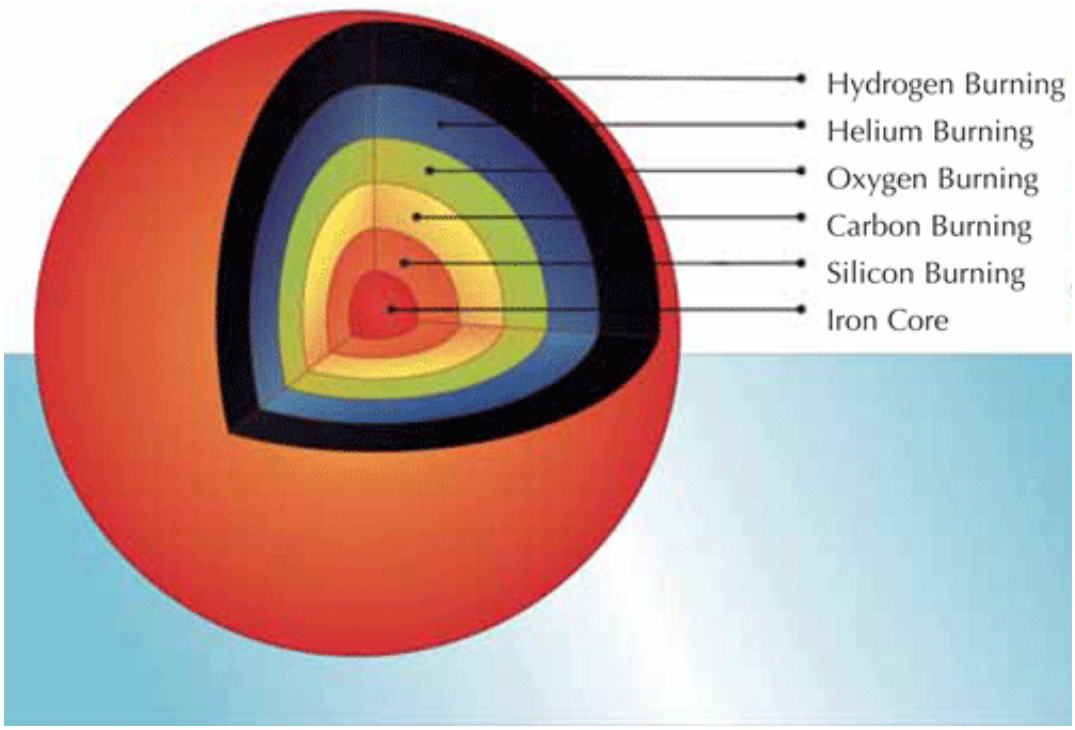

Figure 1.7 *The "onion" structure of a star upon completion of all stellar burning stages in the core prior to supernova explosion. Nuclear burning continues in the outer shells. Diagram not to scale.[25]*

place in the core of the star, it rapidly contracts, resulting in a dramatic increase in temperature and density, increasing the rate of electron capture on the iron nuclei and allowing photodissociation of the iron nuclei into neutrons and protons, reversing the previous nucleosynthesis. These processes absorb some of the thermal energy generated by the collapse which could provide an opposing pressure. The collapse increases in velocity until the dissociated nucleons will begin to feel the effects of the short range, repulsive, nuclear force. This results in a "bounce", driving a shock wave back through the star, further dissociating the matter in the core.

The shockwave is stalled by the in-falling matter from external shells until the neutrinos produced by the weak interactions in the core re-energise it, driving matter outwards once again. The shock wave continues travelling through the external shells of the star, igniting further nucleosynthesis at faster rates and higher energies than previous burning phases, triggering what is known as explosive nuclear burning. This will be discussed in the following sections.

The outer shells of the star are emitted into the interstellar medium by the explosion and what is left behind is a neutron star or, if the explosion is powerful

enough, a black hole. A neutron star is composed mostly of neutrons and is supported by neutron degeneracy pressure, much like the white dwarf is supported by electron degeneracy pressure [12].

1.2.7 Binary Stellar Evolution

The remnants of a full stellar evolution cycle of a single star still have a part to play in other astrophysical scenarios. Here, two such scenarios are discussed, with novae being of particular interest to this thesis.

Novae

Novae occur in binary stellar systems composed of a white dwarf and hydrogen-rich partner. Any star has a Roche lobe, defined as the region within which the star's material is gravitationally bound to that star. If a star expands outwith its Roche lobe, the material can escape into the interstellar medium. In a binary system, as shown in figure 1.8, the interaction of the two gravitational potentials leads to an almost tear drop shaped equipotential contour for the Roche lobe. The cross over of the combined Roche lobe is a saddle point between the two potential minima of the stars, this is defined as the inner Lagrange point. A Lagrange point is a stationary point of the combined potential. When the hydrogen burning partner to the white dwarf in this system expands towards its Roche Lobe, the surface material will pass through the inner Lagrange point to be captured in the gravitational potential field of the white dwarf. This is referred to as the accretion of matter to the white dwarf [26].

As hydrogen rich matter builds on the surface, some mixing occurs with the heavier elements in the white dwarf. This creates a shell of the white dwarf matter (carbon, oxygen, neon or magnesium) mixed with hydrogen. As the matter builds on the surface, this shell is compressed by gravitational contraction of the accreted matter acting against the surface of the white dwarf and so heats up. Eventually, the temperature reaches a point where a thermonuclear runaway is ignited and explosive hydrogen burning occurs [26].

This consists of the hot-CNO cycles synthesising ions of higher mass, which are defined in equation 1.4 and figure 1.11 [22]. In addition, relying on the presence of heavy seed nuclei from previous evolutions, further proton captures can occur

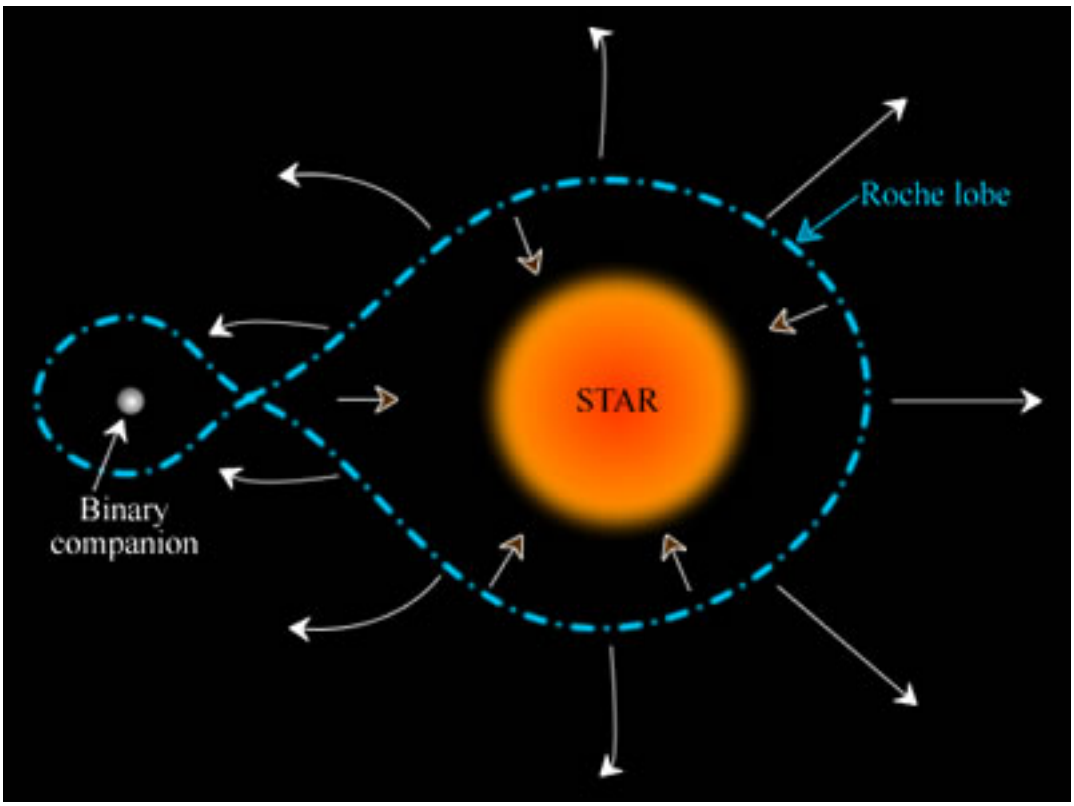

Figure 1.8 *The Roche lobes and equipotential contour of a binary stellar system leading to the accretion of matter to the binary companion [27]*

up to ^{33}Cl. These processes result in a rapid release of energy, blowing the surface matter into the interstellar medium. An example of an observed nova is shown in figure 1.10.

$$^{12}C(p,\gamma)^{13}N(p,\gamma)^{14}O(e^{+}\nu)^{14}N(p,\gamma)^{15}O(e^{+}\nu)^{15}N(p,\alpha)^{12}C \tag{1.4a}$$

$$^{15}N(p,\gamma)^{16}O(p,\gamma)^{17}F(e^{+}\nu)^{17}O(p,\gamma)^{18}F(p,\alpha)^{15}O(e^{+}\nu)^{15}N \tag{1.4b}$$

$$^{15}N(p,\gamma)^{16}O(p,\gamma)^{17}F(p,\gamma)^{18}Ne(e^{+}\nu)^{18}F(p,\alpha)^{15}O(e^{+}\nu)^{15}N. \tag{1.4c}$$

X-ray Bursts

In the case of an X-ray burst, matter is accreted onto the surface of a neutron star. This significantly smaller progenitor, of similar mass to a white dwarf, results in a greater gravitational potential on the accreting matter at the surface. It is so strong that as the temperature rises and nuclear reactions are ignited the matter is still bound to the surface. The energy is released in a sudden burst of X-rays,

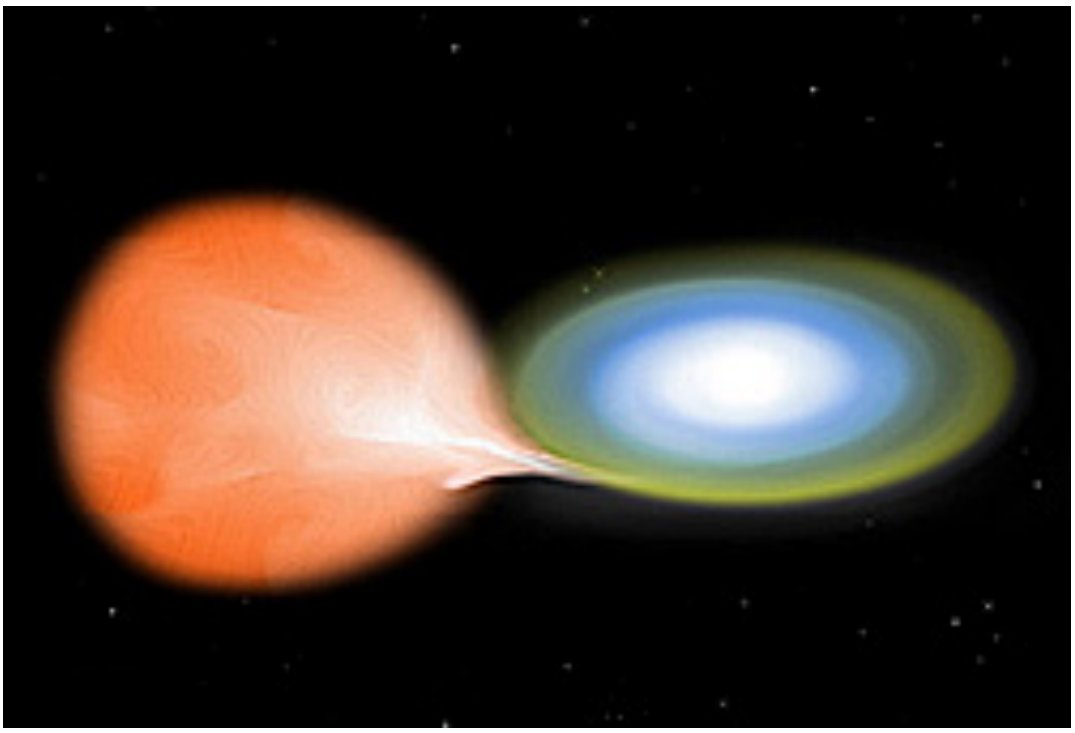

Figure 1.9 *An artist's impression of the accretion process leading to novae, type-1a supernovae and x-ray bursts.[28]*

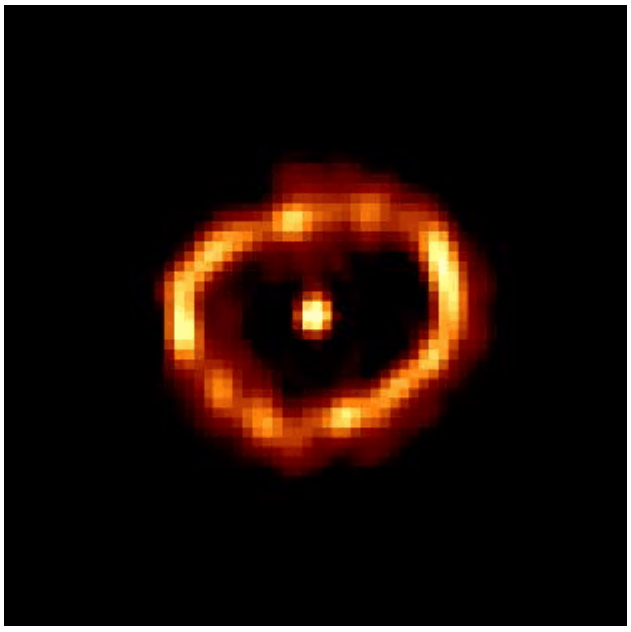

Figure 1.10 *Nova Cygni as observed by the Hubble Space Telescope[29]*

with no contribution of matter to the interstellar medium. As the underlying star remains undisturbed by the burst, another event can occur on the star within a timescale of a few hours making X-ray bursts the most common astrophysical explosion in the universe. Again, a more in depth discussion is available in [12].

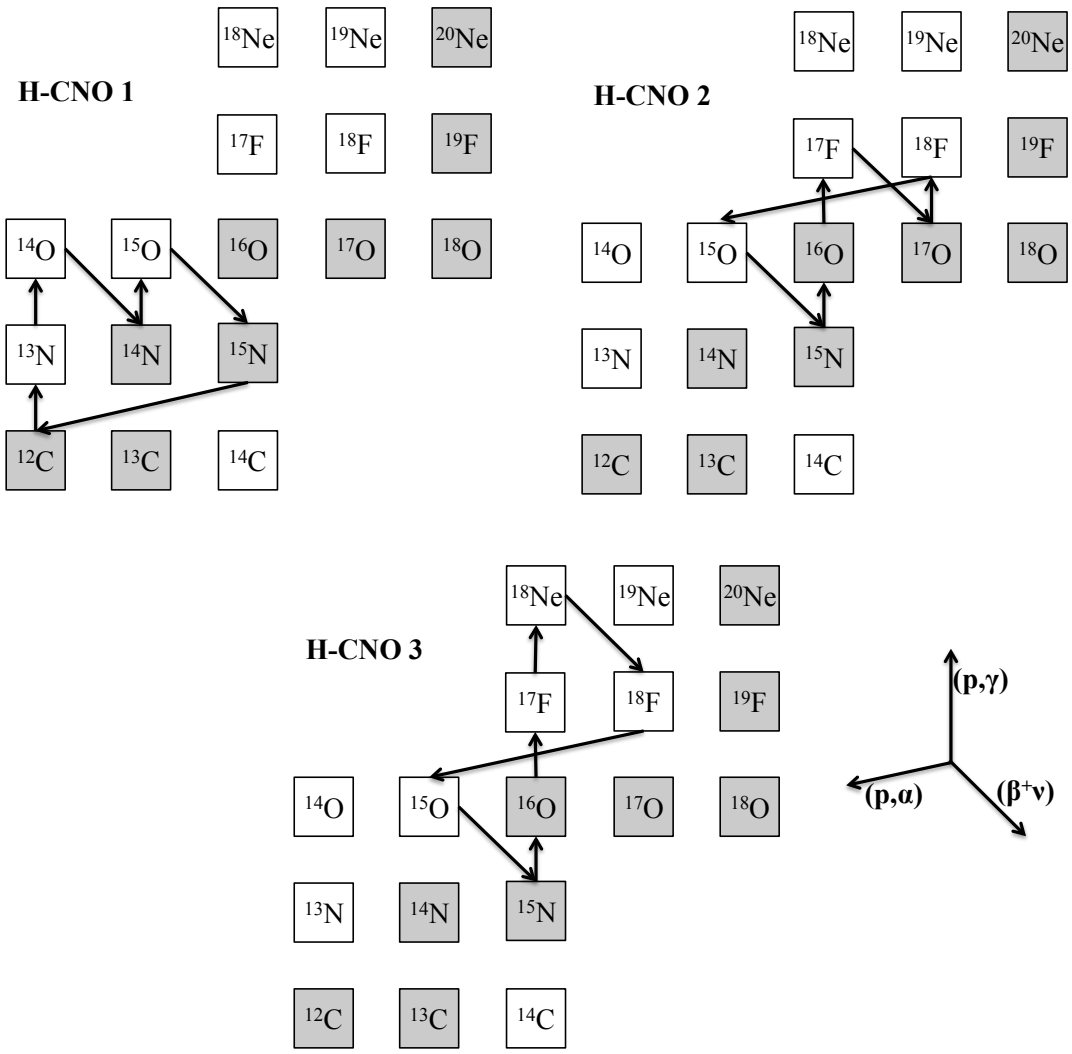

Figure 1.11 *The hot CNO cycles present in explosive stellar scenarios. Again, the seed nuclei are carbon, nitrogen and oxygen.*

Type 1a Supernovae

While there is no theory universally accepted for all type-1a supernova observations, the most commonly accepted explanation is similar to that of a nova, albeit significantly more energetic. This type of supernova is thought to be caused by the accretion of matter from a companion star to a carbon-oxygen white dwarf. At a critical mass of around 1.38 $M_\odot$ the degenerate carbon and oxygen rich matter in the white dwarf ignites and burns in a thermonuclear runaway. The white dwarf explodes and emits the burning matter into the interstellar medium [12].

Type 1a supernovae show a rapid increase in luminosity by reaching the peak of their light curves, $\sim 10^{10} L_\odot$ in about 20 days. This drops by about three orders of magnitude in the next 30 days before a longer decay is observed. These decays

are attributed to the presence of decaying ^{56}Ni in the ejecta. This decays to ^{56}Co with a half life of 6.1 days, followed by a decay to ^{56}Fe with a half life of 77.2 days [10].

Type 1a supernovae also show no hydrogen absorption lines in their light spectra, placing doubt over the nature of the companion star accreting matter to the white dwarf. A main sequence or red giant star is likely to accrete hydrogen rich matter [10]. One alternative explosion mechanism is double detonation where the accreted shell ignites, driving a shock wave into the white dwarf and causing a second ignition, detonating the core and causing the supernova explosion [30].

As no X-ray burst events have been observed in locations where a type 1a supernovae had previously occurred, it is thought that the white dwarf is fully ruptured by the explosion and no remnant is left behind [11].

1.2.8 Interstellar γ-ray Observations

Novae are the most common astrophysical explosion sites in the Universe and provide an excellent opportunity for the study of the nucleosynthesis of radioisotopes through detection of their gamma-ray emission.

511 keV γ-rays Following ^{18}F Decay

The current INTEGRAL satellite, figure 1.12, includes such an objective within its mission goals. A robust prediction of simulations of CO- and ONe-type novae events is that their gamma-ray emission will be dominated by the 511 keV gamma-rays produced by positron annihilation following the β^+ decay of ^{18}F [33]. Key reasons for the high flux are that this isotope is produced relatively abundantly, and its lifetime of $\sim$158 minutes [17] is well matched to the timescale for nova ejecta to become transparent to gamma-ray emission [34]. There remains however a large uncertainty on the absolute flux, and by implication the detectability distance for novae, because of uncertainty in the rates of the nuclear reactions producing and destroying ^{18}F, and most importantly ^{18}F(p,α)^{15}O [3].

This reaction is a key part of hot CNO cycles two and three, with production of ^{18}F occurring through the ^{17}O(p,γ)^{18}F reaction and the β^+ decay of ^{18}Ne. The uncertainty in the destruction rate of this nucleus through the ^{18}F(p,α)^{15}O reaction presents a limit to interpretation of any future observed gamma-ray flux.

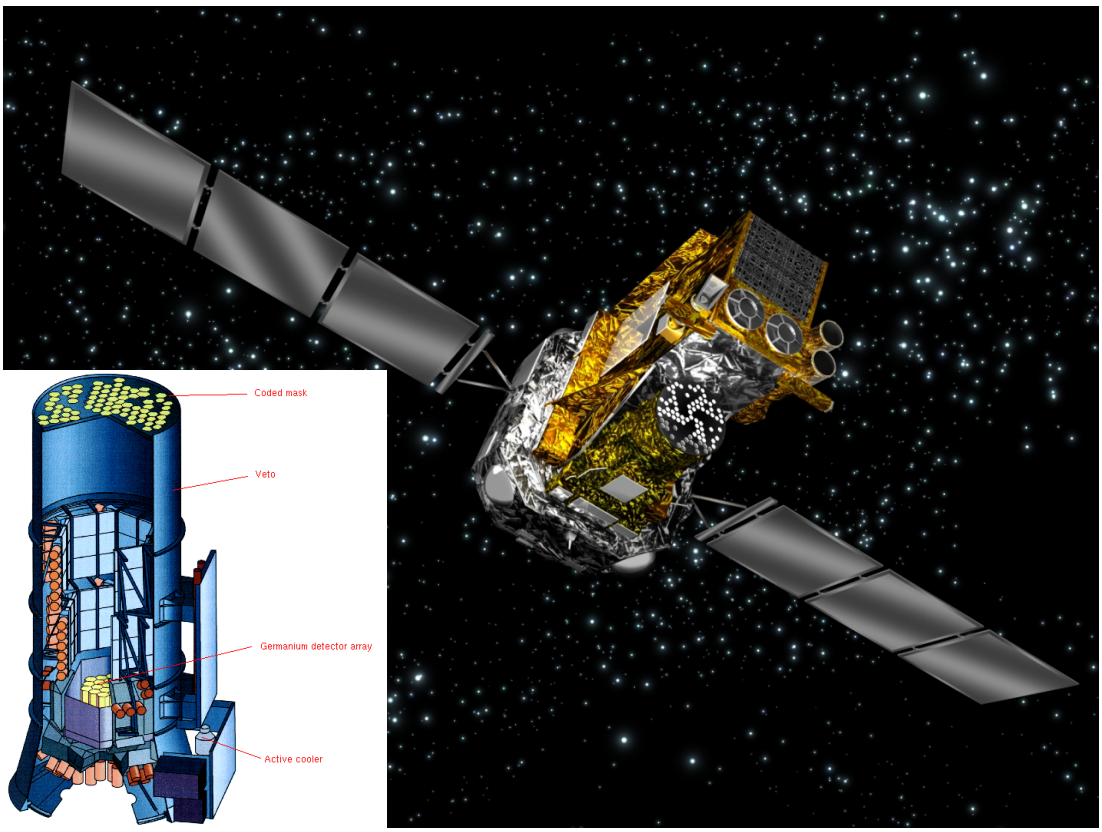

Figure 1.12 *ESA's space-borne INTEGRAL satellite [31]. Inset: The SPI component used for gamma-ray observations from sites such as novae [32].*

1809 keV γ-rays Following ^{26}Al Decay

The $J^{\pi}=5^{+}$ ground state of ^{26}Al decays via β^{+} emission to an excited state of ^{26}Mg, which in turn emits an 1809 keV γ-ray. An observation of this γ-ray by the HEAO-3 satellite in 1982 [4], coupled with the known half-life of the ^{26}Al at 7.5×10^{5} years, gave the first confirmation that nucleosynthesis was continuing in the Milky Way.

The characteristic gamma-ray line was again observed by the COMPTEL telescope [35], observing a non-uniform trend in emission location with sources grouped in localised locations. These data therefore favoured massive star evolution as the source of ^{26}Al, *i.e.* AGB stars and core-collapsed supernovae.

Finally, the measurements and implications were corroborated by the most accurate observation yet of the 1809 keV gamma-ray line, using the afore mentioned INTEGRAL satellite [36]. The observed spectrum is shown in figure 1.14.

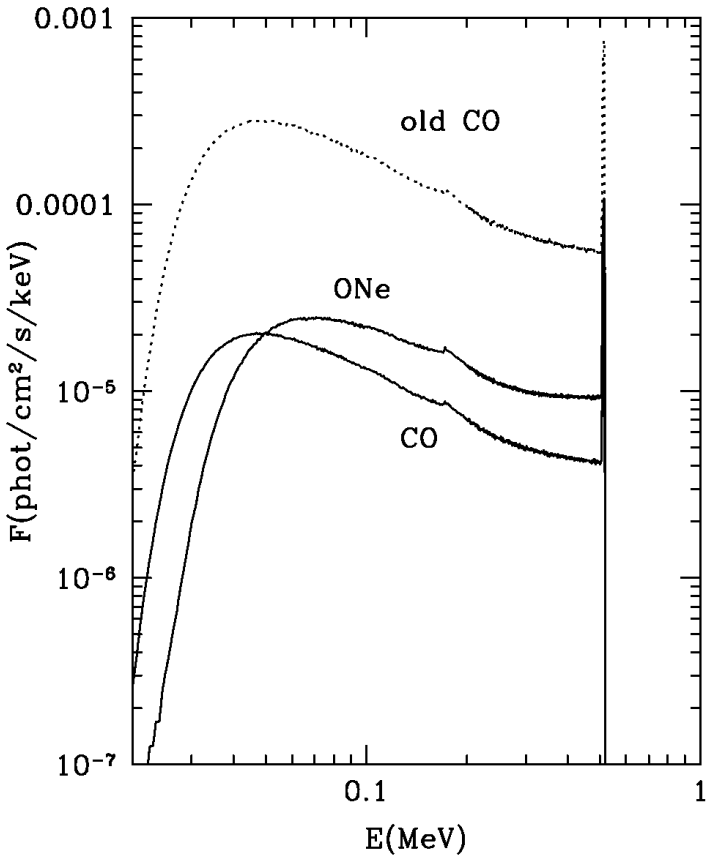

Figure 1.13 *Expected γ-ray energy spectrum from carbon-oxygen and Oxygen-neon novae as calculated by Hernanz* et al. *[33].*

In advanced hydrogen burning, ^{26}Al is formed and destroyed through direct proton capture, in addition to its decay. As such, the ^{26}Al(p,γ)^{25}Mg reaction has been studied extensively.

At around 228 keV above the ground state, ^{26}Al also exhibits a $J^{\pi}=0^{+}$ metastable state with a significantly shorter half life of only 6.3 s, which also β^{+} decays, but directly to the ground state of ^{26}Mg, thus bypassing the emission of the 1809 keV γ-ray. The large parity difference between this isomer and the ground state implies that populating the ground state from the isomer by γ-decay, and allowing the emission of 1809 keV γ-rays, is highly unlikely. Consequently, it has been suggested that the reaction rates of both the ^{26}Al(p,γ)^{25}Mg and ^{26m}Al(p,γ)^{25}Mg must be considered exclusively. Until now, only the ^{26}Al(p,γ)^{25}Mg reaction has been studied directly.

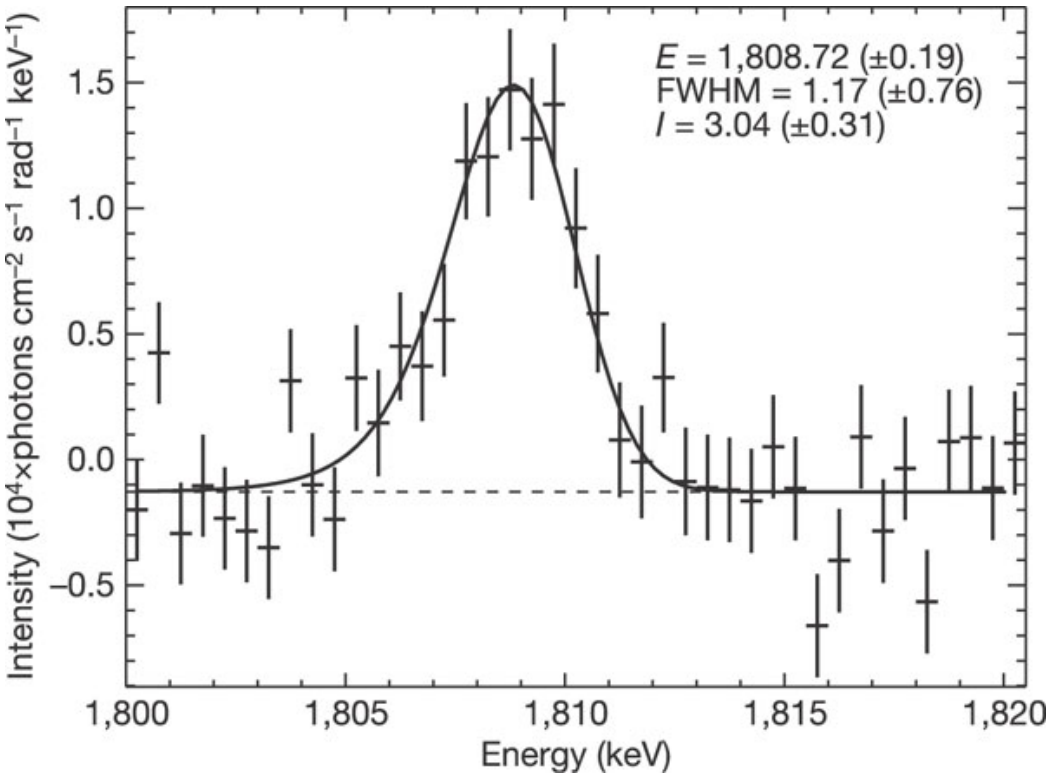

Figure 1.14 *The observed spectrum of γ-rays from ^{26}Al decay as observed by the INTEGRAL satellite [36].*

1.2.9 Other Stellar Abundance Observations

Further to the interstellar γ-ray observations discussed above, stellar abundances can also be measured from samples of meteorites [37]. Such meteorites contain dust grains that form in, and are ejected from, the outer envelopes of low-mass stars. Such measurements have provided further motivation for the study of ^{26}Al destruction due to the observation of a large ^{26}Al/^{27}Al ratio relative to the observed abundance of ^{26}Mg [38].

The current understanding of the rates of the ^{15}N(p,α)^{12}C and ^{18}O(p,α)^{15}N CNO cycle reactions, and the effect of these on current stellar nucleosynthesis models, is inconsistent with the, significantly lower, observed ^{14}N/^{15}N ratio from SiC grains thought to be formed during the AGB stage of the stellar evolution of low mass population I stars [37]. A possible explanation of this discrepancy lies in the poorly constrained rate of the ^{18}O(p,α)^{15}N reaction, if this rate was higher than currently thought the expected ^{14}N/^{15}N ratio would approach consistency with the lower value found from current models [39]. This is discussed further in chapter 2.

1.3 Nuclear Reaction Studies

The reactions of interest to nuclear astrophysics can be studied in laboratories around the world with the development of stable and radioactive beams and detector systems.

A nuclear reaction can be denoted by the simple relationship in equation 1.5 and shown schematically in figure 1.15.

$$a + X \rightarrow b + Y \tag{1.5a}$$

$$X(a, b)Y. \tag{1.5b}$$

The left side is defined as the entrance channel and the right side is the exit channel. In addition, these reactions are often studied in inverse kinematics where the heavier ion in the entrance channel is the beam, as is the case in the studies in this thesis. This can be preferable in the case where the heavy ion is radioactive, resulting in difficulty in its use as a target.

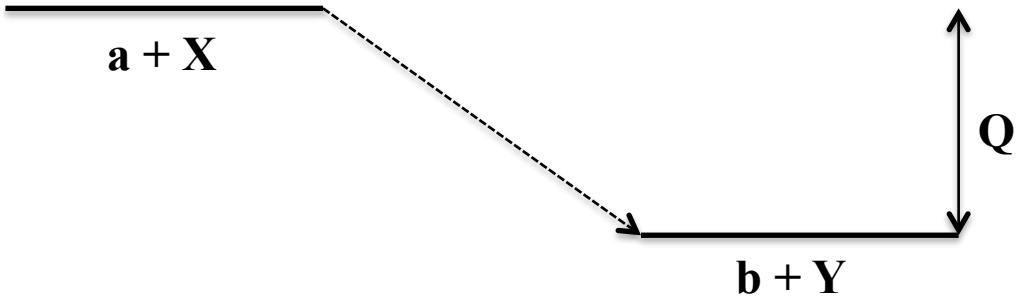

Figure 1.15 *Schematic representation of a direct reaction with nucleus a reacting with nucleus X to form b and Y with the emission of energy Q.*

1.3.1 Energy Production

If the ground state mass of the entrance channel ions can be denoted as M_a and M_X and the exit channel ions can be denoted as M_b and M_Y then the energy

produced in the reaction is given by equation 1.6, known as the Q-value:

$$Q = (M_a + M_X - M_b - M_Y)\, c^2. \tag{1.6}$$

A positive Q-value defines an energy producing reaction while a negative value defines a reaction which must be triggered by the provision of energy.

1.3.2 Reaction Cross Section

The reaction cross section is described as the probability of a reaction progressing and is defined as the number of reactions per incident particle per target nucleus. Geometrically, this can be thought of as being analogous to the cross section of the two interacting particles and so the reaction cross section is presented in terms of area.

1.3.3 Charged Particle Reactions

Non-resonant

As nuclei are positively charged, any reaction occurring between them will be hindered by the repulsive Coulomb force, with the potential defined in equation 1.7 and the form shown in figure 1.16.

$$V_C(r) = \frac{Z_1 Z_2 e^2}{r}. \tag{1.7}$$

This potential provides a barrier to interaction between two nuclei, that is to say that the probability of the wavefunctions of the nuclei overlapping within the combined nuclear radius is inhibited by this potential. This effective radius is given by $R_n = 1.25(A_1^{1/3}+A_2^{1/3})$ fm. At this point, the Coulomb potential is at a maximum and dissipates with increasing separation as shown in figure 1.16. Classically, the nuclei involved in the reaction must have enough energy between them to overcome the maximum of this potential. If this were the case, nuclear reactions would have a sudden onset in stars resulting in a relatively short explosion as opposed to slowly burning fuel over an extended period of time [11]. It was George Gamow [40] that showed that there was an energy dependant

probability of "tunnelling" through the Coulomb Barrier and allowing a slow onset of nuclear fusion with temperature increase in stars.

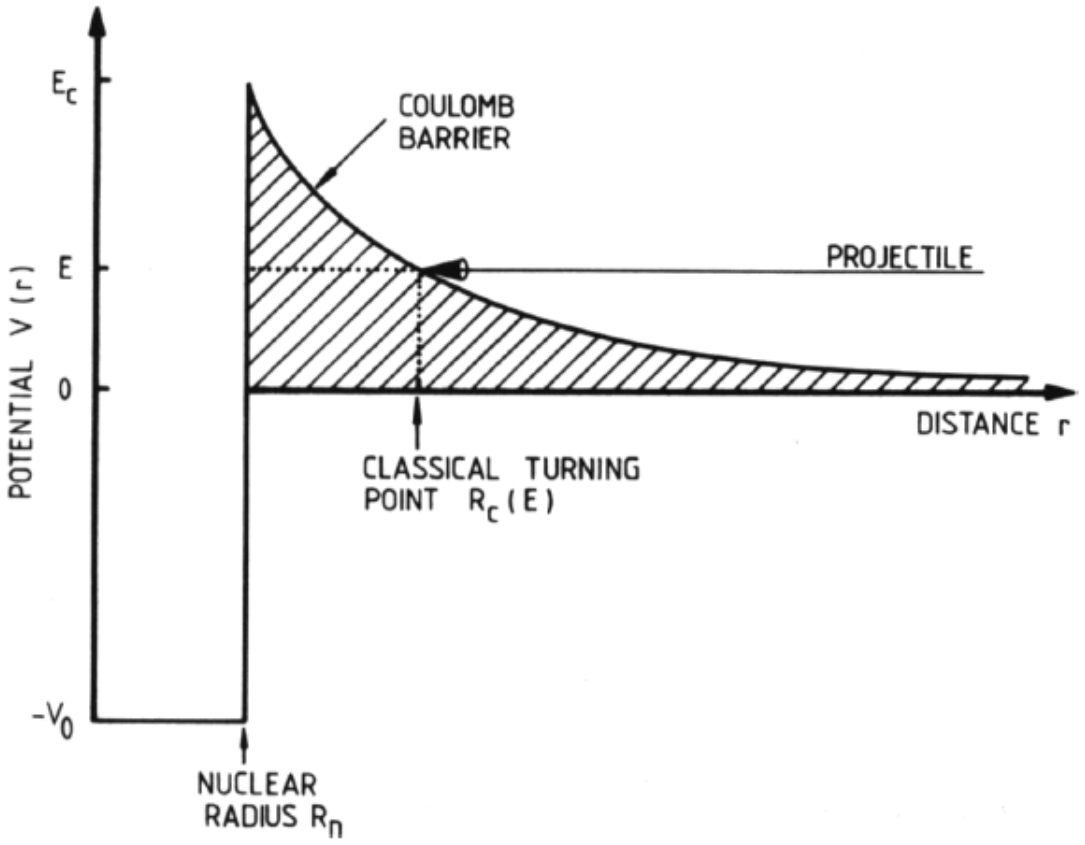

Figure 1.16 *The Coulomb barrier which must be overcome for any interactions to take place between two charged particles. The classical turning point denotes the distance of closest approach without quantum tunnelling effects. [11].*

The energy of nuclei in the stars can be replicated in the laboratory by accelerating a beam of particles to high speeds resulting in kinetic energy providing the required energy for the reaction to take place. If the projectile has energy E, the classical turning point, as shown in figure 1.16, is denoted R_C. The probability of a particle being found at this point is the square of the wavefunction at this radius, and similarly for the probability of a particle penetrating the barrier and being found at R_N. The probability of penetrating the barrier is the ratio of these two values and, by solving the Schrödinger equation, Gamow showed that the probability of penetrating the Coulomb barrier is given by equation 1.8.

$$P = exp(-2\pi\eta) \tag{1.8a}$$

$$2\pi\eta = 31.29 Z_1 Z_2 \left(\frac{\mu}{E}\right)^{1/2}. \tag{1.8b}$$

Here, μ is the reduced mass, defined as,

$$\mu = \frac{M_1 M_2}{M_1 + M_2}. \tag{1.9}$$

As the probability of penetrating the Coulomb barrier decreases, so must the probability of the reaction proceeding. As such the cross section scales linearly with this probability factor, dropping off significantly at energies below the Coulomb Barrier:

$$\sigma \propto exp(-2\pi\eta). \tag{1.10}$$

As noted previously, the cross section can be thought of as the geometrical area of the two reactants. As nuclear reactions are quantum mechanical processes, the geometrical nuclear radius can be replaced by the de Broglie wavelength which has a $1/E^{1/2}$ dependance. As such, the cross section must have a $1/E$ dependance in addition to its dependance upon the tunnelling probability. Therefore, the cross section can be written as in equation 1.11

$$\sigma(E) = \frac{1}{E} exp(-2\pi\eta) S(E). \tag{1.11}$$

This equation defines the astrophysical s-factor, S(E), which contains all the nuclear effects, and is often used in place of the cross section to report on nuclear reactions below the Coulomb Barrier. The usefulness of this quantity is shown in figure 1.17. As the cross section drops off dramatically, the s-factor stays relatively featureless.

Resonances

Instead of proceeding directly from the entrance channel into the exit channel, nuclear reactions can form a compound nucleus in an intermediate step if an

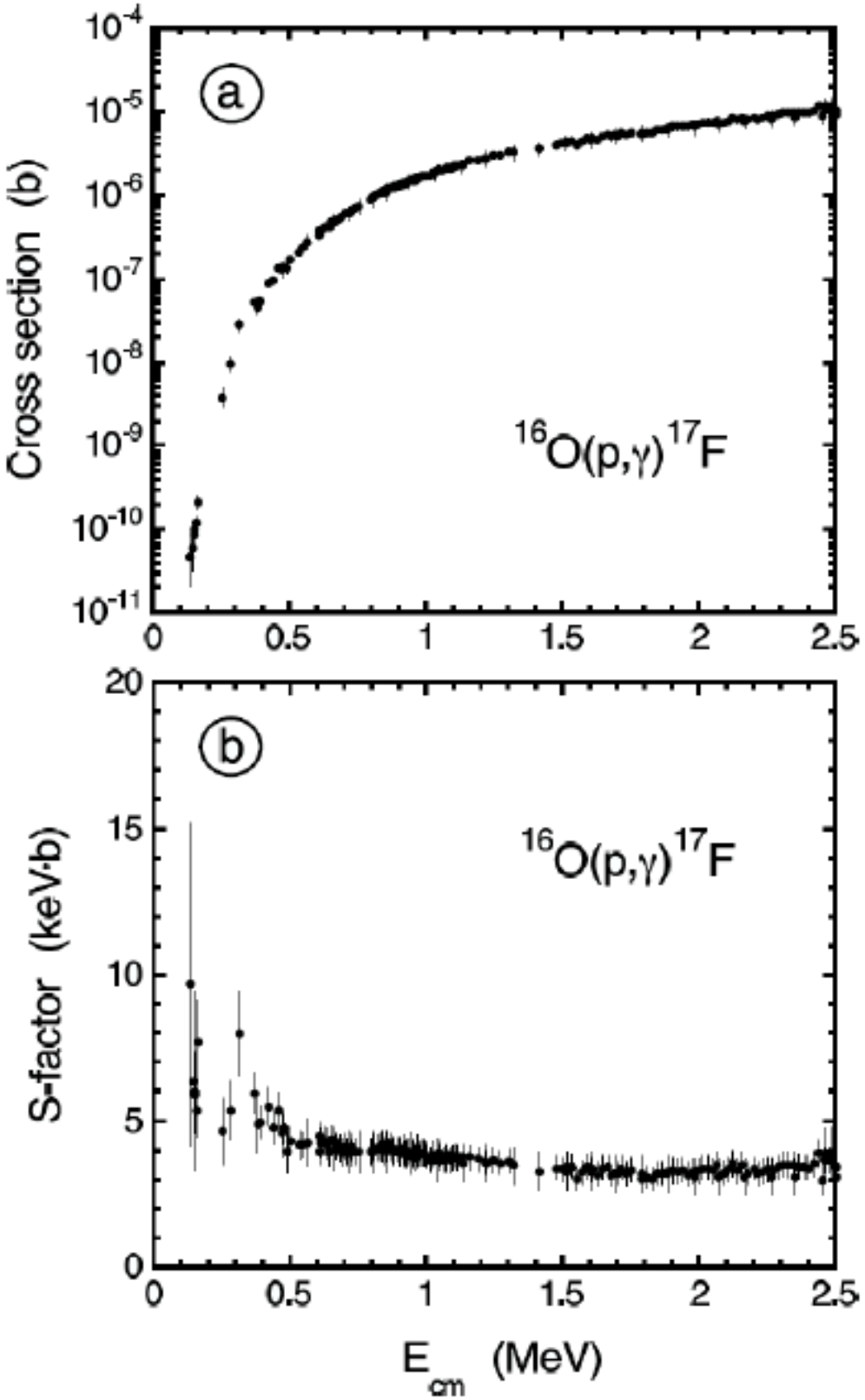

Figure 1.17 *A comparison of the cross section to the astrophysical s-factor for a study of the $^{16}O(p,\gamma)^{17}F$ as presented in [12].*

energetically favourable state exists in that nucleus. This process is shown in equation 1.12 using the notation from earlier.

$$a + X \rightarrow C^* \rightarrow b + Y. \tag{1.12}$$

Schematically this is shown in figure 1.18 where the beam energy in the centre of mass frame is denoted by E_a. All states between the threshold, S_a, and the top of the available energy can be populated.

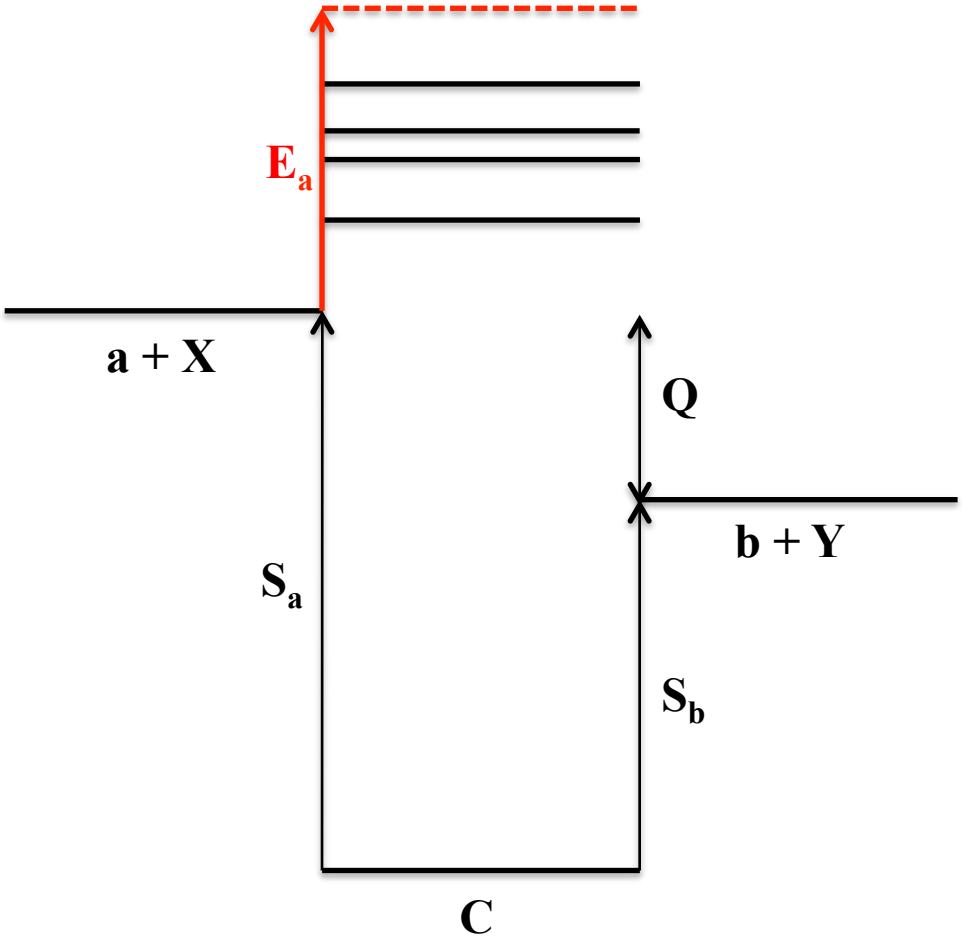

Figure 1.18 *A schematic representation of a compound nuclear reaction where the reaction between a and X populates an excited state in nucleus C which then decays by emitting b and Y. Any states above S_a and below the energy of the beam of a can be populated with probability depending on angular momentum transfer, width and energy above the threshold.*

Therefore, a direct measurement of a beam of particle "a" onto a target of nucleus "X" can give information on the nuclear structure of the nucleus "C" from the

cross section of a reaction of the form in equation 1.12.

Any resonance above the reaction threshold (S_a), given by equation 1.13, and below the beam energy in the compound nucleus, is accessible, with varying probability. This probability appeals to the same theory as tunnelling through the Coulomb barrier, where the process is now additionally hindered by the centrifugal barrier dependant upon the relative spins of the state and the reactants, shown in equation 1.14,

$$S_a = (M_a + M_X - M_C)c^2 \tag{1.13}$$

$$V_{cf} = \frac{l(l+1)\hbar^2}{2\mu r^2}. \tag{1.14}$$

Here, ℓ is the angular momentum transfer required to populate the state of spin $\mathbf{J}$ such that standard vector addition applies to the relationship $\mathbf{J} = \mathbf{J_a} + \mathbf{J_X} + \ell$. Evidently, lower ℓ states are more favourably accessible. Where a resonance is populated, there can be a significant enhancement of the reaction cross-section.

As discussed previously, the geometrical cross section is related to the de Broglie wavelength, however with the addition of a resonance a statistical factor must be added to this expression. As such the maximum cross section takes the form in equation 1.15,

$$\sigma_{max} = \pi \left(\frac{\lambda}{2\pi}\right)^2 \frac{2J+1}{(2J_a+1)(2J_X+1)}(1+\delta_{aX}). \tag{1.15}$$

The probability of a resonance being populated is then its branching ratio, the partial width to the entrance channel divided by the total width of the resonance. The probability of it decaying is similar, the partial width to the exit channel divided by the total width. Breit and Wigner then added this effect to the reaction cross section to give the Breit-Wigner cross section in equation 1.16 [41],

$$\sigma = \pi \left(\frac{\lambda}{2\pi}\right)^2 \frac{2J+1}{(2J_a+1)(2J_X+1)}(1+\delta_{aX})\frac{\Gamma_1\Gamma_2}{(E-E_R)^2+(\Gamma/2)^2}. \tag{1.16}$$

Γ_1 and Γ_2 denote the entrance channel and exit channel partial widths of the resonance respectively.

1.3.4 Reaction Rate

It has already been discussed that charged particle nuclear reactions are inhibited by the Coulomb barrier that exists between two nuclei. These nuclei must have enough energy between them to penetrate this barrier, with the probability of penetration increasing with energy to the point where the barrier is fully overcome.

The energy of particles in the stellar gas is governed by the Maxwell-Boltzmann distribution dependant upon the temperature of the gas, as shown in equation 1.17 [11],

$$\phi(E) \propto E\ exp\left(\frac{-E}{kT}\right). \tag{1.17}$$

Taking the piecewise product of the energy distribution and the penetrability leads to a maximum probability of the reaction occurring being found at energy E_0 as shown in figure 1.19.

The reaction rate is therefore found from a combination of the probability of a collision having an energy with the probability of the barrier being penetrated. If we now consider the Maxwell-Boltzmann distribution in terms of velocity, analogous to the energy as $E \propto v^2$, we can give the reaction rate per particle pair as:

$$< \sigma v >= \int_0^\infty \phi(v) v \sigma(v) dv. \tag{1.18}$$

Now, considering the available flux of reaction nuclei, the rate becomes:

$$r = N_a N_X < \sigma v > . \tag{1.19}$$

By combining the Maxwell Boltzmann distribution with the expression for the cross-section given in equation 1.11 the reaction rate becomes:

$$< \sigma v >= \left(\frac{8}{\pi\mu}\right)^{1/2} \frac{1}{(kT)^{3/2}} \int_0^\infty S(E) exp\left[-\frac{E}{kT} - \frac{b}{E^{1/2}}\right] dE. \tag{1.20}$$

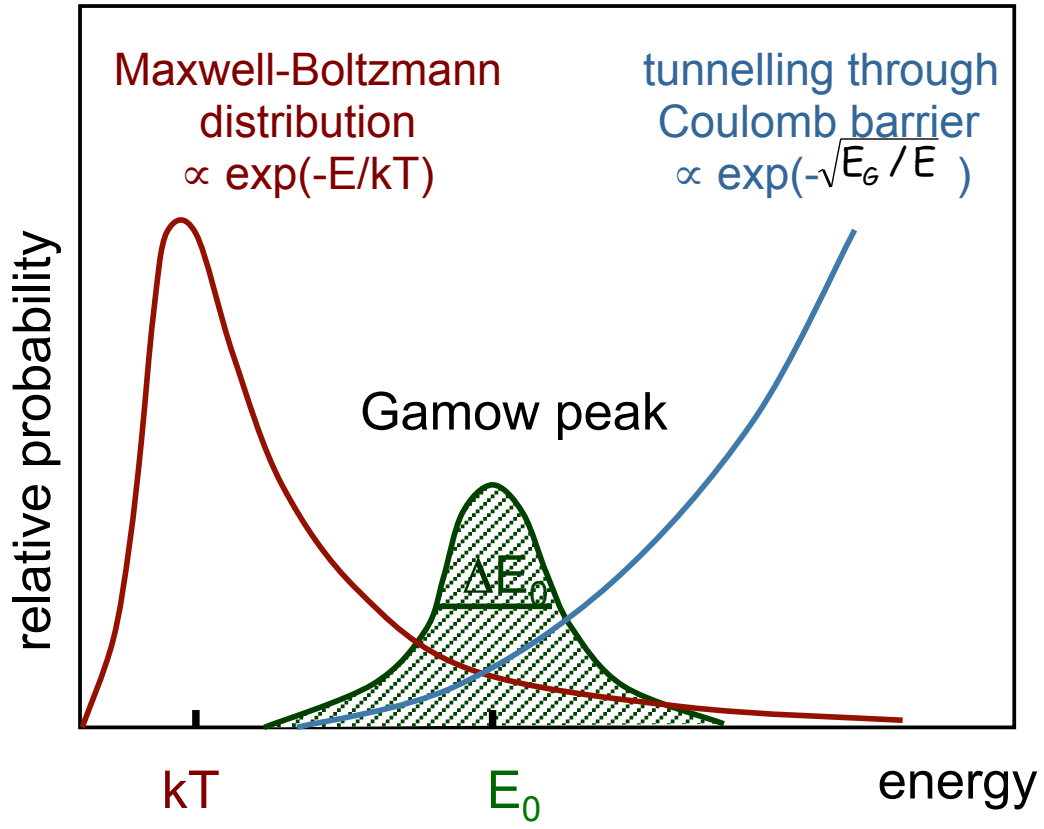

Figure 1.19 *The Gamow window is shown as a convolution of Maxwell-Boltzmann distribution of energies and the probability of tunnelling through the Coulomb barrier. [42].*

Gamow Window

From here, one can estimate the typical energies at which nuclear burning takes place in stars, known as the Gamow window, as shown in figure 1.19. Over a narrow burning window the s-factor can be assumed to be constant and therefore taken out of the integral. Hence, the energy at which the integral is at a maximum, the Gamow peak, can be found from the first derivative of the integrand to be:

$$E_0 = \left(\frac{bkT}{2}\right)^{2/3} = 1.22\left(Z_1^2 Z_2^2 \mu T_6^2\right)^{1/3} keV. \tag{1.21}$$

The effective width of the Gamow peak must now be estimated. To do this, it is approximated to be a Gaussian distribution of width $\Delta/2$ and maximum value of the integrand from equation 1.20 at E_0. By setting the second derivative of this integrand at E_0 equal to the second derivative of a Gaussian expression around

$E = E_0$ we find:

$$\Delta = \frac{4}{\sqrt{3}}\sqrt{E_0 kT} = 0.749\left(Z_1^2 Z_2^2 \mu T_6^5\right)^{1/6} keV. \tag{1.22}$$

This estimates the energy region where a nuclear reaction is likely to proceed dependant upon the temperature of the environment. This estimation relies upon the assumption that the s-factor, containing all resonant information in the cross section, is constant across the Gamow Window. This, of course, is rarely the case and Rauscher has estimated the effect on the Gamow Window for many reactions of interest. More accurate calculations of the relevant burning regions for those reactions affected most are given [43].

1.3.5 Indirect Measurements

Past studies of relevance to the work undertaken in this thesis have been carried out through a variety of indirect methods to try to extract nuclear physics information where direct measurements are challenging. This can be due to the Coulomb barrier and location of the Gamow window or the difficulty in producing intense radioactive beams. Presented here is a discussion of some of the techniques which have been applied in the past.

Inelastic Scattering

Inelastic scattering is defined by the non-conservation of kinetic energy, and can be used to describe various nuclear reactions. In the case discussed here, however, we refer to a reaction that would normally be elastic, such as (p,p) or (α,α), but leaves the product nucleus in an excited state. As a result, the emitted light ion has less energy, and the residual nucleus de-excites by the emission of further radiation. A basic inelastic scattering reaction is defined by:

$$a + X \rightarrow a' + X^* \tag{1.23a}$$

$$X(a, a')X^*. \tag{1.23b}$$

The resulting analysis can proceed through coincident detection of the scattered

components and any further radiation. Furthermore, the angular distribution of this radiation provides crucial information about the spin and parity of the populated states. Not all scattered particles and emitted radiation need be detected; if all but one are detected with energy and angle known, then the remaining particle can be reconstructed through kinematics to give its implied energy and scattering angle.

Charge Exchange

A charge exchange reaction replaces a neutron with a proton or vice versa, populating excited state in the product nucleus, for example a (^{3}He,t) reaction. A generic example is given in equation 1.24,

$$ {}^{q}_{p}a + {}^{m}_{n}X \rightarrow {}^{q}_{p-1}b + {}^{m}_{n+1}Y^* \tag{1.24a} $$

$$ X(a,b)Y^*. \tag{1.24b} $$

Transfer Reactions

Transfer reactions refer to the transfer of a nucleon from one nucleus to the other, often named stripping (removing a nucleon from the beam) or pickup (the beam gains a nucleon). As such, excited states in the product nucleus can be populated and information extracted much like discussed previously through coincidences and angular distributions. An example of a neutron pickup reaction in inverse kinematics is given in equation 1.25.

$$ {}^{q}_{p}a + {}^{m}_{n}X \rightarrow {}^{q-1}_{p}a + {}^{m+1}_{n}X^* \tag{1.25a} $$

$$ X(a,b)X^*. \tag{1.25b} $$

1.4 The R-Matrix Formalism

The R-Matrix formalism is a very useful tool for the analysis of nuclear excitation functions that has been implemented in most of the analyses presented in this

thesis as well as much of the relevant work in the literature discussed in the next chapter. It shall be briefly introduced here while a more in-depth discussion is presented in chapter 5.

The R-matrix formalism was generalised for nuclear reactions in the 1958 work of Lane and Thomas [44]. The premise of the formalism is to bypass consideration of the complex nuclear force in the calculation of reaction cross-sections. This is done by setting the wavefunction of the system, within the range of the nuclear force, to be equal to this wavefunction at distances where the interaction is purely Coulomb.

As shown in chapters 4 and 5, this allows a resonant cross section to be calculated over a range of energies as a function of resonant parameters and includes interference effects between resonances. This has proven useful for the extraction of resonant parameters and extrapolation of cross-sections to low-energy, experimentally challenging regions. This formalism is applied to the data extracted in this thesis in chapter 4.

Chapter 2

Relevant Previous Work

2.1 The $^{18}\mathbf{F}(\mathbf{p},\alpha)^{15}\mathbf{O}$ Reaction

In the energy region of interest, several states in ^{19}Ne may make resonant contributions to the ^{18}F(p,α)^{15}O reaction rate. Presented here is a discussion of the previous studies relevant to this reaction, with particular attention given to the observed resonances and their measured parameters. The low energy resonances close to the Gamow window are discussed alongside those in the energy region studied in this thesis.

2.1.1 The Situation Prior to 2007

The availability of suitable radioactive ^{18}F beams from the mid 1990s for use at Argonne [45] and Louvain-La-Neuve [46] led to a boom in experimental studies of the ^{18}F(p,α)^{15}O reaction, with direct measurements being possible for the first time. The first such studies were carried out independently in 1995 by Rehm *et al.* [47] and Coszach *et al.* [46]. Both of these measurements clearly observed the now well-known 665 keV resonance.

The work of Rehm *et al.* [47] was carried out at the Argonne National Laboratory with a ^{18}F beam from a stored source. The ^{18}F was synthesised by bombarding enriched water, $H_2{}^{18}O$, with protons and the resulting ^{18}F ions from the ^{18}O(p,n)^{18}F reaction stored in a copper cathode and transported to the laboratory for acceleration in the ATLAS facility tandem accelerator.

The work of Coszach *et al.* [46] was carried out at Louvain-La-Neuve with a radioactive ^{18}F beam produced again by bombarding enriched water with protons. In this case the resulting ^{18}F ions were extracted in situ, and accelerated to the experimental set up.

The 665 keV resonance

The most well-known, and readily observable state in ^{19}Ne, of interest to the ^{18}F(p,α)^{15}O reaction, is that at E_x=7076 keV. This resonance results in significant resonant structure in the reaction cross-section. It was identified in both of the early direct measurements discussed above [46, 47]. By studying similar energy ranges, both of these publications were able to show that a $J^\pi = {}^3/_2{}^+$ assignment best described the data in the region of this state. Coszach *et al.* [46] impinged their ^{18}F beam on a polyethylene target thick enough to cover the energy range 550-740 keV, observing an excess of counts in the α-channel and measuring the differential cross-section in the p-channel. Comparison to many possible cross-section fits concluded that this was most likely a ${}^3/_2{}^+$ resonance at 638 keV above threshold with a total width of 37$\pm$5 keV. The ℓ=0 transition was confirmed by the angular distribution of the observed α-particles being isotropic.

Rehm *et al.* [47] measured the ^{18}F(p,α)^{15}O reaction cross section at pre-requested beam energies. The ^{18}F beam was impinged onto a thin polypropylene target and detecting the resulting α particles to obtain the cross section. This resulted in three distinct data points which showed a cross-section consistent with that from a ${}^3/_2{}^+$ resonance of total width 40 keV.

Following these measurements, much of the work on this reaction focussed on extracting well constrained parameters for this resonance, including a repeat of the experiment by Rehm *et al.* to extract more data points and to further constrain the results [48]. The most accurate measurement of its properties to date was conducted by Bardayan *et al.* in 2001 [49] through a direct measurement experiment. Simultaneous analysis was carried out on the ^{18}F(p,α)^{15}O and ^{18}F(p,p)^{18}F reactions and using *R*-matrix and Breit-Wigner analysis extracted the now accepted experimental parameters of $E_{c.m.}$=664.7(16) keV, Γ=39.0(16) keV and Γ_p/Γ=0.39(2).

The renewed interest in this reaction also saw some older methods, see [50], revisited. In 1998, Utku *et al.* [51] performed the charge exchange reaction ^{19}F(^{3}He,t)^{19}Ne in forward kinematics and identified 19 resonances around the ^{18}F+p threshold, 14 of which were above threshold. At nova temperatures the Gamow window for the ^{18}F(p,α)^{15}O reaction is around 0.04 - 0.4 MeV and three of these states lie in this region, one of which was observed for the first time. Even resonances lying outside of the Gamow window, however, could contribute to the reaction cross section through interference effects. In total, three resonance were observed for the first time, at 8 , 38 and 287 keV above threshold with proposed $J^{\pi} = {}^{3}/_{2}^{+}$, ${}^{3}/_{2}^{+}$ and ${}^{5}/_{2}^{+}$ respectively. The latter of these lies within the Gamow window. The J^{π} assignments were based on possible mirror assignments and are considered tentative.

A previous thin target direct measurement at Louvain-La-Neuve by Graulich *et al.* [52], however, gave the first observation of the 330 keV resonance, and assigned a spin-parity of ${}^{3}/_{2}^{-}$. In this study, scattered tritons were detected in coincidence with the protons and α-particles emitted as the resonance decays. This allowed experimental partial widths to be measured and reported for the resonances. Reaction rate calculations then showed that the main contributing resonances to the ^{18}F(p,α)^{15}O reaction at nova temperatures are those at 330 keV and (now-known) 665 keV. Furthermore, in 2000, A. Coc *et al.* [3], reviewed the current status of ^{18}F production and destruction in novae and found that the 38 keV resonance, as observed by Utku *et al.*, could also have a significant contribution to the reaction rate, as shown in figure 2.1.

In the early 2000s, a group from Oak Ridge National Laboratory (ORNL) sought to extract accurate parameters for the 665 keV resonance [49] and the 330 keV resonance [53]. The parameters extracted for the 665 keV resonance are discussed above, while the currently accepted parameters for the 330 keV resonance are based on this work and reported in the review by Nesaraja *et al.* [54].

A further measurement by the ORNL group, of the ^{18}F(p,p)^{18}F reaction, observed an apparent new resonance of $J^{\pi}={}^{7}/_{2}^{+}$ at $E_{c.m.}$=1009 keV. A further analysis of the reported parameters by Fortune and Sherr [55] found this assignment highly unlikely, however, due to an unphysical spectroscopic factor and its existence was later ruled out by the work of Murphy *et al.* [56].

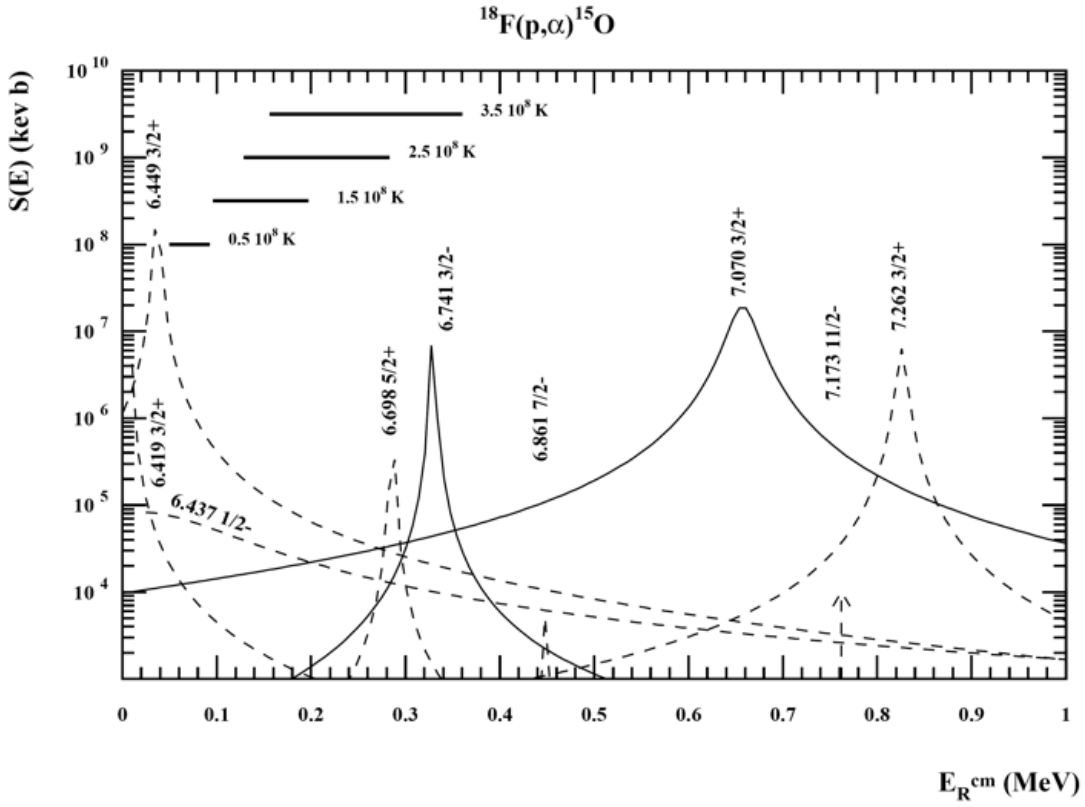

Figure 2.1 *Contributions to the astrophysical s-factor of the $^{18}F(p,\alpha)^{15}O$ reaction from predicted and observed resonances. The significant contribution from the 38 keV resonance is shown [3]*

2.1.2 Predictions of Dufour and Descouvemont

In 2007, Dufour and Descouvemont predicted the existence of a broad state in ^{19}Ne, lying just below the ^{18}F+p threshold at 6411 keV. This state could have a significant effect on the ^{18}F(p,α)^{15}O reaction rate by enhancing the reaction rate in the energy region of interest [57] thus reducing the uncertainties associated with interference between the low energy $^3/_2^+$ resonances discussed above [58].

In their calculation, the wavefunction of the ^{19}Ne nucleus is formed by a superposition of cluster wavefunctions for three incoming channels, ^{18}F+p, ^{15}O+α and ^{18}Ne+n. This wavefunction is then calibrated to be consistent with the ^{18}F+p threshold and the well-known 665 keV resonance at E$_x$=7.075 MeV [59].

Using this wavefunction as a basis, they then implemented the generator coordinate method and the calculable R-matrix, similar to a previous work by Dufour [60]. They found two $^1/_2^+$ states, in addition to the ground state, and three $^3/_2^+$ states in ^{19}Ne. One of the $^3/_2^+$ resonances produced parameters consistent

Table 2.1 *Calculated parameters of two new $^1/_2{}^+$ resonance in the $^{18}F(p,\alpha)^{15}O$ reaction [57].*

E_{cm} (MeV)	Γ_p (MeV)	Γ_α (MeV)
-0.41		0.231
1.49	0.157	0.139

with the well-known 665 keV resonance. These results were then compared to the mirror nucleus, ^{19}F. Candidate partner states have been observed experimentally in this nucleus at E_x=5.94 and 8.65 MeV. From here, the spectroscopic factors of the low energy resonance were calculated to be S_p=0.082 and S_α=0.768 while the higher energy resonance had S_p=0.707 and S_α=0.094.

Calculations show that the higher energy $^1/_2{}^+$ resonance in ^{19}Ne lies at around 1 MeV above the proton threshold. This is a significant energy shift from the energy of the implied mirror state, but not unlikely for a resonance with a large spectroscopic factor and low ℓ. As a result, it is expected to play a significant role in the ^{18}F(p,α)^{15}O cross section. The lower energy $^1/_2{}^+$ resonance is expected around 100 keV below the proton threshold, also with a large spectroscopic factor. This resonance is likely to significantly enhance the reaction cross section in the energy region of interest.

Assuming that the energy difference between a similar calculation for ^{19}F and the experimental resonance measurements is equal between mirror nuclei, the resonance energies are modified and the final results of [57] are given in table 2.1. The higher energy, broad, s-wave resonance should be readily observable in a direct measurement of the ^{18}F(p,α)^{15}O reaction, as exhibited by figure 2.2 from the reference [57]. If it is observed, the existence of the lower energy resonance may be inferred with a consequent significant impact on the overall ^{18}F(p,α)^{15}O reaction rate and the production of ^{18}F in novae.

2.1.3 Current Status

Predicted States

Following the predictions of Dufour and Descouvemont [57], two experiments, employing alternative methods, were designed with the observation of the broad high-energy resonance at the forefront of their aims.

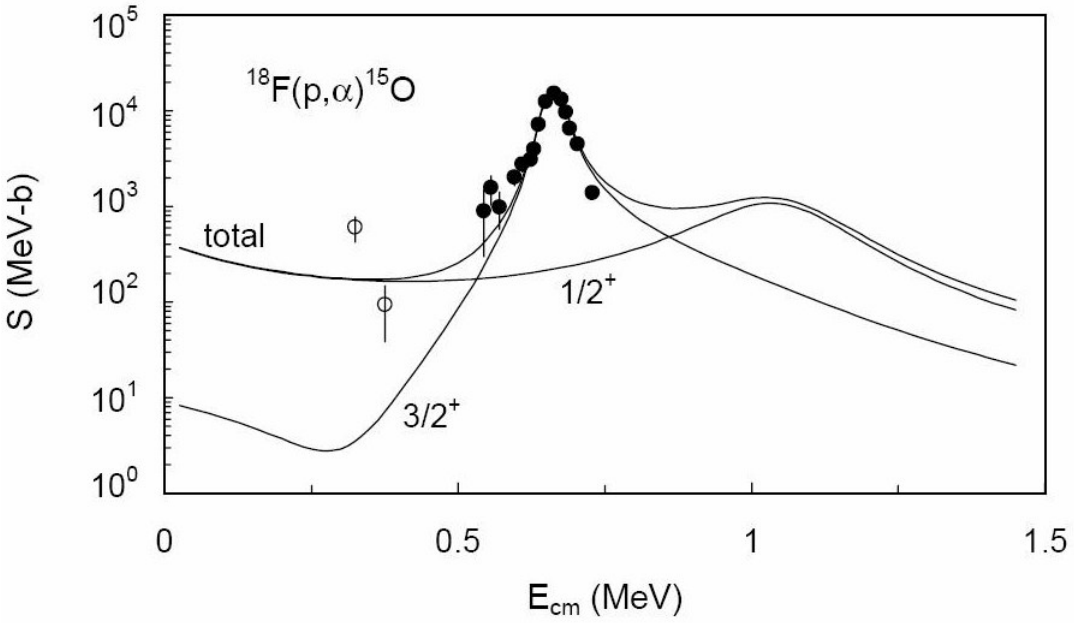

Figure 2.2 *Contributions to the astrophysical s-factor of the $^{18}F(p,\alpha)^{15}O$ reaction from $^3/_2^+$ and $^1/_2^+$ resonances. The predicted enhancement due to the inclusion of the resonances predicted by [57] is clear. Data are taken from [49] and [53]. Figure presented in reference [57]*

Murphy *et al.* carried out a direct measurement using the thick target method [56], employing a radioactive ^{18}F beam provided by the TRIUMF laboratory in Canada. This measurement took data up to around 1.6 MeV above the proton threshold for both a direct measurement of the ^{18}F(p,α)^{15}O and the ^{18}F(p,p)^{18}F elastic scattering, allowing simultaneous analysis to be carried out. Five resonances were observed, including a previously unobserved feature in the vicinity of the high energy cut off.

The proximity of this feature to the high energy cut-off hinders accurate extraction of the associated resonance parameters. Nonetheless, the authors sought to investigate the possibility that this resonance was consistent with the predictions of Dufour and Descouvemont [57]. With a tentative assignment of $J^\pi=^1/_2^+$, the partial widths extracted were significantly narrower than predicted by reference [57], hence, it was concluded that the predicted resonance had not been observed.

In the same period of time, Dalouzy *et al.* [61] carried out an experiment on the inelastic scattering of ^{19}Ne at Louvain-La-Neuve. A radioactive ^{19}Ne beam was produced and impinged upon a polypropylene target, thick enough to allow reactions to populate resonances in the excitation energy range of around 6.7 -

8.4 MeV in ^{19}Ne. This work observed five resonant structures with additional strength underlying those in the region of 7.5-8 MeV. Four of these structures were observed in the work of Murphy *et al.* including the high energy feature discussed above.

Angular distributions of the detected protons allowed the spin of all observed resonances to be assigned, while the parity was based upon the lowest value of ℓ required to populate the resonance from the entrance channel. Hence, the high energy resonance observed by Murphy *et al.* was unambiguously assigned J=$^5/_2$ with lowest angular momentum transfer of $\ell = 1$ implying a negative parity.

The additional strength underlying the resonant structures in the high energy region was found to be consistent with the existence of a J=$^1/_2$ state at E_x=7.863(39) MeV, in the vicinity of the prediction made by Dufour and Descouvemont. The total width was also calculated to be 292(107) keV, consistent with the prediction and contrary to what was found by Murphy *et al.* This discrepancy remained unresolved until the work presented in this thesis was undertaken.

Interference Between Resonances

Motivated by a discussion in a 2005 work by de Séréville *et al.* [62], another uncertainty that remains in the ^{18}F(p,α)^{15}O reaction is the nature of the relative interference effects between *s*-wave resonances at 8, 38 and 665 keV above the ^{18}F+p threshold. There have been many recent studies of the ^{18}F(p,α)^{15}O reaction that have attempted to resolve this issue, while also trying to constrain the contribution from the *p*-wave resonance at 330 keV. These are now discussed.

A cross-section measurement around the 665 keV resonance, by Chae *et al.* in 2006, included in its analysis a consideration of numerous possible interference terms [63]. During this discussion, and by including interference between the 1009 keV resonance observed by [59], they considered eight possible interference combinations between the 8, 38, 665 and 827 keV $^3/_2^+$ resonances and this higher energy $^7/_2^+$ resonance.

A further study by de Séréville *et al.* [64] was carried out at Louvain-La-Neuve. Despite making four direct measurements in the relevant energy range, and considering previous measurements, this work was also unable to bring firm conclusions on the nature of the relative interference between these resonances.

They considered only the relative interference of the three lowest energy $^3/_2^+$ resonances, having found a negligible contribution from the resonance at 827 keV. Their results do suggest a positive interference term for the 8 keV resonance, relative to the other $^3/_2^+$ resonances.

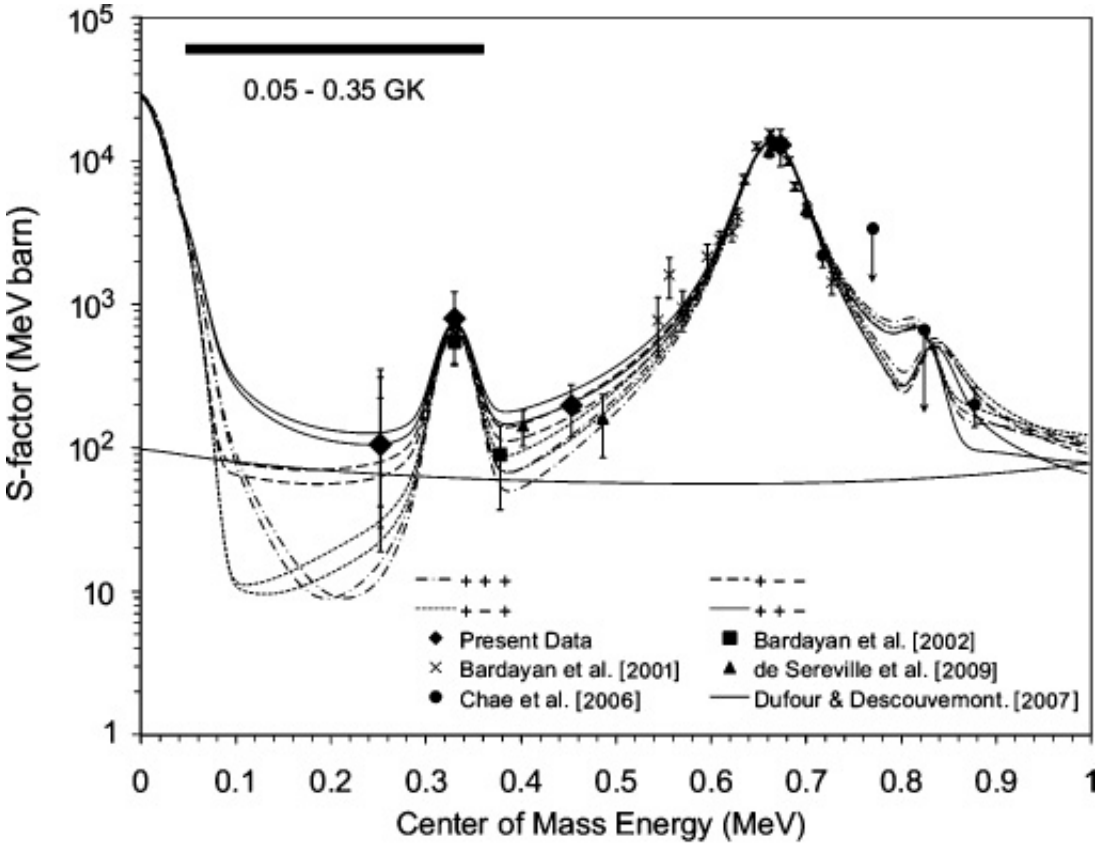

Figure 2.3 *Figure presented by Beer* et al. *[65] showing a range of possible interference terms between $^3/_2^+$ resonances at 8, 38 and 665 keV above the ^{18}F+p threshold. In addition, the proposed enhancement due to the predictions of Dufour and Descouvemont is shown along with s-factor measurements made by [49, 53, 63, 64]*

The recent work of Beer *et al.* [65] sought to address this through a further direct measurement of the astrophysical s-factor at four energies in or close to the Gamow Window for this reaction in novae. A radioactive ^{18}F beam, provided by the TRIUMF laboratory, was impinged upon a thin target to take measurements at 250, 330, 453 and 673 keV above the threshold, as shown in figure 2.3.

Direct measurements at low energies such as 250 keV are strongly inhibited by the Coulomb barrier and as such only two counts were observed at this energy despite a week of running with a relatively high intensity ^{18}F beam of 5×10^6 pps. The extracted s-factor, therefore, had very large error bars with 1, 2 and 3 σ levels shown in figure 2.3. While it is argued that the lowest *s*-factor curves are less

favourable, uncertainty over interference effects in this region remains unresolved.

Adekola et al.

Also in 2011, Adekola *et al.* [66] reported on the population of ^{19}Ne levels through the use, for the first time, of the ^{18}F(d,n)^{19}Ne* reaction. They measured the energies of emitted ^{15}O and α-particles from the decay of the excited ^{19}Ne levels and were able to extract angular distributions of the emitted neutrons through momentum conservation.

This information allowed spin-parity, excitation energy and spectroscopic factors to be extracted through a series of DWBA and R-matrix fits. This included the states that contribute to the interference uncertainty with consistent measurements made for those at $E_{c.m.}$=38 and 665 keV. The 8 keV resonance, however, is found to emit ions into the exit channel through an ℓ=1 transfer and so the corresponding state must have spin-parity of $^1/_2^-$ or $^3/_2^-$. This would remove the contribution of this state to the $^3/_2^+$ interference uncertainty but could add further uncertainty to the total ^{18}F(p,α)^{15}O reaction rate through interference with the observed $^3/_2^-$ resonance at 330 keV.

Further to the discussions of Dufour and Descouvemont [57], there also appears to be a state with ℓ=0 transfer lying just below the proton threshold in Adekola *et al.*. This would result in a resonance of $J^\pi = {}^1/_2^+$ or $^3/_2^+$, possibly being consistent with the predicted sub-threshold resonance postulated by Dufour and Descouvemont, however an inconsistent α partial width implies more work is required to confirm that this is the postulated state.

2.2 The ^{18}O(p, α)^{15}N Reaction

Often run alongside the direct ^{18}F(p,α)^{15}O reaction studies discussed above is the direct measurement of the ^{18}O(p,α)^{15}N reaction for normalisation purposes. As such, a further study in this thesis performed the analysis of an available data set from such an experiment. As discussed in chapter 1, the reaction itself has some astrophysical importance as well. Previous studies of this reaction are now discussed with specific focus on the three resonances which were the focus of this present work.

Throughout the 1970s and 1980s, many studies sought to observe and parameterise the states of interest in ^{19}F for the ^{18}O(p,α)^{15}N and ^{18}O(p,γ)^{19}F reactions. In 1999, Angulo *et al.* set out to review the status of the former reaction and found that resonances at $E_{c.m.}$=20, 143.5 and 656 keV are likely to dominate its rate [67], and the resulting ^{14}N/^{15}N ratio observed in pre solar grains.

Until recently, the lowest energy of these states, 20 keV above the proton threshold, was not well constrained due to the difficulty of direct measurements below the Coulomb barrier. This state, with $J^{\pi}=5/2^{+}$, has mainly been studied via indirect methods, although it has been observed in a direct capture experiment [68]. The resonance strength was determined from the proton transfer reaction ^{18}O(^{3}He,d)^{19}F with proton spectroscopic factors extracted through a DWBA analysis [69, 70].

The 143.5 keV resonance is relatively well-known [67]. The broadest of these states, however, at $E_{c.m.}$=656 keV, is poorly constrained. A compilation of accepted values by Tilley *et al.* [71] stated that the currently accepted total width is 340 keV, while the partial widths are estimated to be Γ_p=5 keV and Γ_α=95 keV, with no uncertainties reported. Evidently this leaves a significant discrepancy between the measured total and partial widths, since the only other open channel for this reaction to proceed is through γ-ray emission, with a width of the order of eV. This is a discrepancy which must be addressed.

In addition to this broad resonance, two other resonances are reported in the vicinity by Tilley *et al.*, a further $1/2^{+}$ resonance at around $E_{c.m.}$=800 keV and a $3/2^{-}$ resonance at around $E_{c.m.}$=600 keV. The resonance at $E_{c.m.}$= 800 keV was identified in many early studies of this reaction [72, 73], with Yagi *et al.* performing extensive work on the understanding of the two $1/2^{+}$ resonances. While unable to extract accurate parameters for the 656 keV resonance, they did conclude that it must have the opposite relative interference phase to the 800 keV resonance to produce a reasonable fit to their data.

Further works by Mak *et al.* [74] and Lorenz-Wirzba *et al.* [75] were still unable to extract accurate parameters for this 656 keV resonance, however the resonances at 800 keV and 600 keV were constrained. Little work on this reaction followed and best estimates to 1995 are given in table 2.2 as reported by Tilley *et al.* [71].

More recently, this reaction has been studied again by La Cognata *et al.*. These studies set out to address the discrepancy in previous measurements of the resonance at 656 keV by performing a Trojan Horse study. In this case the

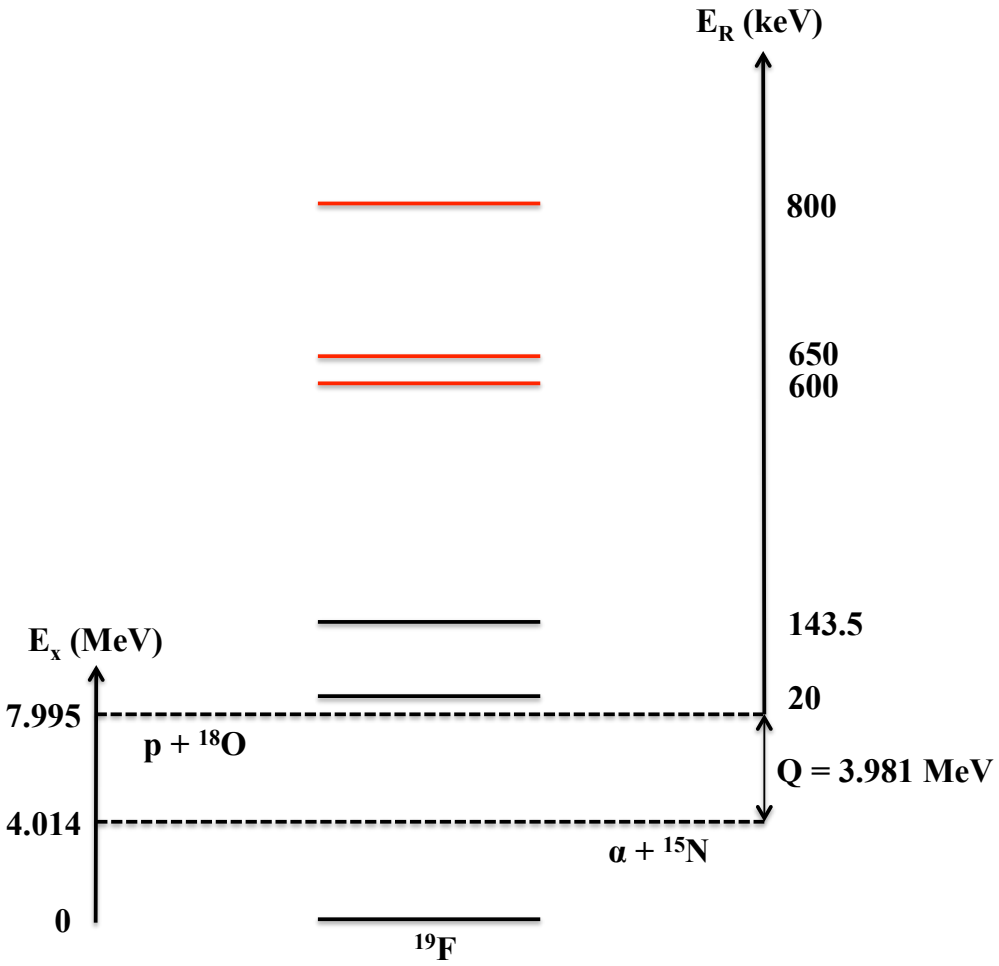

Figure 2.4 *Level diagram showing resonances of interest in the ^{18}O+p system. The three resonances with the most significant contribution are shown at 20, 143.5 and∼650 keV. The three resonances with greatest uncertainties are shown in red at ∼600, 650 and 800 keV. Excitation and resonance energy scales are not linked numerically.*

entrance channel is ^{18}O+d. Performing this reaction at much higher energies, the nuclear region is more accessible and the proton in the deuterium ion is brought within the nuclear field of the ^{18}O ion without a significant hinderance by the Coulomb barrier. Hence, the reaction can then proceed with the neutron acting as a spectator. The first result of this work was to improve the constraints of the reaction rate associated with the 20 keV resonance by a factor of 8.5 [76], due to a significant decrease in the uncertainty of the previously poorly constrained resonance energy.

The emitted α-particles were detected in coincidence with the recoiling ^{15}N nuclei in order to obtain an astrophysical s-factor spectrum in which there were obvious features around 660 and 800 keV. The preliminary analysis presented in 2008 [77]

Table 2.2 *Previous measurements around the uncertain 660 keV resonance [71]. There are no error estimates given for the 658 keV resonance.*

E_p (MeV)	E_{cm} (MeV)	J^π	Γ_p (keV)	Γ_α (keV)	Γ_{lab} (keV)
0.6326(4)	0.5991(4)	$\frac{3}{2}^-$	2.0(2)	0.065(6)	2.0(1)
0.695	0.658	$\frac{1}{2}^+$			340
0.8460(15)	0.8011(14)	$\frac{1}{2}^+$	26.0(15)	21(1)	47(1)

fitted the data in this region with two Breit-Wigner functions (to account for the two resonances) and an interference term between them. As a result it was found that the broad state may be lower in energy than previously thought. The results of this work gave: $E_{c.m.}$= 590±20 keV and total width of 208±26 keV.

A more in depth analysis was then carried out in a follow up to this work [78] using a *R*-matrix method modified for the Trojan Horse approach. The results are shown in figure 2.5. This work analysed the data in conjunction with the Lorenz-Wirzba data [75] to attempt to extract accurate parameters for the resonance at around 660 keV. The *R*-matrix fit was carried out with two $^1/_2^+$ levels, with opposite relative interference, being allowed to vary freely with the contribution from a fixed $^7/_2^+$ state at E_x= 8.629 MeV (E_r=634 keV) in ^{19}F added incoherently.

This $^7/_2^+$ resonance has not been previously observed. There is, however, a $^7/_2^-$ resonance reported at this energy on NNDC [17] having been observed in ^{15}N+α data [71]. This is reported, however, to be extremely narrow, at less than 1 keV, and so, when considered with the large angular momentum transfer required to populate this state, it is unlikely to make a significant contribution to the ^{18}O(p,α)^{15}N cross section. The narrow feature attributed to the $^3/_2^-$ resonance at around 600 keV is included, seemingly at the accepted values given in Tilley *et al.*, although no discussion of the parameters utilised has been offered.

With the parameters of the two $^3/_2^+$ resonances free to vary in the modified *R*-matrix formalism, new constraints were set. The 800 keV resonance was observed to be slightly higher energy at $E_{c.m.}$= 812.5±1.5 keV as well as being broader at Γ_p= 27±10 keV and Γ_α= 40^{+5}_{-13} keV. For the remaining resonance, the lower energy found in the preliminary study is revised up to $E_{c.m.}$= 609±2 keV, while the width is consistent with previous measurements at Γ= 199±3 keV, albeit at an ambitious precision.

Most recently, a review of the current status of this reaction was performed by Palmerini *et al.* [39]. This work, again, identifies the 656 keV resonance as

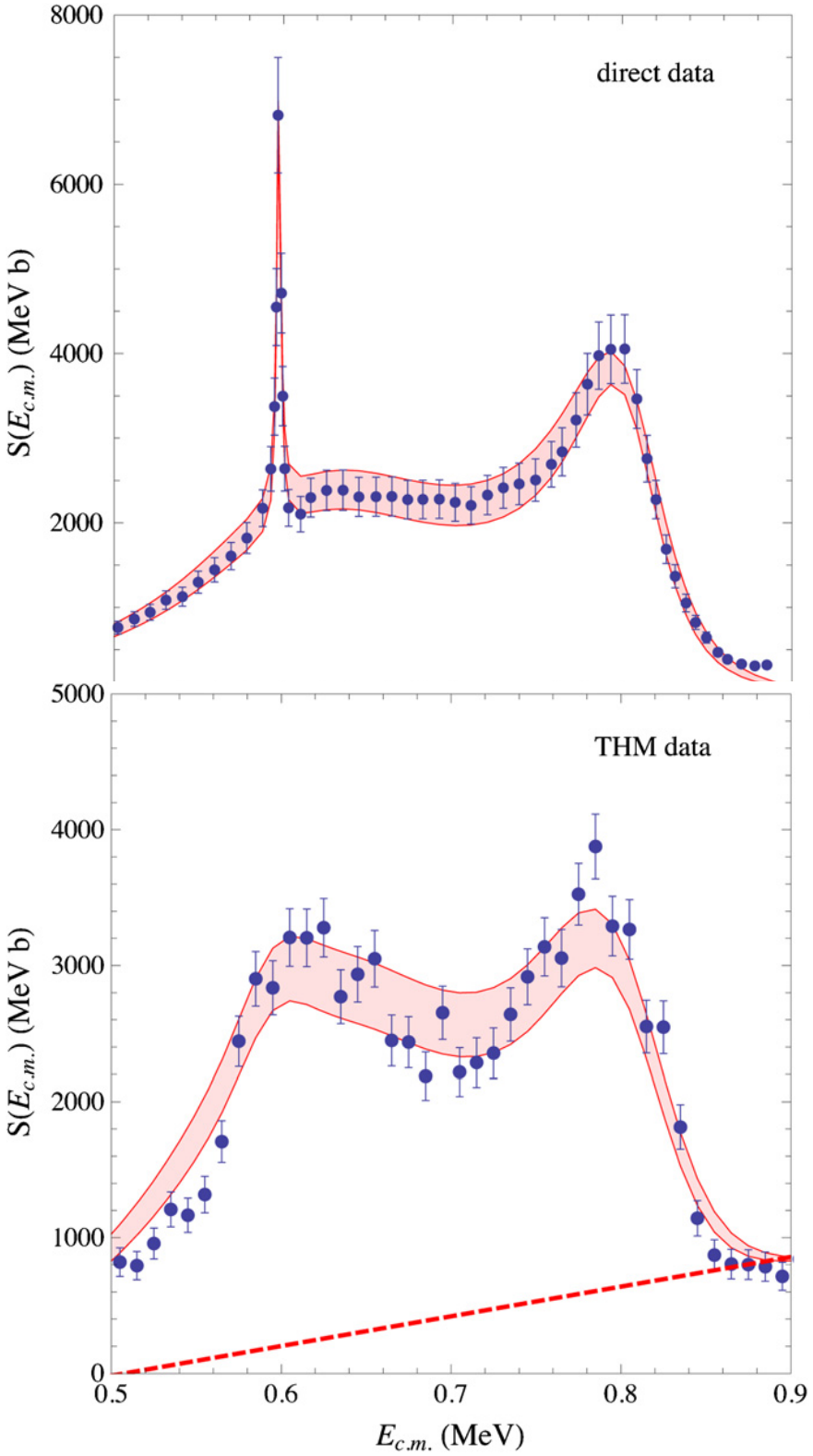

Figure 2.5 *Direct data from [75] (top panel) and Trojan Horse data from [78] (lower panel) simultaneously fitted through the R-matrix formalism by allowing all parameters associated with the 650 and 800 keV resonances to vary freely. The narrow resonance at ∼600 keV appears to have been included but is not discussed in the text. The dashed line denotes a background contribution.*

the greatest uncertainty in this reaction. However, this work also accepts the improvement in the parameter precision from the Trojan Horse Measurement by La Cognata *et al.* [78].

Chapter 3

Experimental Measurements of the $^{18}\mathrm{F}(\mathrm{p},\alpha)^{15}\mathrm{O}$ and $^{18}\mathrm{O}(\mathrm{p},\alpha)^{15}\mathrm{N}$ reactions

3.1 $^{18}\mathrm{F}(\mathrm{p},\alpha)^{15}\mathrm{O}$ Experiment

An experiment was carried out at the GANIL-SPIRAL facility [79], figure 3.1, Caen, in April 2010, with the primary aim of resolving the discrepancy surrounding the observation of a broad s-wave resonance consistent with that predicted by Dufour and Descouvemont [57]. While the 2009 study of Dalouzy *et al.* [61] made such a consistent observation, the work of Murphy *et al.* [56], in the same year, did not.

3.1.1 Target Selection and Measurement

The ^{18}F beam to be provided was specified to have E = 4.00 MeV/u = 72.0 MeV, the lowest energy available to the GANIL facility. Further degradation of the beam was required, however, to minimise fusion evaporation contamination from reactions on the carbon present in the target foil and to achieve a centre of mass energy matched to the scientific objectives. To optimise the possibility of observing the resonance as predicted by Dufour and Descouvemont [57], 1.49 MeV above the reaction threshold with Γ_p=157 keV and Γ_α=139 keV, a centre of

Figure 3.1 *Arial view of the GANIL facility in Caen, France [80].*

mass energy of around 1.6 MeV was required, corresponding to a beam energy of E = 1.68 MeV/u = 30.2 MeV. The reduced beam energy would eliminate as much fusion evaporation background as possible while also covering the full energy range of the resonance.

Degrader

To achieve the required reduction in beam energy, a gold foil would be placed immediately upstream of the target foil, thick enough to degrade the beam to the required energy. In addition, the use of gold foil was expected to allow beam normalisation through Rutherford Back Scattering (RBS).

`SRIM2008` [81] was used to produce energy-range tables for ^{18}F ions in natural gold (^{197}Au) over the full energy range of the beam. Interpolating between the points on this table in the region of this beam energy results in a maximum deviation of 0.025 %, hence the range of the initial ^{18}F beam was estimated to be 47.3 μm in gold. The degradation of a beam, however, is a stochastic process and the energy profile of the beam was therefore not unique upon exit of the gold foil (and entry to the target). The Bohr formula given in equation 3.1 gives

the standard deviation of the beam energy after degradation, depending on the charge number of the incoming beam and target (Z), the atomic density of the target (N) and the thickness of the target (d),

$$\sigma = \frac{Z_1 e^2}{2\epsilon_0}\sqrt{\frac{Z_2 N d}{\pi}}. \tag{3.1}$$

Hence, to ensure that most of the beam was above the required energy and to account for systematic uncertainties in the `SRIM2008` calculations [12], we required $E_{cm} \geq 1.6+3\sigma$ MeV upon entry to the experimental target.

The following process was employed to calculate the required thickness of gold. The remaining beam energy after five different foil thicknesses, from 6 to 10 μm, was calculated along with the respective standard deviations. The thickness as a function of remaining energy was then fitted with a straight line and the thickness which corresponds to $E_{lab} = 30.2$ MeV calculated from the fit. This was found to be 8.9 μm.

One might expect the degraded energy to have a more complex relationship to detector thickness than a linear fit. It was found, however, that over the region of interest a straight line fit was adequate. The $\bar{\chi}^2$ value was found to be 0.5 with error bars of 0.7 %, as suggested by [12].

Each energy then had 3 standard deviations added to it to create a set of "top energy" data points. These values were fitted with a second straight line. From here, the top energy remaining after a degrader of thickness 8.9 μm was found to be 31.1 MeV. Referring back to the initial energy-thickness relationship, the required thickness of gold was found to be 8.7 μm. This process is shown graphically in figure 3.2.

Gold foils were commercially available with nominal thicknesses of 8 or 9 μm, therefore, a thickness of 8 μm was chosen for the gold degrader. This results in a mean energy of 33.4 MeV, 1.72 MeV in the centre of mass, well above the required energy.

To estimate the thickness of the gold, a precision measurement of its mass was made. This was required as there were difficulties with making a measurement from triple alpha degradation. The surface area of the foil was then used with

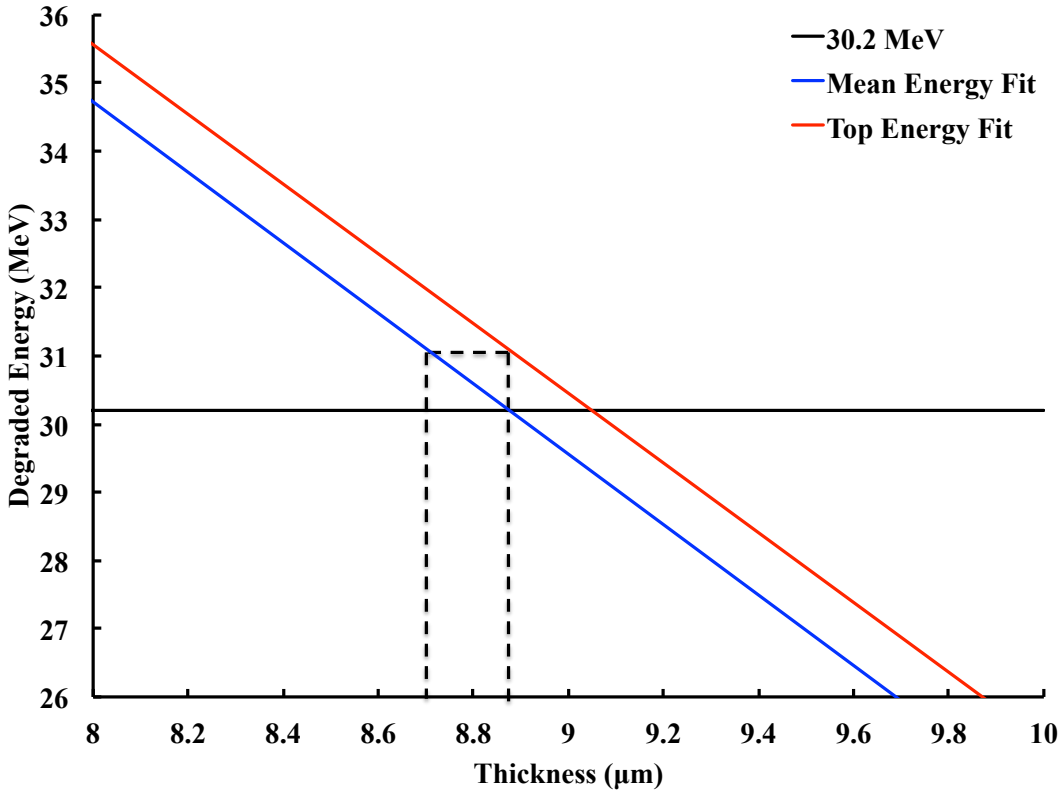

Figure 3.2 *Relationships between mean degraded energy and thickness (blue) and between the top degraded energy and thickness (red). The solid black line shows the target energy of 30.2 MeV and the black dashed lines outline the process of choosing a suitable gold thickness.*

the density (19.3 g/cm^3) to calculate the thickness (T) through equation 3.2,

$$T = \frac{m}{\rho A}. \tag{3.2}$$

Table 3.1 shows the results of the calculations. Foils 2 and 4 were selected for use in the experiment.

Upon arrival at GANIL, it was found that the beam was in fact lower in energy than expected. As such, a thinner gold foil was employed with nominal thickness of 6 μm. Upon repeating the above measurement with this new foil, it was found to have a thickness of 5.5$\pm$0.3 μm.

Table 3.1 *Measured area, mass and thickness of available gold foils for use as degrader.*

Foil Number	Area (cm^2)	Mass (mg)	Thickness (μm)
1	6.7(4)	98.80(5)	7.7(4)
2	6.4(4)	92.10(5)	7.4(4)
3	6.4(4)	96.90(5)	7.8(4)
4	6.4(4)	91.90(5)	7.4(4)
5	6.3(4)	94.70(5)	7.8(4)

Table 3.2 *Energies of dominant α-particle emission from triple-α source used for target measurements. [17]*

Nucleus	α-energy (keV)	Intensity	Range in CH_2 (μm)
^{239}Pu	5156.59(14)	70.77(14)%	36.2
^{241}Am	5485.56(12)	84.8(5)%	39.8
^{244}Cm	5804.77(5)	76.90(10)%	43.5

Target

Immediately downstream of the degrader was the CH_2 target. Since protons and alpha particles were to be detected in a detector centred around 0°, it was important that the beam stopped in the target and would not impact the detector, increasing dead time and possibly damaging the apparatus. Assuming a gold foil of 8 μm, the mean energy of the ^{18}F beam would be 33.485 MeV with $\sigma = 0.281$ MeV. Therefore, the 3σ energy would be 34.328 MeV which, from `SRIM2008` [81], has a range of 29.43 μm in CH_2. To fully cover the possible range of ^{18}F at this energy, the required thickness was assumed to be 29.5 μm.

During the run at GANIL, it was hoped to also study the ^{18}O(p,α)^{15}N reaction for normalisation purposes. As such, the target had to be thick enough to stop an ^{18}O beam of similar energy. A 72 MeV beam of ^{18}O would have slowed to 41.93 MeV after an 8 μm gold foil, with $\sigma = 0.249$ MeV. The high energy is, therefore, 42.68 MeV which has a range in CH_2 of 41.88 μm. Therefore, the required range of CH_2 was 41.95 μm.

As such, and to allow for variation in the degrader thickness and energy straggling, a target was to be built with two CH_2 foils, of nominal thickness 25 μm each. The thickness of the foils was measured using a triple-α source containing ^{239}Pu, ^{241}Am and ^{244}Cm. The energy of the most intense α-particle emitted from each nucleus is given in table 3.2.

Using a silicon surface barrier detector, the emitted α-particles were detected at

a distance of 6 cm in the setup shown in figure 3.3.

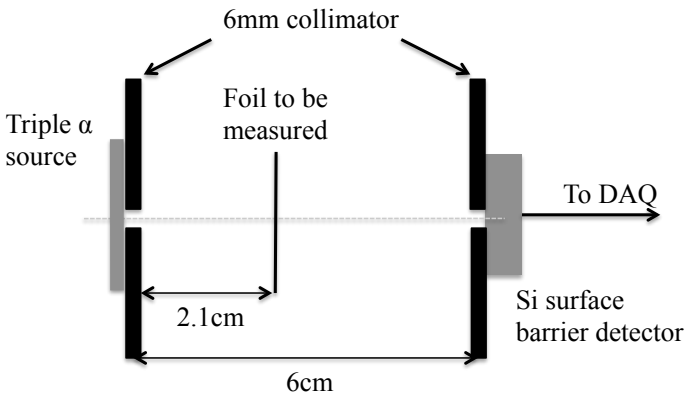

Figure 3.3 *Setup used to measure thickness of foils used in experimental work.*

The surface barrier detector was calibrated firstly using a pulser walkthrough and then known α-particle energies reported in table 3.2. The nine pulser points were fitted with a straight line to find the electronic offset which was then subtracted from the peak position for each of the measured α-particle peaks. The resolution was good enough to observe the primary and secondary α-particle peaks, the primary peaks used for the calibration. The gain was then found by dividing the known energy by the corrected peak location.

The foil to be measured was then placed 2.1 cm from the α-particle source. Using the calculated gain and offset, the energy of the detected α-particles after traversing the foil to be measured could be calculated by equation 3.3,

$$E = Gain \times (Peak - Offset) \tag{3.3}$$

and the resulting range in CH_2 calculated from `SRIM2008` [81]. The difference in range relative to the known energy gives the measured thickness of the target.

The resulting thicknesses of the targets used in the experiment were 27.1(1) μm and 27.6(1) μm giving a compound target of thickness 54.7(1) μm. There is an additional systematic error associated with the `SRIM2008` calculations, estimated to be around 10 % [12].

3.1.2 Detector preparation

The experiment was designed to detect the particles of interest at the most forward angles possible in order to improve resolution. A 50×50 mm square DSSSD (MSL type-W [82]) was placed at 0° in the forward laboratory frame.

Thickness

This detector had to be thick enough to stop all particles of interest so that all of their energy would be deposited in the silicon and an accurate measurement made. From kinematic calculations contained in [83], the maximum energy of a proton emitted from the ^{18}O(p,p)^{18}O reaction with a beam energy of 42.68 MeV, and lab angle of 0°, is 8.581 MeV. After travelling through 54.7 μm of CH_2, the average energy of the proton will be 8.292 MeV. The resulting range in silicon of this proton would be about 514 μm. With commonly available thicknesses being 300 μm, 500 μm or 1000 μm, it was decided to run with a silicon detector of thickness 1000 μm. This would ensure that all the emitted protons would be stopped.

Similarly, an α-particle from the ^{18}O(p,α)^{15}N reaction at this beam energy has energy 26.412 MeV with a range of about 348 μm in silicon, suitably depositing all energy in the detector.

Location

The optimum location for the detector then had to be considered, looking for the optimal trade off between energy resolution and the expected yield. To estimate the yield, consider the cross section of the ^{18}F(p,α)^{15}O reaction between 1 and 1.02 MeV as calculated by Murphy *et al.* [56]. This energy window corresponds to a thin slither of the target in use here, with around 2.3×10^{18} particles/cm^2. Therefore, assuming a beam intensity of 10^5 pps, the expected yield over 1 day is 2970 events/sr. The expected yield in a detector of size 50×50 mm square can then be plotted against distance from the target as shown in figure 3.4, scaled as a fraction of the yield at 125 mm.

For a proton emitted at 0° with 8.929 MeV, the time taken to reach the detector at 125 mm is around 3 ns. Similarly, an α-particle emitted with this energy would

take 6 ns to reach the detector at 125 mm. Therefore, to ensure a reasonable separation in the arrival time for particle identification for a system of this type, where the timing resolution is expected to be a few nanoseconds, 125 mm was the minimum target-detector distance chosen.

The expected energy resolution of the detector pixels could then be calculated for a pixel near the centre of the detector and one at the corner. This was done by calculating the energy of the outgoing α-particle [83] and considering energy loss through the remaining target for a collision at 1 MeV in the centre of mass. The calculation was made at each extreme of the pixel and the difference in energy of the detected particle was calculated. The fractional improvement with distance from a maximum at 125 mm was then plotted on figure 3.4.

The resulting optimum position was then taken as 250 mm from the target location, where the resolution is close to optimal without an overly significant loss of yield. At this point, the time separation between protons and alpha particles at 8.292 MeV is approximately 6.5 ns.

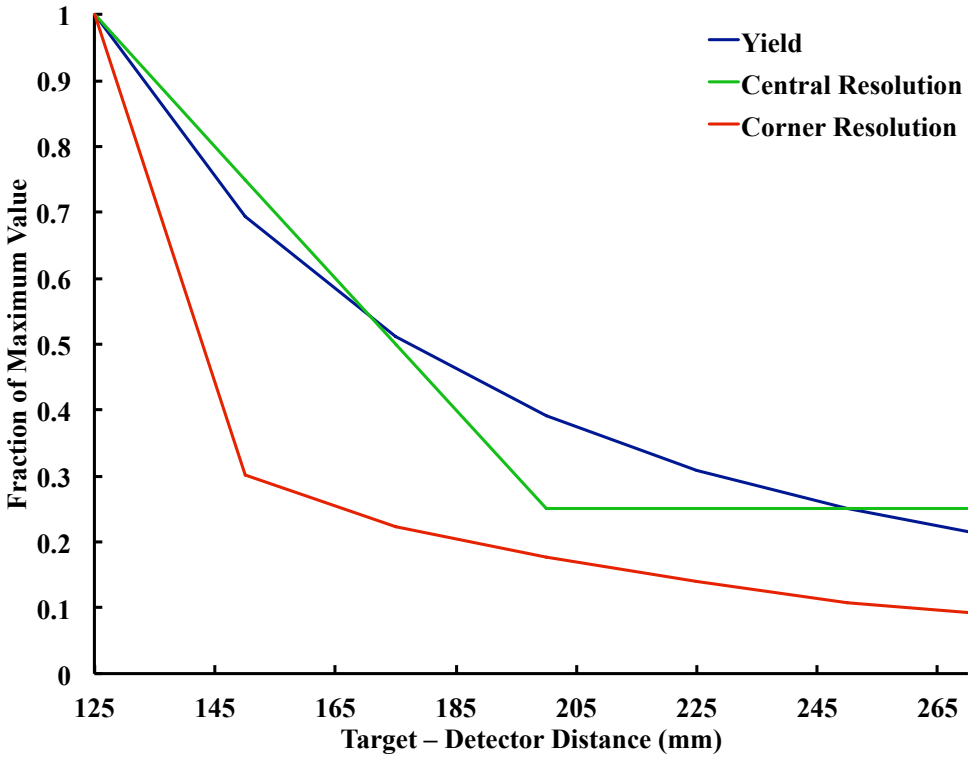

Figure 3.4 *Fractional decrease in expected yield (blue line), central resolution (green line) and corner resolution (red line) of α-particles from the $^{18}F(p,\alpha)^{15}O$ reaction*

Operating Voltage and Leakage Current

As discussed in appendix B, a DSSSD has an optimum operating voltage where the energy gap is wide enough to stop thermally excited electron-hole pairs from forming but the leakage current is at a plateau. The detector must also be tested to ensure that it reaches such a plateau without reaching a critically high leakage current.

The increase of leakage current with bias across the detector used can be seen in figure 3.5. It was decided to run at a detector bias of 275 V, which had a leakage current of 0.4 μA.

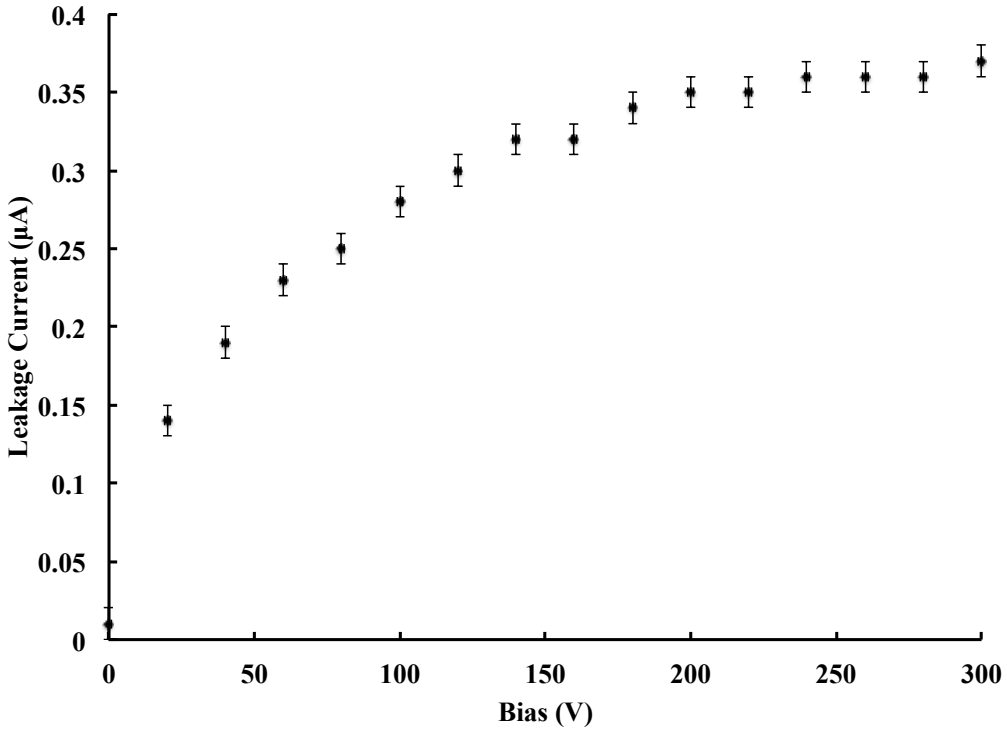

Figure 3.5 *Leakage current curve for the detector used in the experiment*

Angle

The distribution of events across the detector did not show any significant angular distribution effects and so events were summed over all angles, with the average angle considered the detection angle. The type-W detector has 32 unique angles ranging from $\sim 0.5^\circ - 7.6^\circ$ in the lab frame, with some angles occurring more than others. Taking a weighted average gives an average detection angle of 4.4° in the laboratory frame.

Calibration

The detectors and associated electronics were calibrated through a combination of a pulser walkthrough, see figure 3.6, and gain matching to a triple-α source with energies specified in table 3.2, see figure 3.7, including detector dead layer effects. The data in the experimental detectors was adequate to perform a multi-peak fit to the three α-particle groups. Thus the primary peak could be used for calibration.

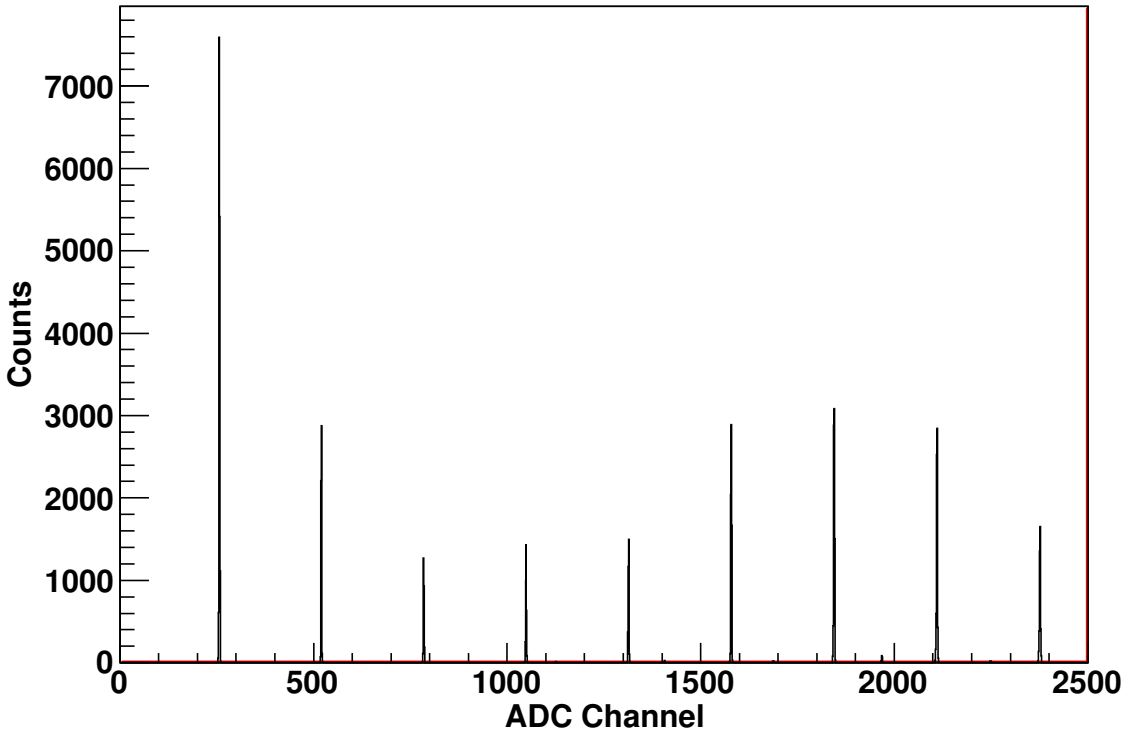

Figure 3.6 *Pulser walkthrough on a central strip on the front of type-W DSSSD used in the experiment.*

3.1.3 Hardware Setup

The 5.5±0.3 μm Au foil was mounted on the upstream face of the target ladder, degrading the ^{18}F beam to an energy of 1.9 MeV/A. The target then consisted of 55±4 μm of low density PTFE (CH_2 polymer), thick enough to stop the beam, but thin enough to allow light ions to escape. Protons and alpha particles, emitted from ^{18}F(p,p)^{18}F and ^{18}F(p,α)^{15}O reactions in the target, were detected in a 50 mm × 50 mm double sided silicon strip detector (Micron Semiconductors Ltd.

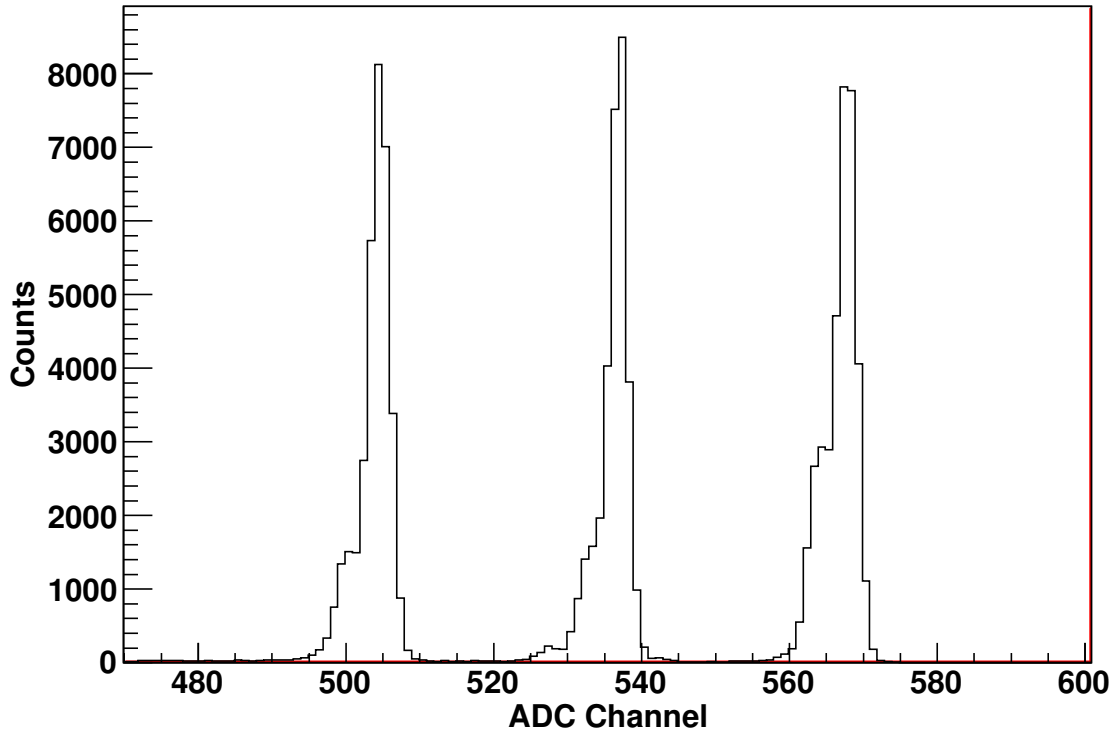

Figure 3.7 *Example triple alpha spectrum from a central strip on the front of type-W DSSSD used in the experiment.*

type-W [82]) located 248 ± 1 mm downstream of the target. Carbon ions were also observed from ^{18}F(^{12}C,^{12}C)^{18}F scattering.

To provide a local reference time for each ion delivered, a 3 μm aluminised Mylar foil at 45° to the beam axis and a microchannel plate (MCP) were positioned upstream.

Finally, a high purity germanium detector was placed external to the chamber to search for 1042 keV γ-rays consistent with the potential contamination of ^{18}Ne in the beam. Any contaminants of this type would also stop in the target and β^+ decay to an excited state of ^{18}F with a half-life of 1.7 s.

3.1.4 Electronics and Data Acquisition

The circuit diagram of the timing circuitry used in the experiment can be seen in figure 3.9.

The signals obtained from the 32 strips of the type-W detector were immediately

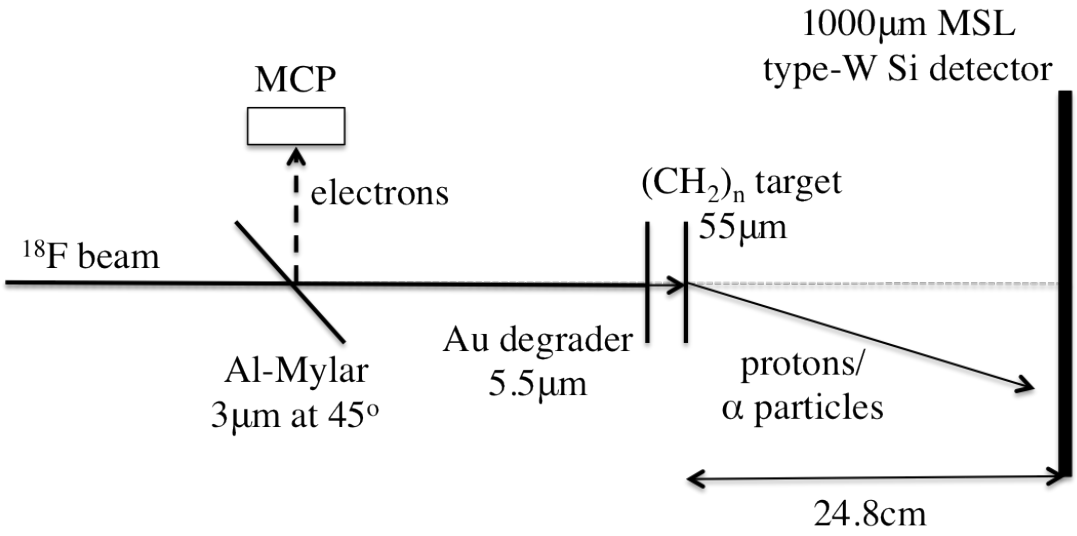

Figure 3.8 *Schematic layout of the experimental set up (not to scale). The ^{18}F was stopped in a thick CH_2 target. Recoiling proton and alpha particles were detected in a double sided silicon strip detector.*

passed to 32 RAL108 preamplifier units, inside the scattering chamber. Since air cooling was not possible, the preamplifiers were thermally mounted to copper heat sinks connected by 1/4 inch nylon tubing. A mixture of water and ethanol was then circulated around the cooling system at approximately -4°C by an external FTS RS44CL2 recirculating cooler [84], maintaining a safe operating temperature of around 15 °C

The output from these pre-amplifiers was then transmitted through 2×16 ribbon cables to the RAL109 shaping amplifier that both amplified the analogue signal and provided a leading edge logic signal. The gain of the shaping amplifiers were set using interchangeable resistors and a 100 Ω terminator. For the four required for the type-W detector, measuring α-particles of up to 26.4 MeV, a 1 kΩ resistor was used, corresponding to a full scale range of 33.3 MeV. For the remaining shaping amplifier, associated with the PIPS and photodiode detectors, detecting ^{18}F and ^{18}O ions at up to 72 MeV, a 10 kΩ resistor was used resulting in a full scale range of 183 MeV.

As discussed further in section 3.1.5, photodiode detectors placed in the target position were used to search for beam contaminants. For these detectors, Cocknell EC575 pre-amplifiers were used and mounted outside the chamber. The connection to the detectors inside the chamber were made through a vacuum feedthrough. The signal from these pre-amplifiers was then also connected to the RAL109 shaping amplifier.

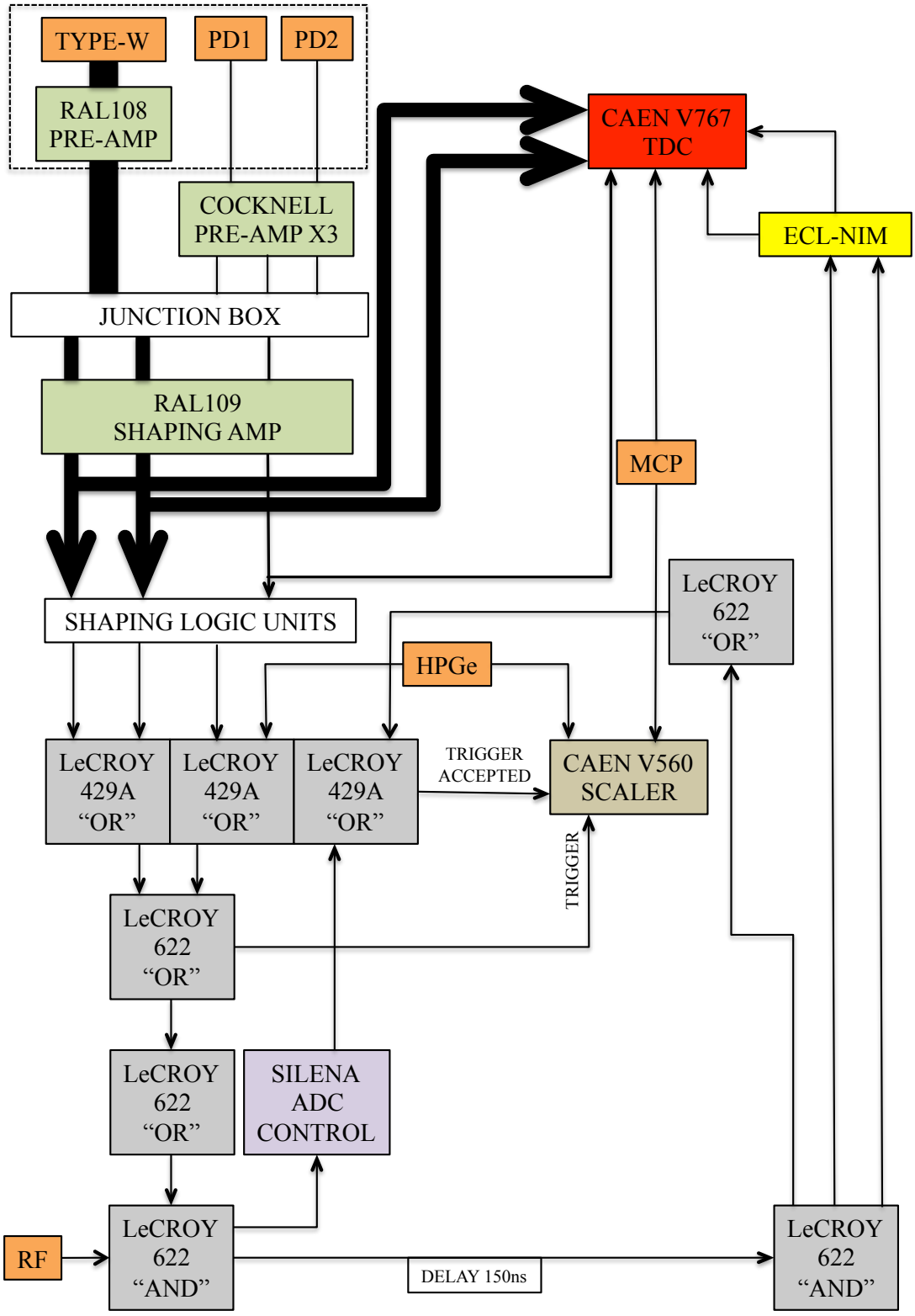

Figure 3.9 *Schematic layout of the timing circuit used in the experimental set up. Timing was operated in common stop mode.*

The amplified analogue signals were passed to two 32-channel Silena 9418/6V analogue-to-digital converters (ADCs) with a rise time of 2 μs for the type-W signals and 8 μs for the signals from the other detectors, to allow for the anticipated slower time-to-peak of the germanium detector amplifier output.

Trigger

The trigger for the system consisted of a total OR of all detectors, in coincidence with the RF of the accelerator. The analogue signals from the RAL109 amplifier were assigned to one of two logic Fan In/Fan Out modules and then passed to a second one creating a total OR for all detectors in the experimental setup. This was then shaped to form an approximately 100 ns pulse and placed in coincidence with the RF of the accelerator to form the experimental trigger.

This trigger was then split, with one signal delayed by 150 ns and the other passed to the Silena ADC Control (SAC). If the ADC was not busy, the trigger was added to "triggers accepted" and shaped to coincide with the delayed trigger and passed to the ADC to start the conversion to a digital signal that was passed to the data acquisition system.

Each "trigger" and "trigger accepted" was counted by the logic scalers in the experiment for dead time calculations.

Timing

The logic signal from the RAL109 amplifier was also fed to CAEN V767 time-to-digital converters (TDCs) in common stop mode. That is that a signal from the detectors started the timer and a signal from the RF stopped it. This minimised the dead time of the data acquisition. If the initial signal had come from the beam RF, then the TDC would have been active regardless of any events occurring.

3.1.5 Beam Production and diagnostics

Upon completion of the experimental setup, the beam was delivered to the SPIRAL facility at GANIL. A 95 MeV/A primary beam of ^{20}Ne bombarded a thick carbon target. Secondary ^{18}F ions were extracted in the molecular form HF, ionised in an ECR ion source, and post-accelerated with the CIME cyclotron [85]

to form a secondary radioactive ion beam of energy 3.924 MeV/A. The typical ^{18}F intensity was $\sim 2\times10^4$ pps. The beam optics were tuned to deliver ions of mass-to-charge ratio equal to 2, *i.e.* a 9^+ charge state for ^{18}F ions. The 9^+ charge state was achieved through use of a thin carbon stripper-foil placed in the beam line after the CIME cyclotron and before a charge separating magnet, and was motivated by the desire to eliminate expected contamination with ^{18}O ions.

Possible contamination of the beam by ^{18}Ne ions was searched for by inserting a Hamamatsu photodiode detector [86] with a thin aluminium degrader entrance foil into the target position and reducing the beam intensity to protect the detector. Heavier ions have greater stopping power and so beam contaminants can be identified by how much energy has been lost in the degrader. The beam was found to be split into two components, as shown in figure 3.10, with the lower energy component consistent with ^{18}Ne at an intensity $\sim 3\%$ of that of ^{18}F, thus contributing negligibly to the observed proton yield [87]. In addition, no evidence of ^{18}Ne contamination was observed in the high purity germanium spectrum.

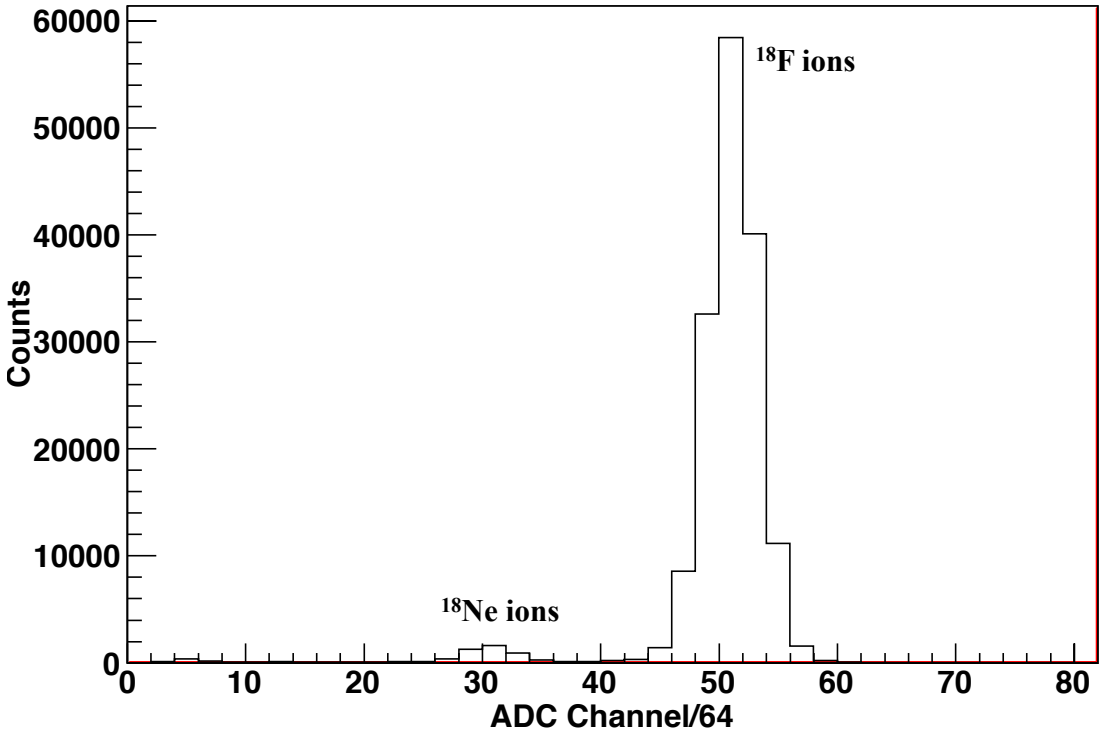

Figure 3.10 *Events recorded in the photodiode placed on the target ladder with a thin aluminium degrader entrance foil. ^{18}F and ^{18}Ne ions are well separated in energy.*

Table 3.3 *Key properties of a sector of the LEDA detector used in the $^{18}O(p,\alpha)^{15}N$ experiment.*

Strip	Mean Lab Angle (°)	Active Area (cm^2)	Solid Angle (sr)
0	5.389	1.786	0.000570
1	5.899	1.966	0.000626
2	6.409	2.145	0.000681
3	6.917	2.325	0.000736
4	7.424	2.504	0.000790
5	7.930	2.684	0.000844
6	8.435	2.864	0.000897
7	8.938	3.043	0.000949
8	9.441	3.223	0.001001
9	9.941	3.402	0.001052
10	10.440	3.582	0.001102

3.2 $^{18}\mathbf{O}(\mathbf{p},\alpha)^{15}\mathbf{N}$ Experiment

An experiment was carried out at the ISAC-I facility at TRIUMF, Vancouver, Canada in May 2009, prior to the beginning of my PhD. studies. A stable ^{18}O beam was provided from the OLIS stable ion beam source, stripped to charge state 8^+ and delivered to the TUDA scattering chamber [88].

The delivered beam was reported to have an energy of 2.400 MeV/u, equal to 43.2 MeV in the lab frame or 2.28 MeV in the centre of mass. This beam was then impinged upon a polyethylene target of nominal thickness 50 μm where ^{18}O+p reactions would take place emitting protons and alpha-particles. These were then detected in a full array of LEDA detectors [89] positioned 55.6 cm downstream of the target. Table 3.3 gives the specifications for a LEDA sector at this distance.

During the 3 experimental runs, covering around 4 hours, the beam intensity was recorded in the TRIUMF Faraday cup and reported to be 20, 20 and 21 epA. This corresponds to a total of around 2×10^{11} ^{18}O nuclei impacting the target over the total run time.

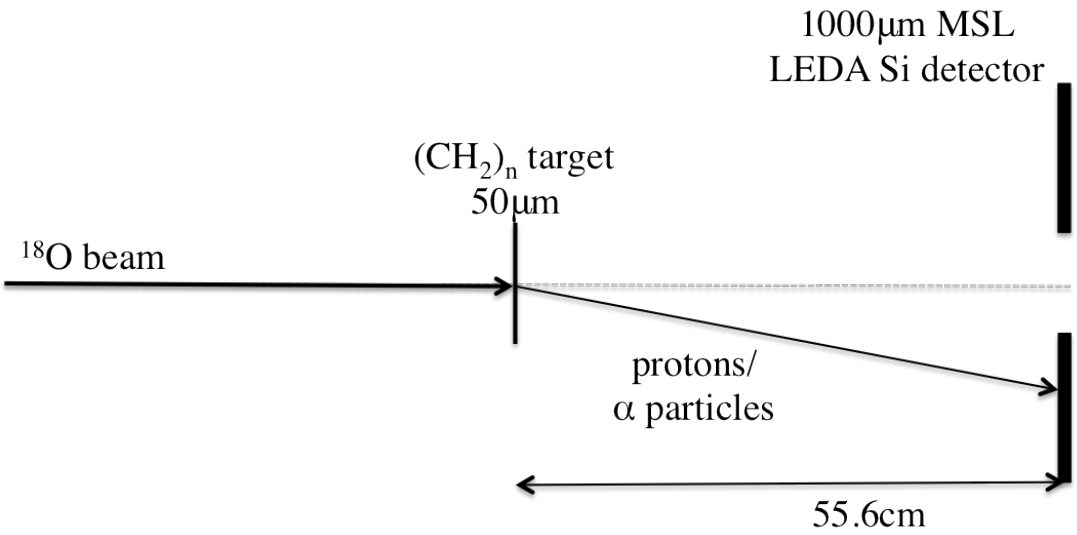

Figure 3.11 *Schematic layout of the experimental set up for the study of* $^{18}O(p,\alpha)^{15}N$. *The* ^{18}O *was stopped in a thick* CH_2 *target. Recoiling proton and alpha particles were detected in a LEDA type [89] double sided silicon strip detector.*

Chapter 4

Data Analysis and interpretation of experiments on the $^{18}\mathrm{F}(\mathrm{p},\alpha)^{15}\mathrm{O}$ and $^{18}\mathrm{O}(\mathrm{p},\alpha)^{15}\mathrm{N}$ reactions

4.1 $^{18}\mathrm{F}(\mathrm{p},\alpha)^{15}\mathrm{O}$ Analysis and Results

This chapter describes the extraction of excitation spectra from the data collected in the study of the ^{18}F(p,α)^{15}O reaction, and the ensuing data analysis. Events are selected on the basis of having equal energy recorded from the front and back of the detector and then by their energy and time of flight to select particle type. The R-Matrix formalism has then been employed to extract resonance parameters from the excitation spectra.

4.1.1 Event Selection

"Good" events were selected based on the energy difference of an event between front and back strips on the detector, revealing an intense peak at 0 MeV difference. There was, however, a long tail at lower energy differences implying that a channel had not been well calibrated. Plotting the front energy against the back energy on a 2D plot, as shown in figure 4.1, showed the discrepancy clearly.

To correct for this, six points were selected along the errant line of front versus back energy and fitted with a straight line. By reversing the fitted equation, the

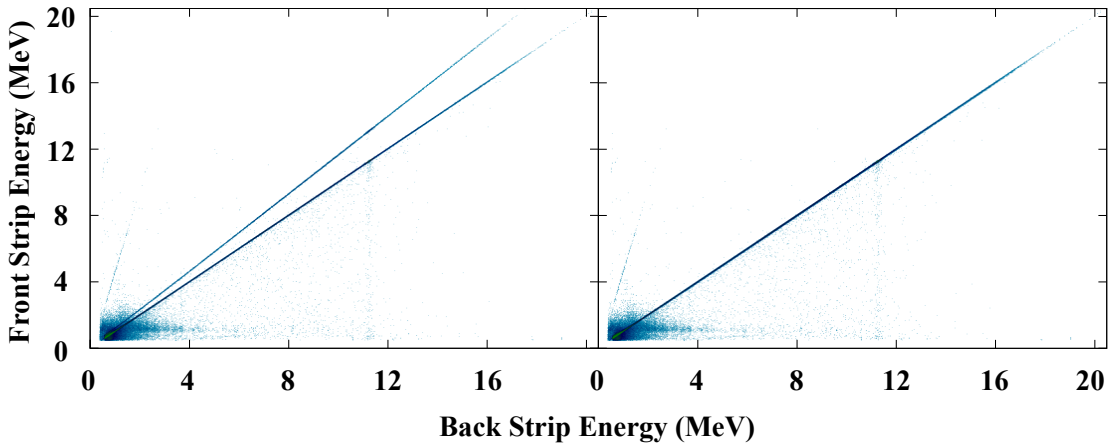

Figure 4.1 *Energy of events recorded in front strips of the detector against energy of event recorded in back strips before and after correction for moving channel.*

stray points from the errant channel were corrected to lie along the equal energy line again. This process increased the number of counts in the equal energy peak from 100799 to 116195, broadly consistent with a central strip being incorrectly calibrated.

A "region of interest" was then defined, as shown in figure 4.2, on the energy difference plot to include all "good" events within the equal energy peak. An additional locus of stray events appeared on the low energy side of the equal energy plot, around 5 % of the peak. The events did not show an intense enough contribution in the front versus back energy plot to allow a correction and so these events were discounted.

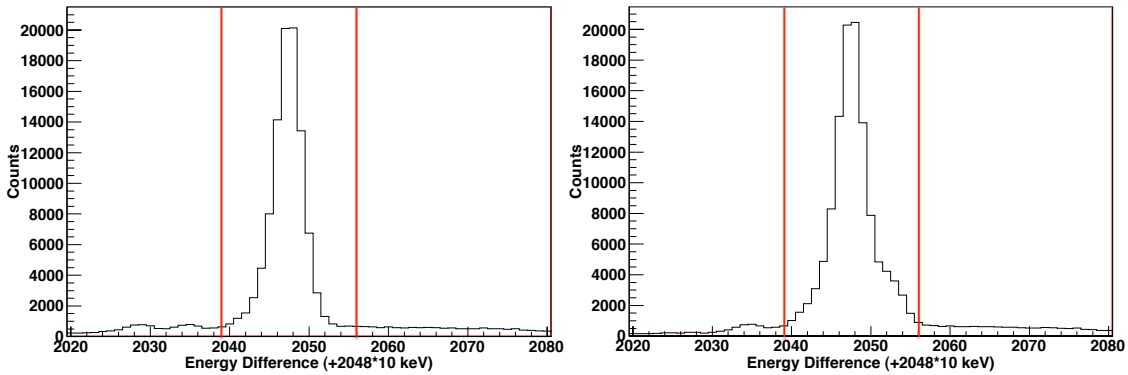

Figure 4.2 *Energy difference histogram for all events, the region of interest which includes all "good" events is shown. The left panel shows the distribution before the correction, the right panel shows after the correction.*

Good events selected above were included in an energy versus time of flight plot,

with three particle species well separated and identified, as shown in Figure 4.3. The most intense locus in Figure 4.3 corresponds to carbon ions, the next most intense to protons, and the low intensity band between the two corresponds to alpha-particles.

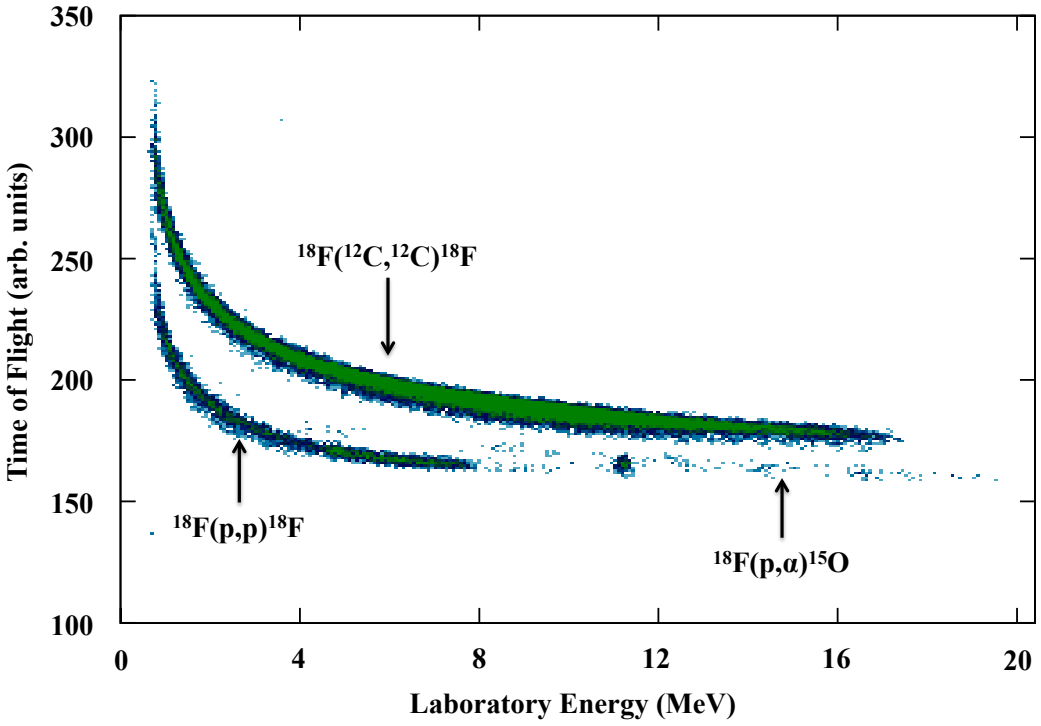

Figure 4.3 *The time difference between beam ions traversing the MCP foil and particles being detected in the DSSD, as a function of the detected particle energy. Three loci are observed: a proton locus (lower left), an alpha particle locus (middle), and a carbon ion locus from $^{18}F(^{12}C,^{12}C)^{18}F$ events. At ∼11 MeV, a ^{4}He ion beam contaminant is observed.*

As can be seen in Figure 4.3, there appears to be an additional contribution to the alpha-particle locus ($E_{lab} \sim 11$ MeV). Gating on these events revealed that they were impacting the centre of the detector, *i.e.* these events were aligned with the beam axis, as shown in figure 4.4. Given the A/q selection employed to accelerate ^{18}F ions, these events were most likely due to a ^{4}He beam contaminant which have a lower stopping power and therefore do not stop in the target. As a result, these events were discounted from further analysis.

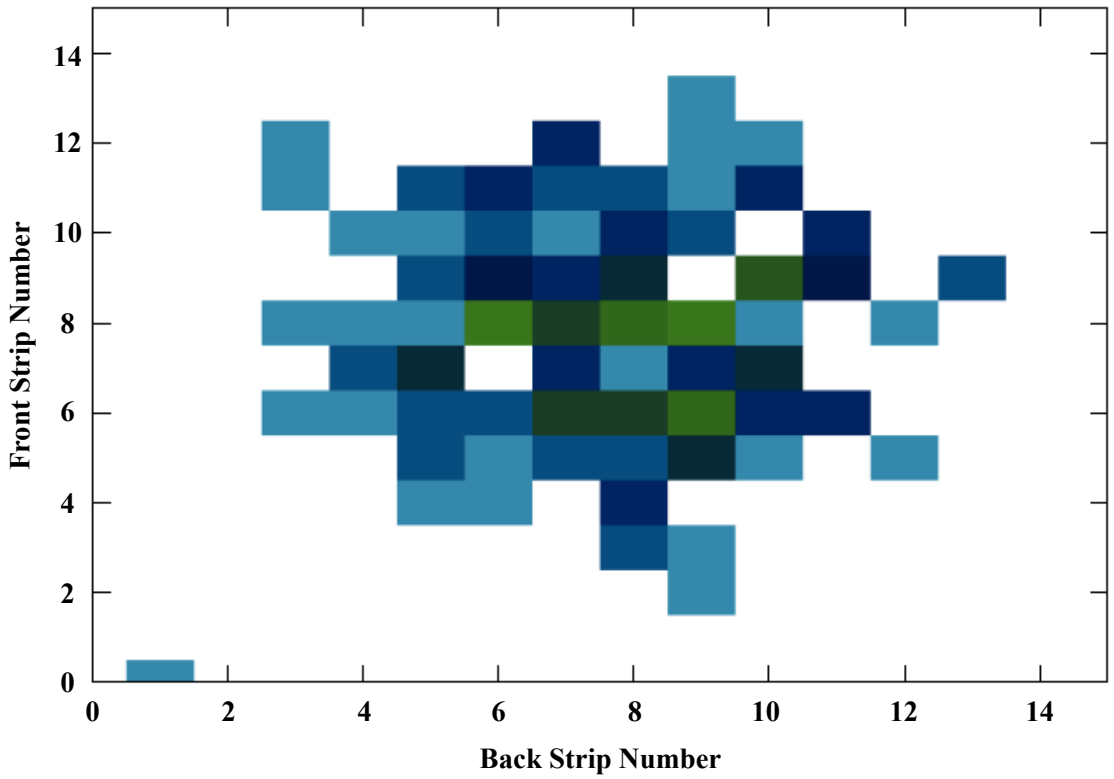

Figure 4.4 *Location of impact on the detector of all events within a "rogue" locus in the energy-time of flight plot.*

4.1.2 Energy Loss Calculations

For a thick-target measurement, with protons undergoing elastic scattering, and for alpha-particles originating from (p,α) reactions, the detected energy and angle of a particle is uniquely related to the centre of mass energy of the scattering/reaction. By consideration of all possible target depths at which reactions might occur and angles to which particles might be detected, an angle-dependent algorithm was generated mapping laboratory energy to centre of mass energy. This is a single-valued function, as shown in appendix A. Energy losses in the degrader, the target and in detector dead layers were based on `SRIM2008` [81]. For each unique pixel angle on the type-W detector, reaction kinematics and energy loss calculations were used to calculate the resultant laboratory energy of a particle from collisions at various depths in the target. A detected particle energy at a particular angle could then be mapped by linear interpolation between points to a centre of mass energy. Relative quenching effects between α-particles and protons have been accounted for here prior to the transformation to centre of mass energy, see appendix B.

4.1.3 Cross Section Calculations and Excitation Functions

The centre of mass excitation functions for the ^{18}F(p,p)^{18}F and ^{18}F(p,α)^{15}O reactions are shown in Figure 4.7. Data from all detector pixels (all scattering angles) are included as the limited number of events precluded projection of angular distributions. Furthermore, the limited statistics have required that the spectra are binned at 25 keV (CM).

The centre of mass energy reconstruction algorithm was first applied to each event to generate centre-of-mass energy spectra for the ^{18}F(p,p)^{18}F and ^{18}F(p,α)^{15}O reactions. The cross section was then calculated from equation 4.1. Here, Δx is the range of the beam in each energy bin, found from the stopping power as given by `SRIM2008` [81]. Combined with the known target density, ρ, this gave the number of target particles per bin. The beam intensity was assumed to be 2×10^4 pps as reported by the GANIL technical staff from Faraday Cup measurements.

The correction factor required to account for the dead time of the data acquisition system is denoted by η. This value was found from the total scaler values of triggers and triggers accepted throughout the experimental run: 579296:738188, giving η=0.785.

$$\frac{d\sigma}{d\Omega} = \frac{Y}{N_p \rho \Delta x \Delta\Omega \eta}. \tag{4.1}$$

Data have been removed near $E_{c.m.}$=0.92 MeV in the ^{18}F(p,α)^{15}O channel because of the contamination due to ^{4}He ions present in the beam. Several resonant structures are observed of which the most prominent is that at 665 keV, due to the well known 7076 keV $J^\pi = 3/2^+$ state in ^{19}Ne [49]. While the relative normalisation between the two data sets was maintained, to account for dead time, variation in the beam intensity, etc. the absolute normalisation and energy offset were adjusted to provide consistency with the known differential cross section in the vicinity of this peak. The final scale factors were 1.75 for the (p,α) channel and 2.27 for the elastic channel, with offsets of 0.038 MeV and 0.010 MeV respectively. The fractional variation in the scale factors, $\sim$13% from the mean, is consistent with the fractional uncertainty in the data. From figure 4.7, the fractional error is $\sim$7% in the ^{18}F(p,p)^{18}F data and $\sim$20% in the ^{18}F(p,α)^{15}O data.

As a result of the 665 keV resonance being used for absolute normalisation, no

parameters were extracted from this data set for this resonance. This resulted in an iterative process of fitting to the data which will be discussed further in the R-Matrix analysis.

It should be noted that the observed width of this peak matches well the rather precise widths found in previous studies, providing some validation of the Monte Carlo used to estimate the energy resolution, see section 4.1.4.

Fusion Evaporation

The presence of carbon in the target allows a possible contribution from fusion-evaporation reactions. To investigate this, data were taken with the CH_2 target replaced with a thick natural carbon target. The resulting yield of both protons and alpha particles was found to be small and insufficient to make a significant contribution to any of the proposed resonant structures. This conclusion was supported by the results of fusion-evaporation event rate estimates made using the LISE computer code [90]. The simulated fusion evaporation excitation function presented in the top panel figure 4.5 bore little resemblance to the observed events from the carbon target, shown in the lower panel of figure 4.5. The ^{4}He contaminant is also present in this data at around 10 MeV, slightly lower in energy than for the CH_2 target due to the thickness of the pure carbon target, nominally 75 μm.

4.1.4 Energy Resolution

Contributions to the energy resolution of these spectra arise from several factors, including: the geometric angular resolution of the detector; the intrinsic energy resolution of the detector and associated electronics; the energy and angular straggling of the beam and ions in passing through degraders, target and detector dead layers; uncertainty in the detector alignment with respect to the beam; beam divergence and beam spot size at the target. A significant additional uncertainty may arise if the absolute energy loss corrections are inaccurate, either because of insufficient knowledge of stopping powers, or due to incorrect target thickness measurements. The complexity of estimating the overall effect of these factors, especially given the use of a thick degrader, together with the potential sensitivity of the subsequent analysis on correct determination of the energies and energy resolutions, warranted the development of a dedicated Monte Carlo simulation of

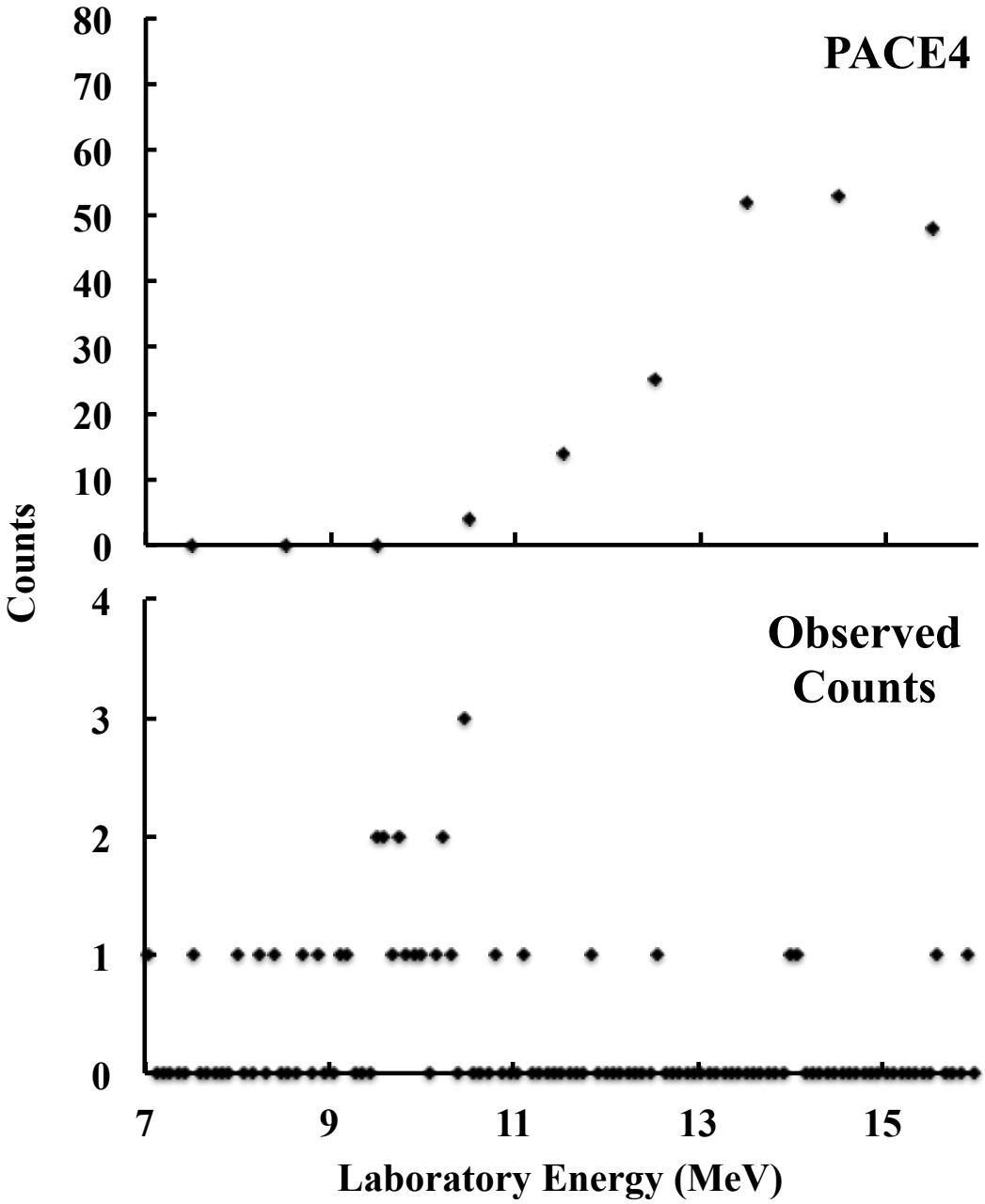

Figure 4.5 *α particle events observed from ^{18}F on the pure carbon target compared to the output of the PACE4 fusion evaporation code for 100000 events [90]*

the above effects. This was provided by Dr. Alexander Murphy. The provided code included energy losses, energy straggling and angular straggling based on `SRIM2008` [81], the intrinsic energy resolution of the detectors was 15 keV for protons and 25 keV for alpha particles [91], and the beam divergence (0.5 degrees) and beam spot size (10 mm) were determined during the experiment by the GANIL technical staff.

Taking into account the target and degrader thickness measurements made previously, the code simulated both reactions of interest, with the angular distribution of reactions assumed to be isotropic in the centre of mass.

The simulation returned a range of energy resolutions (rms, in the lab frame) at each simulated energy corresponding to various depths in the target, as shown in figure 4.6. For the detected alpha particles, this range was found to be between 40 and 70 keV for scatters occurring at centre of mass energies of 0.6 MeV, increasing to between 60 and 160 keV for centre of mass energy of 1.9 MeV while for the protons, this was between 30 and 40 keV at 0.6 MeV, increasing to between 25 and 50 keV at 1.9 MeV. The larger resolutions correspond to wider angle scatters in both cases, with each "dot" corresponding to a different specified detector angle.

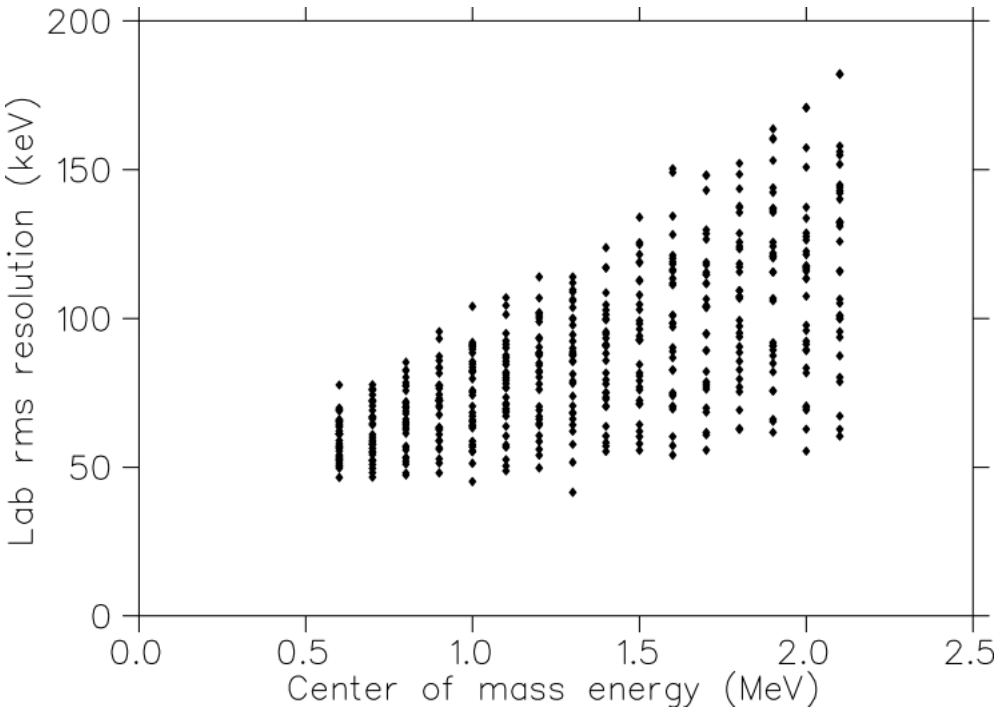

Figure 4.6 *The energy resolution plotted for a range of collision energies in the centre of mass frame, as produced by the Monte-Carlo code.*

Table 4.1 *Energy resolutions (rms, keV) found from Monte Carlo simulation for the $^{18}F(p,p)^{18}F$ and $^{18}F(p,\alpha)^{15}O$ reactions*

	^{18}F(p,α)^{15}O	^{18}F(p,p)^{18}F
Lab	55-110	35-37.5
C.M	7-13	3-5

The resulting centre of mass energy resolutions are given in table 4.1

4.1.5 R-matrix analysis

Interpretation of the data, aided by R-matrix calculations informed by previous results in the literature, revealed six further resonant structures present in the excitation functions. Their parameters are given in table 4.2, labelled B-F and H. In addition, there is also additional strength in the region of 1.3–1.7 MeV. An additional broad seventh state, here labelled G, has been included to account for this additional strength, based upon the predictions of Dufour and Descouvemont [57]. Due to the low statistics obtained from the experiment, projection of angular distributions was not possible. Hence, spin and parity assignments made here are inferred from previous works and remain tentative.

To extract best estimates of the parameters of the states forming these seven resonances, the data have been compared to R-matrix calculations of the excitation functions under various assumptions for the energies and partial widths for each state. The R-matrix calculations followed the standard theory of Lane and Thomas [44, 92] through the use of a multichannel R-Matrix code, with a channel radius of 5 fm, and an energy dependent energy resolution. The resolution varies linearly between the values noted in table 4.1. Events detected were spread over a range of angles, from $\sim$172° to 180° in the centre of mass. The value used for the calculations was, therefore, taken to be the average angle of all detector pixels, $\sim$176°.

At high energy in the elastic data, statistical variations and unknown contributions from higher energy resonances made it difficult to constrain the extracted parameters, such as those for resonance H which results in obvious structure in the inelastic reaction but less so in the elastic data. To account for this, the error bars associated with the points $E_{c.m} \geq 1.4$ MeV were increased such that the percentage error on each point was equal to that of the corresponding point in the inelastic data. That is, the statistical significance of these points in the

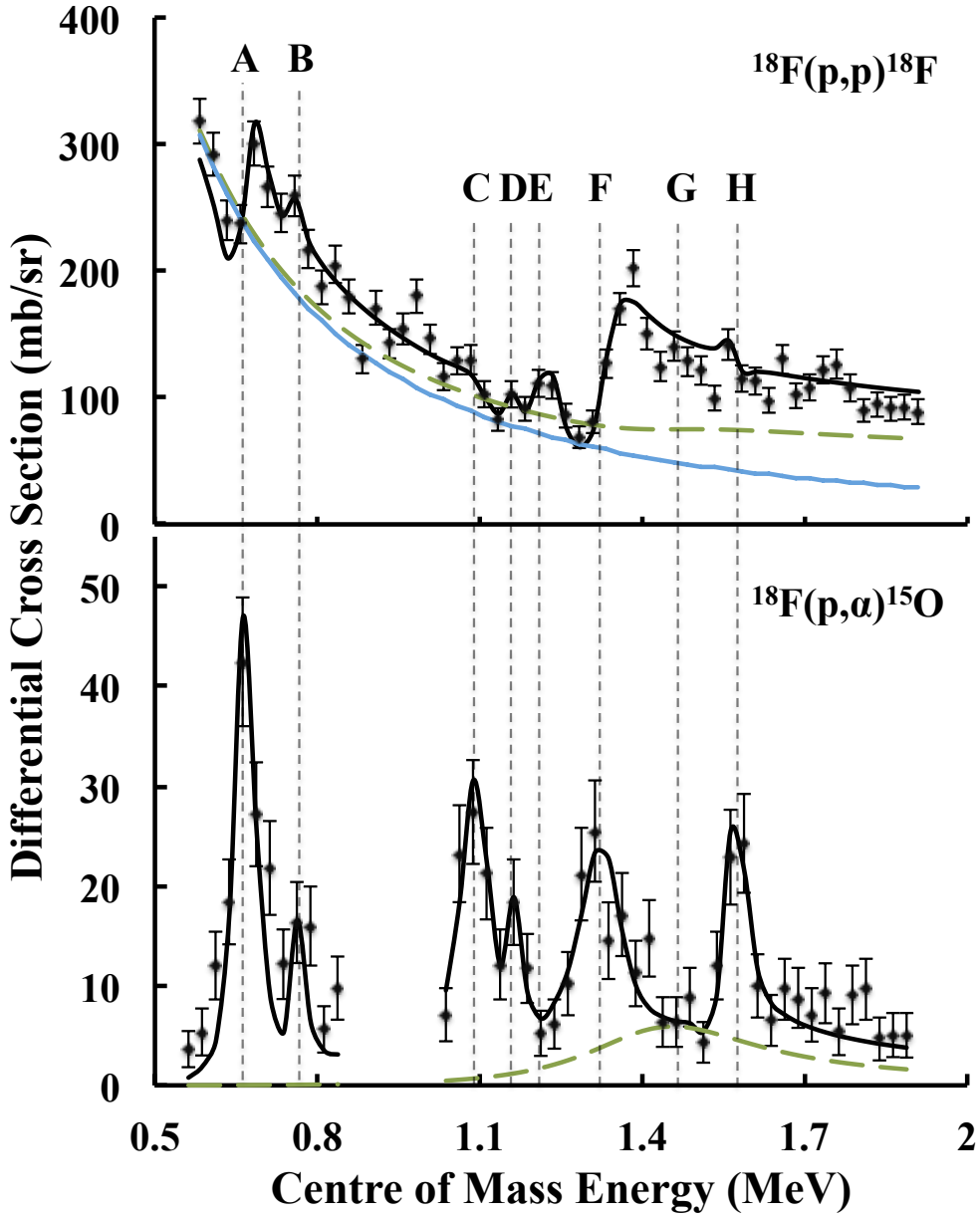

Figure 4.7 *Differential cross sections of both $^{18}F(p,p)^{18}F$ and $^{18}F(p,\alpha)^{15}O$ reactions as a function of centre of mass energy. A simultaneous R-matrix fit, calculated at a centre of mass angle of 176° is shown by the solid black line with the $^1/_2^+$ contribution shown in long-dashed green and (in the elastic scattering case) the Coulomb contribution is in pale blue. The $^1/_2^+$ contribution is consistent with a predicted broad state [57]. The combined fit has a $\bar{\chi}^2$ of 1.634*

Table 4.2 *Tabulation of the resonance parameters extracted from the present data when all resonances are allowed to vary within the minimisation procedure. The resulting R-matrix calculated excitation curves are shown in Figure 4.7. Also presented is a summary of previously reported parameters.*

	This work				Previous Results					
Resonance	E_{CM} (MeV)	J^π	Γ_p (keV)	Γ_α (keV)	E_{CM} (MeV)	J^π	Γ_p (keV)	Γ_α (keV)	Γ (keV)	Ref.
A[a]	0.665	$\frac{3}{2}^+$	15.2	23.8	0.6647(16)	$\frac{3}{2}^+$	15.2(1)	23.8(12)		[49]
B	0.759(20)	$\frac{3}{2}^+$	1.6(5)	2.4(6)	0.827(6)	$\frac{3}{2}^+$	0.35(35)	6.0(52)		[49]
					0.793(31)	$\frac{3}{2}^{(+)}$			35(12)	[61]
C	1.096(11)	$\frac{5}{2}^+$	3(1)	54(12)	1.089(9)	$\frac{5}{2}^+$	1.25(125)	0.24(24)		[59]
					1.092(30)	$\frac{5}{2}^{(-)}$			17(7)	[61]
					1.089(3)	$\frac{5}{2}^+$	1(1)	1.5(10)		[56]
D	1.160(34)	$\frac{3}{2}^+$	2.3(6)	1.9(6)	1.197(11)	$\frac{3}{2}^+$	2(1)	43(15)		[51]
					1.206(5)	$\frac{3}{2}^{(+)}$			21(10)	[61]
E	1.219(22)	$\frac{3}{2}^-$	21(3)	0.1(1)	1.233(12)	$\frac{1}{2}^-$	27(10)	16(6)		[51]
					1.233(18)	$\frac{3}{2}^-$	1(1)	3(3)		[56]
F	1.335(6)	$\frac{3}{2}^+$	65(8)	26(4)	1.347(5)	$\frac{3}{2}^+$	42(10)	5(2)		[56]
G	1.455(38)	$\frac{1}{2}^+$	55(12)	347(92)	1.452(39)	$\frac{1}{2}^{(+)}$			292(107)	[61]
H	1.571(13)	$\frac{5}{2}^+$	1.7(4)	12(3)	1.564(10)	$\frac{5}{2}^{(-)}$			11(8)	[61]
					1.573(8)	$\frac{1}{2}^+$	$8(^{+8}_{-4})$	34(13)		[56]

[a]Parameters of state A are constrained to those shown here to provide normalisation. Hence, no parameters or error bars have been extracted in the present work.

Table 4.3 *Covariance matrix for all parameters allowed to vary in the fitting process*

B			C			D			E			F			G			H			
E_{CM}	Γ_p	Γ_α	E_{CM}	Γ_p	Γ_α	E_{CM}	Γ_p	Γ_α	E_{CM}	Γ_p	Γ_α	E_{CM}	Γ_p	Γ_α	E_{CM}	Γ_p	Γ_α	E_{CM}	Γ_p	Γ_α	Par.
1	-0.51	0.99	0	0	0	0	0	0	0	0	0	0	0.02	0.02	-0.01	0.01	0	0	0	0	E_{CM} B
	1	-0.51	0.01	0.03	0	0	0	0	-0.01	0.07	-0.02	0	-0.08	0.01	0	-0.03	0.04	0	0	0	Γ_p
		1	0	0.01	0.01	0	0	0.01	0	0.01	0.01	-0.02	0.03	0.03	-0.02	0.01	0.02	0	0	0	Γ_α
			1	0.14	0.03	0.05	0.02	0.05	-0.02	0.01	0.50	-0.01	0.01	0.04	0.12	-0.14	0.02	-0.01	-0.02	-0.01	E_{CM} C
				1	-0.27	0.08	-0.02	0.07	-0.09	-0.05	-0.11	0.02	0.01	0.07	-0.27	0.21	0.25	0.09	0.05	0.11	Γ_p
					1	0.02	0.13	0.07	-0.01	-0.02	-0.05	-0.02	0.06	0.07	0.10	0.21	-0.25	0.12	0.11	0.22	Γ_α
						1	-0.78	0.99	-0.02	0.02	0.10	-0.03	0.08	0.08	-0.07	0.05	0.01	0	0	0	E_{CM} D
							1	-0.71	-0.04	0.15	0.07	-0.01	-0.04	0.02	0.02	-0.05	0.05	0	0	-0.01	Γ_p
								1	-0.01	0.02	0.17	-0.08	0.13	0.12	-0.07	0.03	0.03	0	-0.01	-0.01	Γ_α
									1	-0.11	0.11	-0.02	0.04	0.04	-0.13	0.03	0.10	0	0.01	0	E_{CM} E
										1	-0.29	0.01	-0.42	0.07	-0.13	0.03	0.06	0	0	-0.01	Γ_p
											1	-0.08	0.24	0.18	0.02	-0.46	0.27	-0.13	-0.20	-0.34	Γ_α
												1	-0.50	0.17	0.04	0.08	-0.22	0	0	0	E_{CM} F
													1	-0.02	-0.23	0.18	-0.08	-0.01	0.02	0.02	Γ_p
														1	-0.56	0.33	-0.08	-0.01	0.03	0.01	Γ_α
															1	-0.33	0	-0.33	0.22	0.19	E_{CM} G
																1	-0.69	-0.19	0.53	0.60	Γ_p
																	1	0.03	-0.41	-0.51	Γ_α
																		1	-0.63	-0.39	E_{CM} H
																			1	0.93	Γ_p
																				1	Γ_α

minimisation procedure was reduced so that it was equal to the significance of the inelastic points.

With this alteration, all resonances not associated with the well-known 665 keV state were free to vary. Resonance E was required to provide extra strength just below resonance F in energy but was significantly weaker in the inelastic data. As such, it was assigned an alpha width of 0.1 keV with a 100% error bar and constrained for the minimisation process.

At the end of the minimisation, the normalisation and energy offset was re-calibrated to the 665 keV resonance. This iterative process was repeated until no change was found to the best fit parameters in consecutive minimisation cycles.

Best Fit Parameters and Maximum Likelihood

The final parameters resulting in a minimum in the reduced χ^2 for the simultaneous fit to both data sets were searched for. In the region of minima, likelihoods were also calculated and it was observed that the maximum likelihood coincided with the minimum χ^2. This was tested by calculating the reduced χ^2 and likelihood values for many energies around the best fit energy of resonance C. Figure 4.8 shows that the location of maximum likelihood is consistent with the location of minimum χ^2.

The process has been repeated under alternative assumptions of angular momentum transfer and spin of the states, and for alternative possibilities for the signs of the interference between states of identical spin-parity. Under the condition that the widths and energies for all states (except the well-known $^3/_2{}^+$ state at 7076 keV) could vary freely, the parameter set resulting in the overall smallest reduced χ^2 is shown in Table 4.2. Additionally, previous measurements of the states observed here are noted in the table. It can be seen that the assigned parameters vary significantly between many of the measurements.

Error Analysis

The error estimation process used in the R-matrix code is described in [93], where it is shown that the error on parameter i is equal to the square root of the covariance matrix element, ii, assuming a diagonalised covariance matrix.

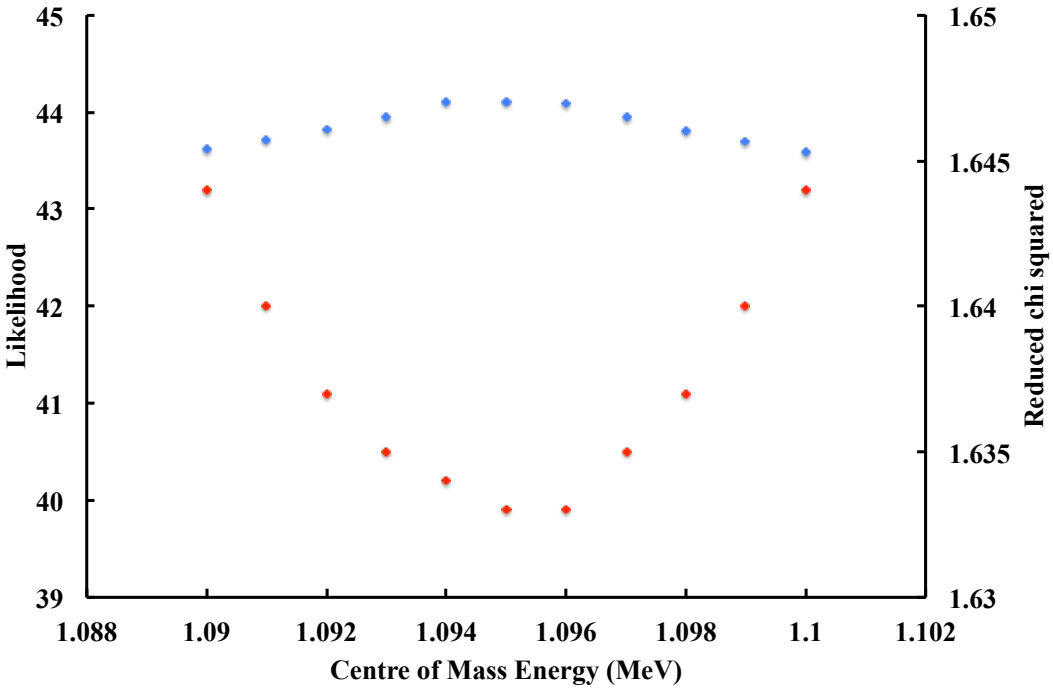

Figure 4.8 *Likelihood (blue) and reduced χ^2 (red) values for the energy of resonance C varied around the value of best fit.*

In general, however, the off-diagonal elements of a covariance matrix are large, meaning that this is not an accurate representation of the errors on the extracted parameters. Therefore, for completeness, the parameters and their errors must be presented in conjunction with the covariance matrix, as shown in figure 4.3. Unsurprisingly, several of the parameters appear to be strongly correlated, meaning the corresponding uncertainties are not independent.

In addition, it is noted that the errors extracted are also invalid unless the $\bar{\chi}^2$ is less than 1. Therefore, the suggested routine in [93] is applied where the error bars on data points are increased to give the best fit line a $\bar{\chi}^2$=1, and then the parameter error estimation routines of the code are reimplemented, generating revised estimates of the errors.

4.1.6 Results and Interpretation

The final extracted parameters, based upon previously observed parameters in the literature are presented in table 4.2 with the resulting cross sections shown in fig 4.7.

The feature labelled B is likely to be the resonance previously observed by Bardayan *et al.* [49], and by Dalouzy *et al.* [61]. The energy reported here is somewhat lower than previously observed, though it is poorly constrained as is illustrated by the large covariance between the energy and relative widths of this state.

Feature C has previously been observed several times [51, 56, 59, 61], but while there is reasonable agreement in energy and proton width, the present fit suggests a significantly broader alpha width than the earlier works, even given their disagreement. Re-analysis of the data in Murphy *et al.* [56] has revealed an ambiguity such that a significantly broader alpha partial width than reported would also adequately describe the structure. Based on two previous observations of a state with likely $J^{\pi}=3/2^{+}$ approximately 100 keV higher in energy [51, 61], resonance D has been included in our *R*-matrix calculations. The proton partial width for this state is in agreement with Utku *et al.* [51], but with a significantly narrower alpha width, and consequently a total width which is less than was found by Dalouzy *et al.* [61]. It seems likely therefore that features C and D are poorly resolved in this and other measurements, with both states having proton widths of order 1-3 keV and the sum of their alpha widths being of order 40-50 keV (assuming their spins are as stated). Curiously, table 4.3 suggests that the correlation between the extracted parameters for resonances C and D is low in the present measurement.

The strong feature at $E_{c.m.}$=1.2–1.4 MeV is well described by two previously observed states in ^{19}Ne, labelled here as E and F, but only when additional strength underlying these states is attributed to an additional broad state, labelled G, described shortly. States E and F match those previously observed at excitation energies of 7624 and 7748 keV [51, 56], where state F must have the opposite sign of interference to state A to adequately fit the data. Consistent with [56], state F was given a negative sign of interference while other $3/2^{+}$ states are assumed to have positive interference signs. Here the $J^{\pi}=3/2^{-}$ assignment is favoured for resonance E, as in Murphy *et al.* [56], although the proton and alpha widths are closer to those seen by Utku *et al.* [51] where an assignment of $J^{\pi}=1/2^{-}$ was proposed.

A further clear feature, H, is seen at about 1.571 MeV, and is here most well reproduced by a $J^{\pi}=5/2^{+}$ state. In the work of Murphy *et al.* [56] a resonance was seen at close to the same energy, but a $1/2^{+}$ assignment was found to best reproduce the data, although this was tentative due to the proximity of the state

to the upper energy limit of that experiment. Dalouzy *et al.* [61] also observed a state close to this energy, of somewhat smaller width, and made an unambiguous assignment of $^5/_2$ for the spin based on a parity independent angular distribution measurement: the parity was inferred on the basis of the lower centrifugal barrier for protons in the reaction being studied. In the present work, attempts to fit the data with a $J^\pi = {}^5/_2{}^-$ assignment are poor, strongly favouring the positive parity assignment.

As stated, a broad resonance, denoted G, has been included in the present work. Its contribution to the differential cross section of both reactions studied is illustrated by the dashed lines in Figure 4.7. Without the inclusion of this state, the best fit of the *R*-matrix calculations to the data is significantly worsened, especially in the higher energy region of the ^{18}F(p,α)^{15}O data. The overall reduced χ^2 value for the simultaneous fit to the entire data set changes from 1.634 to 2.483, and, considering only the data between 1.0 and 1.8 MeV, the reduced χ^2 changes from 1.306 to 2.486. Furthermore, the deduced parameters for resonances C, D, E, F and H depart significantly further from literature values. With the inclusion of resonance G, the best fit corresponds to a $J^\pi = {}^1/_2{}^+$ state at an excitation energy of 7870±40 keV with a proton partial width of 55±12 keV and an alpha partial width of 347±92 keV. The extracted parameters show quite strong correlations with those extracted for resonances F and H. The data are consistent with the presence of the state predicted by Dufour and Descouvemont [57] and observed by Dalouzy *et al.* [61].

Finally, it has been found that the incorrect angle has been used for the cross section calculations made here. The calculated centre of mass cross section for the elastic scattering data corresponds to an angle of ∼2.2° instead of the required average angle of ∼4.4° on the detector. In the vicinity of the $^5/_2{}^+$ resonance at $E_{c.m.}$ ∼1.57 MeV, the differential cross-section, found from the *R*-matrix formalism, of the ^{18}F(p,p)^{18}F reaction does not vary over the range of the detector from a value of 133 mb/sr.

For the ^{18}F(p,α)^{15}O data, the centre of mass angle used in the above calculation corresponds to a scattering angle of θ_{lab} ∼1.5° and the differential cross section is calculated to be 20.0 mb/sr at this angle. θ_{lab}=4.4° gives a centre of mass angle of 169° resulting in a differential cross section of 18.8 mb/sr. This shows that the variation in cross section with angle in the region of the high spin resonance at $E_{c.m.}$=1.571 MeV shows a reduction of ∼1 mb/sr between θ_{lab}=1.5° and 4.4° in the ^{18}F(p,α)^{15}N reaction differential cross section. This level of variation is similar

to or smaller than the existing level of uncertainty in the results, therefore, the conclusions presented here remain valid.

4.1.7 Astrophysical Implications

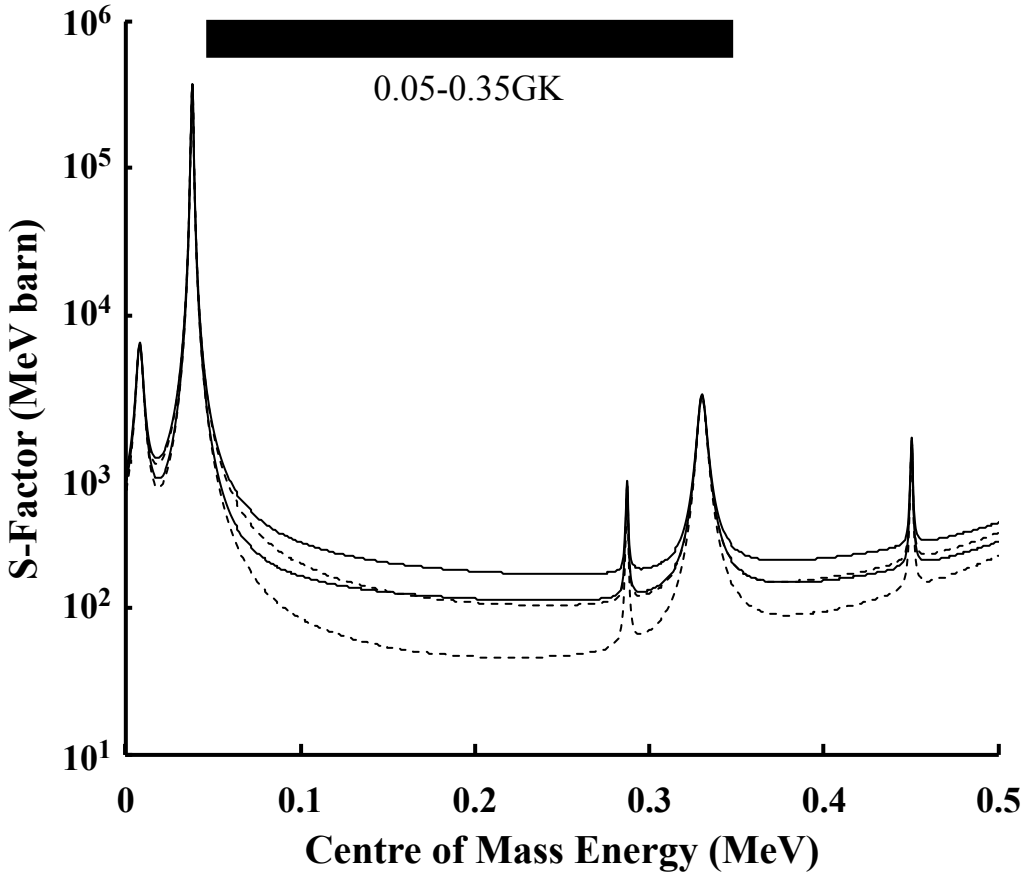

Figure 4.9 *The Astrophysical S-factor for the $^{18}F(p,\alpha)^{15}O$ reaction. The dashed lines are the astrophysical S-factor arising from interference combinations giving the highest and lowest values in the astrophysical region based on the parameters recommended by Iliadis* et al. *[58]. The addition of the predicted sub-threshold $J^{\pi}=1/2^{+}$ state [57] significantly enhances the S-factor, as shown by the solid lines.*

The apparent existence of the broad state G supports the prediction of an additional broad $1/2^{+}$ state below threshold. The impact of such a state is illustrated in Figure 4.9, where the astrophysical s-factor most recently recommended by Iliadis *et al.* [58] is shown, together with the same s-factor modified by the inclusion of the proposed sub-threshold $1/2^{+}$ state with parameters as suggested by [57]. The two curves shown in each case correspond to the highest and lowest s-factors allowed due to the uncertainty in the interference between

the 38 and 665 keV $J^{\pi}=3/2^{+}$ states. Within the Gamow window, the astrophysical s-factor is increased, is more tightly constrained, and the possibility of strongly destructive interference, as highlighted by de Séréville *et al.* [62] is removed. The lowest energy measurement to date [65] was at 250 keV, with an s-factor of 105^{+118}_{-60} MeV b, in good agreement with this result.

4.2 $^{18}\mathrm{O}(\mathrm{p},\alpha)^{15}\mathrm{N}$ Analysis and Results

This section describes the extraction of excitation spectra from the data collected in the study of the ^{18}O(p,α)^{15}N reaction, and the ensuing data analysis. Events are selected by their energy and time of flight, as shown in figure 4.10, and sorted into centre of mass exciatation functions. The R-Matrix formalism has been employed to extract resonance parameters from the excitation spectra in a region of significant uncertainty.

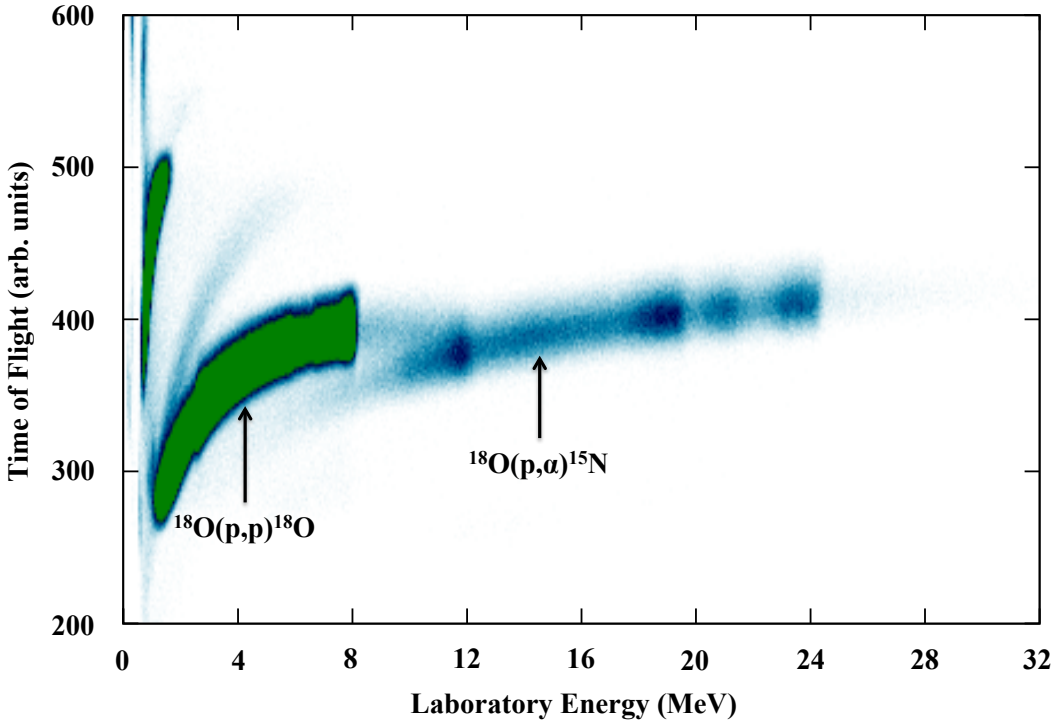

Figure 4.10 *The time difference between events occurring in the detector and the next beam pulse as a function of the detected particle energy. Two loci are observed: a proton locus (left), an alpha particle locus (middle).*

4.2.1 Energy Loss and Final Calibration

For the ^{18}O(p,α)^{15}N reaction, the same energy loss and conversion to centre of mass has been performed as for ^{18}F(p,α)^{15}O reaction. The LEDA angles are input to the code and lookup tables produced for many beam energies through the target. These can then be used to convert an event with specified particle type, energy deposited and detection angle to a centre of mass energy through linear interpolation. Again, the relative quenching effects have been included prior to transformation.

This process was also successful as a final stage calibration of the experiment as there was no known target measurements to draw upon. The centre of mass energy of the beam is the maximum centre of mass energy available for reactions, and as such there is a high energy "edge" in any extracted spectra. The experimental beam energy could be found by varying the target thickness and beam energy within the conversion program until the beam energy agreed with this high energy edge and this was consistent between all returned spectra. As such, the beam energy was found to be 42.5 MeV ($E_{c.m.}$= 2.25 MeV) upon entry to the target which was 57.8 μm thick. The intention of this study is to constrain the parameters of resonances observed up to around $E_{c.m.}$ = 1 MeV, so upon analysis, the excitation spectra are limited to this region of interest for the time being.

The relatively low rate of alpha particles precluded any considerations of angular distribution studies. As such, one single excitation spectrum was extracted for all α-particle events across the LEDA detector and considered at the weighted average scattering angle. The high rate of proton events, however, could allow for an investigation of angular distribution effects. Multiple proton excitation spectra, however, would result in a statistical bias towards effects observed in these spectra. As such, for this initial analysis, the spectrum associated with the annulus closest to the average angle (as used for the α-particle events) was selected for further study. These spectra can be seen in figure 4.16.

4.2.2 Background Subtraction

Alpha Background

Unlike in the case of the ^{18}F(p,α)^{15}O reaction, the energy-time of flight plot, see figure 4.10, shows a significant fusion-evaporation tail on the α-particle events. Therefore, the maximum energy of the beam used to build the lookup tables is increased so that the resulting excitation spectrum will include a tail of fusion-evaporation α-particles to guide the background subtraction.

To understand the shape of the fusion evaporation under the structures in the excitation spectrum, an experimental run with the polyethylene target replaced by a thick carbon target was studied, and the energy-time of flight plot is shown in figure 4.11. Gating on the α-particle locus, the same event-by-event analysis was implemented to the data and the resulting figure is shown in figure 4.12.

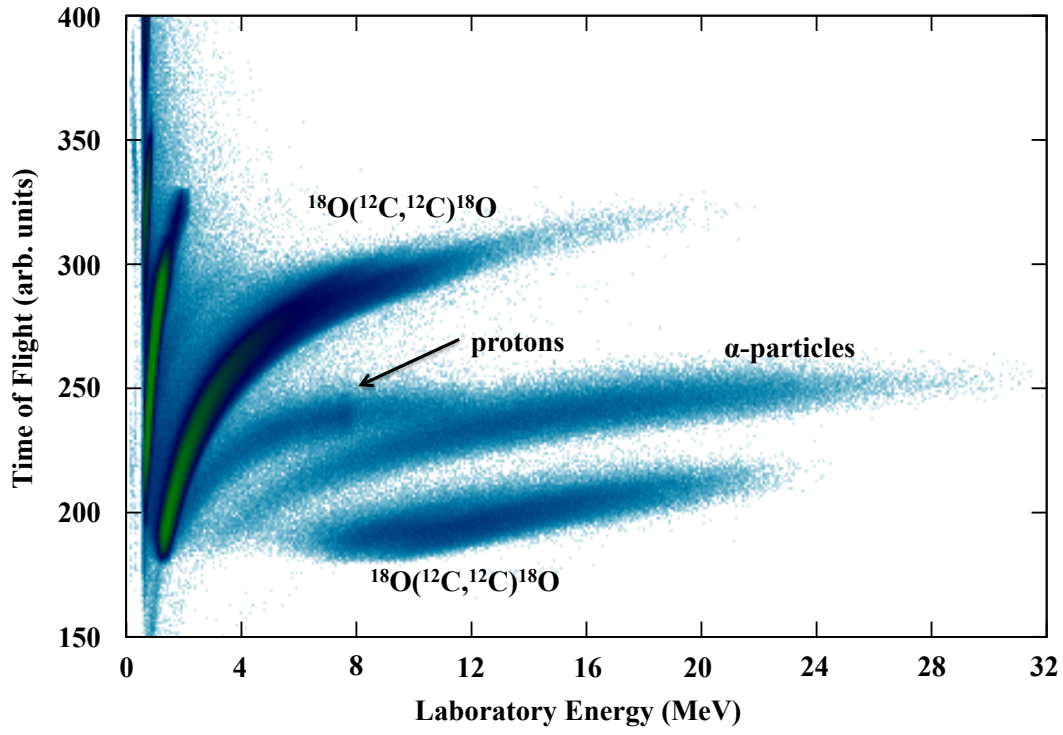

Figure 4.11 *The time difference between events from ^{18}O on a carbon target occurring in the detector and the next beam pulse as a function of the detected particle energy. Many loci are observed: a proton locus, an alpha particle locus and elastic scattering events on the ^{12}C ions.*

This shape is best described by two functions which cross over at a point around

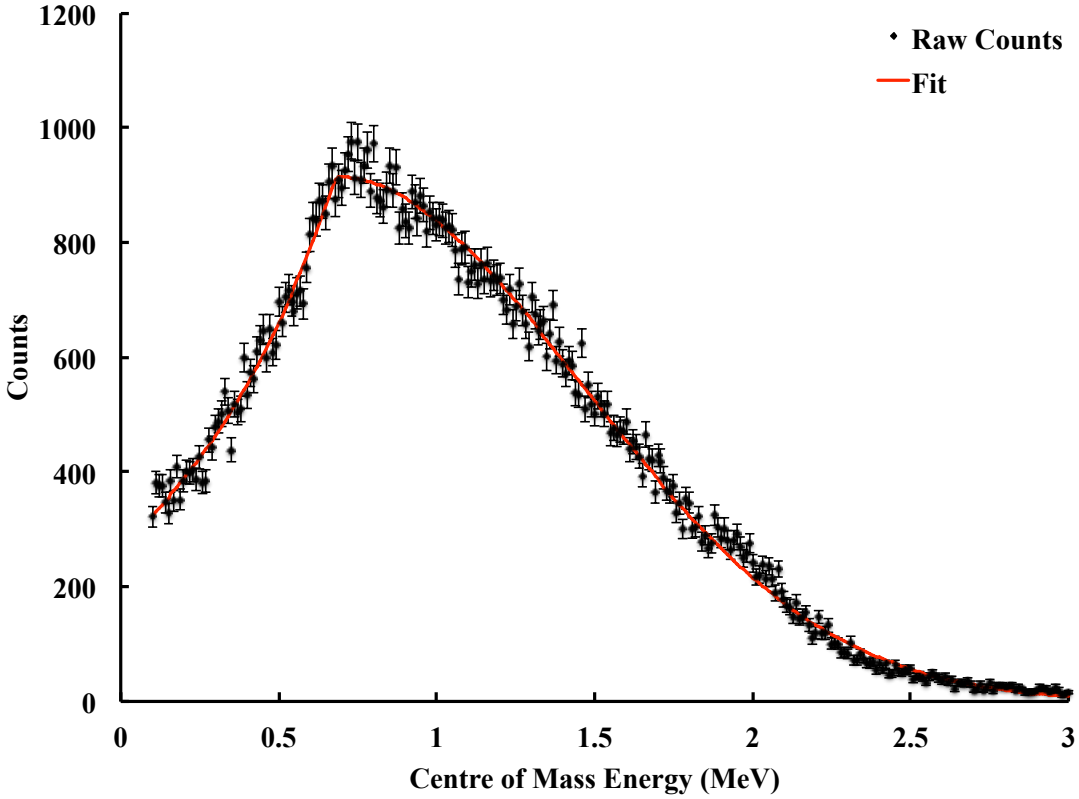

Figure 4.12 *Events observed at the location of the α-particle locus when a pure carbon target is placed at the target position. The distribution is fitted with two functions either side of the apparent peak at around 0.7 MeV.*

the peak at ∼0.7 MeV in figure 4.12. On the left side of the crossover, the shape is best described by the simple exponential function in equation 4.2a. On the right side, the function has a Maxwell-Boltzmann type shape, characterised by the function in equation 4.2b. The values A, B, C, D and F are parameters free to vary to obtain a best fit as shown in figure 4.12.

$$b = Ae^{BE_{c.m.}} \tag{4.2a}$$

$$b = CE_{c.m.}^{D} e^{FE_{c.m.}^{2}}. \tag{4.2b}$$

To obtain the cross over point, the difference between the functions is calculated and the cross over point selected where this is a minimum. The best fit functions are then found and the global χ^2 calculated. This process is repeated and the global χ^2 compared to the previous value until either the minimum χ^2 corresponds

to the location of the difference minimum, or no improvement can be made to the χ^2 value.

Upon application to experimental data, there are some features in the excitation spectra which can be used to guide the background fit. The event-by-event conversion tables were extended to include events beyond the high energy beam edge. This produces a tail on the end of the data which guides the high energy tail of the fusion evaporation. In addition, the cross over point is also obvious in the alpha spectrum between $E_{c.m.}$ ~0.85 - 1.4 MeV.

Fitting the above functions to these points, and proceeding as before with reference to the cross over point, the background effects can be estimated as shown in figure 4.13.

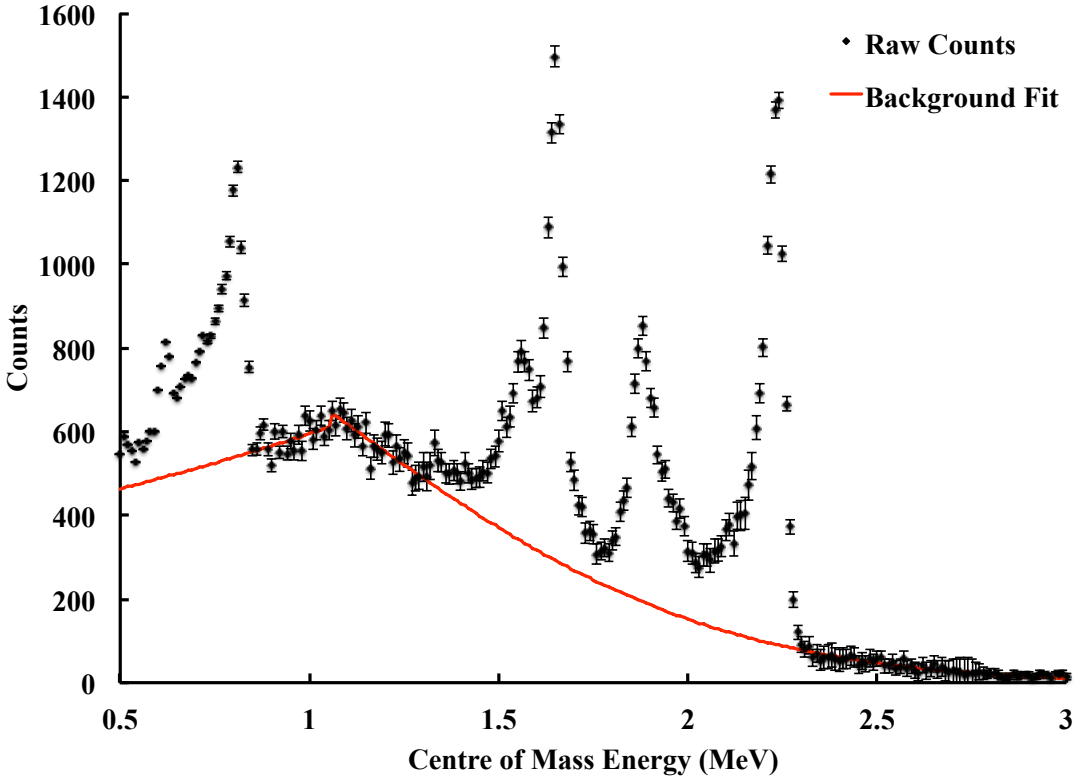

Figure 4.13 *Events found in the α-particle locus with the fusion evaporation background estimate shown.*

Proton Background

Similar to the α-background, the proton background was investigated with a carbon target replacing the polyethylene and, by gating on the proton locus in

figure 4.11, the resulting events are shown in figure 4.14. In this case, the fusion evaporation is well described by a first order polynomial, with a small negative gradient. The additional events above the high energy edge in the experimental data, as shown in figure 4.15, follow a similar trend and can be considered the high energy fusion evaporation events. As such, the small number of fusion-evaporation events is negligible compared to events of interest and no subtraction is required.

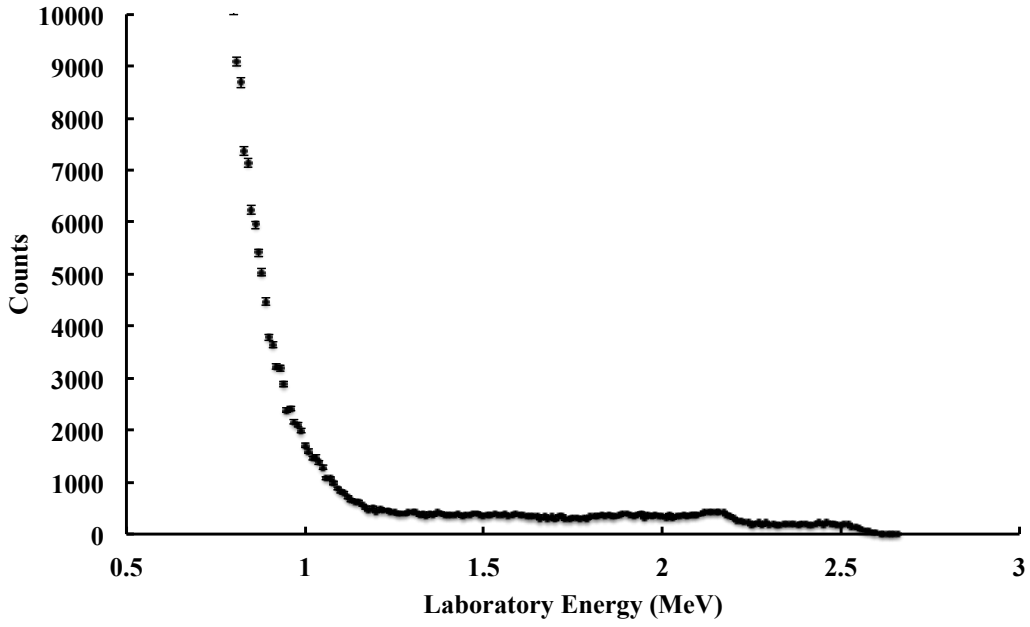

Figure 4.14 *Events observed at the location of the proton locus when a pure carbon target is placed at the target position.*

At low energy in figure 4.14, there is an additional contribution to the background. Comparing this with figure 4.10, it appears likely that these events come from wrap around of elastic scattering events on the ^{12}C ions in the target. By comparing figures 4.10 and 4.11, it is clear that such events are much diminished from the polyethylene target such that the lower locus is no longer visible in figure 4.11. As such, these events make an insignificant contribution to the yield in the experimental data from the polyethylene target with any contribution only likely to effect events below $E_{c.m.} \sim 0.7$ MeV. Hence, these background events can also be discounted from further consideration.

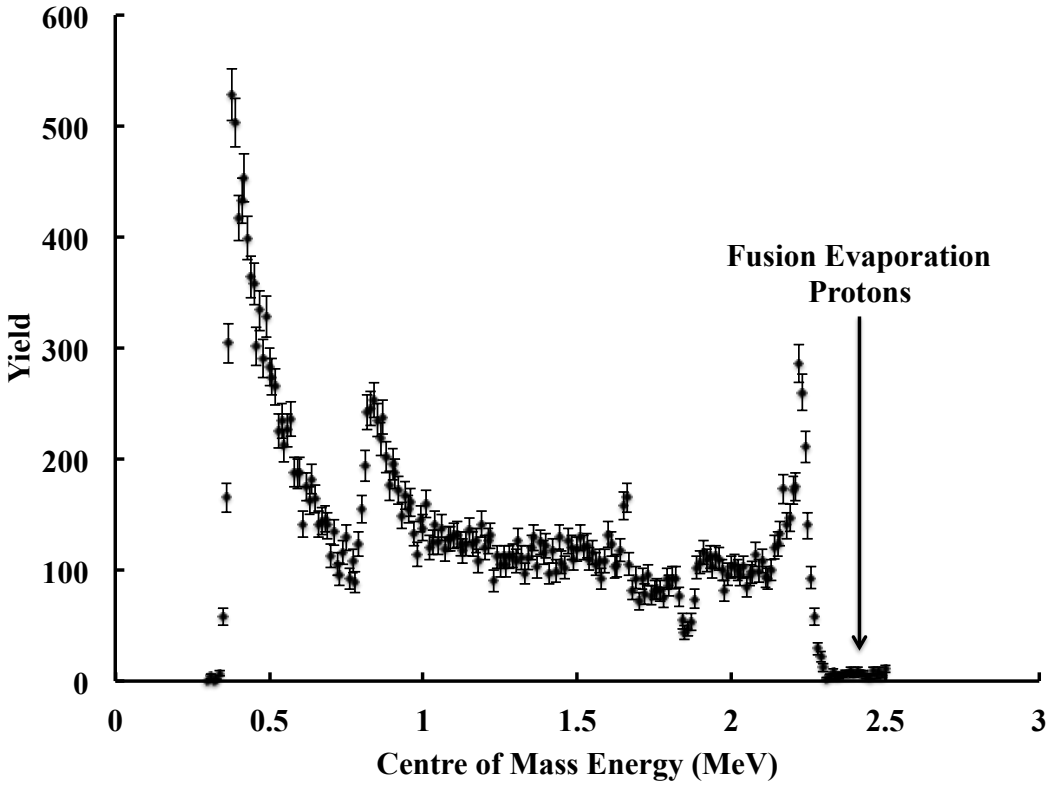

Figure 4.15 *A sample spectrum, taken from annulus 3 of LEDA, of good proton events in the $^{18}O(p,p)^{18}O$ reaction. The high energy fusion evaporation events are shown.*

4.2.3 Cross-section Calculations and Excitation functions

The cross section calculation was again based on equation 4.1 where the number of projectiles was estimated from the TRIUMF Faraday Cup measurements. All other values were calculated as before, aided by `SRIM2008` [81] calculations. In order to account for discrepancies in the Faraday cup measurements and any additional detector efficiency or dead time effects, the cross section of each elastic scattering data set in the non-resonant low energy region from 0.5-0.6 MeV was scaled to the R-matrix calculation in this region. The scale factors are given in table 4.4 and the average taken. This value is assumed to be independent of energy and particle type as it is likely to include such effects as Faraday Cup variation and dead time. The final scale factor was found to be 2.95(7).

Applying this scale factor to both excitation spectra produced absolute cross section calculations for the ^{18}O(p,p)^{18}O and ^{18}O(p,α)^{15}N reactions.

Table 4.4 *Scale factors calculated from the non-resonant region of the elastic scattering excitation functions.*

Annulus	Scale Factor
0	2.94
1	2.81
2	2.47
3	2.92
4	2.62
5	2.93
6	3.09
7	3.08
8	3.20
9	3.24
10	3.11

4.2.4 R-Matrix Analysis

The following R-matrix analysis was carried out using the new C++ code available from JINA [94], referred to as `AZURE2`. Experimental parameters were fitted to the spectra presented in figure 4.16. As was noted by Mak *et al.* [74], the resonances at around 650 keV and 800 keV are required to interfere destructively, that is that they have opposite interference terms within the R-matrix formalism. The excitation energy and partial widths for each of the three states of interest were initially taken from those reported by Tilley *et al.* [71] and all were allowed to vary freely. As no angular distribution have been included as yet, spin-parity assignments have been taken as read from [71].

Resolution effects are included in the fit through a Gaussian convolution, of specified width, *i.e.* the resolution, with the calculated cross section. No simulations had been carried out on the experimental setup as with the previous reaction, so the resolution was estimated through an iterative process. Starting with nominal resolution of 5 keV for the proton data and 10 keV for the α-particle data, a full χ^2 minimisation was carried out and the minimum values noted. The resolution was then varied and another minimisation carried out to check for a better fit. This iterative process was repeated until no better fit was found. The resulting resolutions were 7 keVc.m. for the proton data and 11 keVc.m. for the α-particle data, both reasonable values.

The error analysis was carried out by AZURE using the MINOS function from MINUIT [95]. This function, discussed further in chapter 5, searches the

parameter space for uncertainty contours consistent with being 1σ from the optimum parameter set. This occurs at the point where $\chi^2 = \chi^2_{min} + \Delta\chi^2$. $\Delta\chi^2$ is calculated from the normal distribution for the point where $\Pr(\chi^2_{min} - \Delta\chi^2 < \chi^2 < \chi^2_{min} + \Delta\chi^2) = 68.27\%$, 10.4 in this case for nine free parameters.

The parameters extracted as a result of this fitting are presented in table 4.5 and the fitted cross-sections are included in figure 4.16. Each resonance will now be discussed.

Table 4.5 *Tabulation of the resonance parameters extracted from the ^{18}O data when all resonances are allowed to vary within the minimisation procedure. The resulting R-matrix calculated excitation curves are shown in Figure 4.16.*

J^π	E_x (MeV)	$E_{c.m.}$ (keV)	Γ_p (keV)	Γ_α (keV)	Int.
$\frac{3}{2}^-$	8.608*	613*	<0.35	<0.51	+
$\frac{1}{2}^+$	$8.615\binom{+42}{-30}$	$620\binom{+42}{-30}$	$10\binom{+1}{-3}$	$189\binom{+65}{-35}$	+
$\frac{1}{2}^+$	8.812(5)	817(5)	20(2)	28(6)	-

The low-energy $^3/_2{}^-$ resonance was observed at an excitation energy of 8.608 MeV, corresponding to a centre of mass energy of 613 keV. The MINOS [95] error analysis used in AZURE became unconstrained when searching for an uncertainty on this value, and therefore no uncertainty was extracted. This is most likely due to the lack of a feature attributed to this resonance in the elastic scattering channel. It is clear in the (p,α) channel, however, and this likely contributes most to the extracted parameters associated with this resonance. The uncertainty surrounding the resonance width is furthered by the near 100% error bars returned by the AZURE program. As such, presented here are upper limits to the partial widths. Even so, these results imply a slightly narrower resonance than previously thought, around 15 keV higher in energy.

The broad resonance previously observed at around 650 keV was suggested to have a significantly lower resonance energy by La Cognata *et al.* [78] using the Trojan Horse Method, and such a broad resonance is likely to have an uncertain energy due to its rather uniform contribution across the energy range. It had been previously reported at approximately 658 keV above the reaction threshold by Tilley *et al.* with Γ_p=5 keV, Γ_α= 95 keV and Γ=340 keV. This present study finds the resonance at E_x = 8.615 MeV, 620 keV above the proton threshold. The reported error bars make this measurement consistent with both the Tilley *et al.* report and the work of La Cognata *et al.*, both lying within 1σ. In addition, the partial widths are consistent across all publications. As such, it is clear

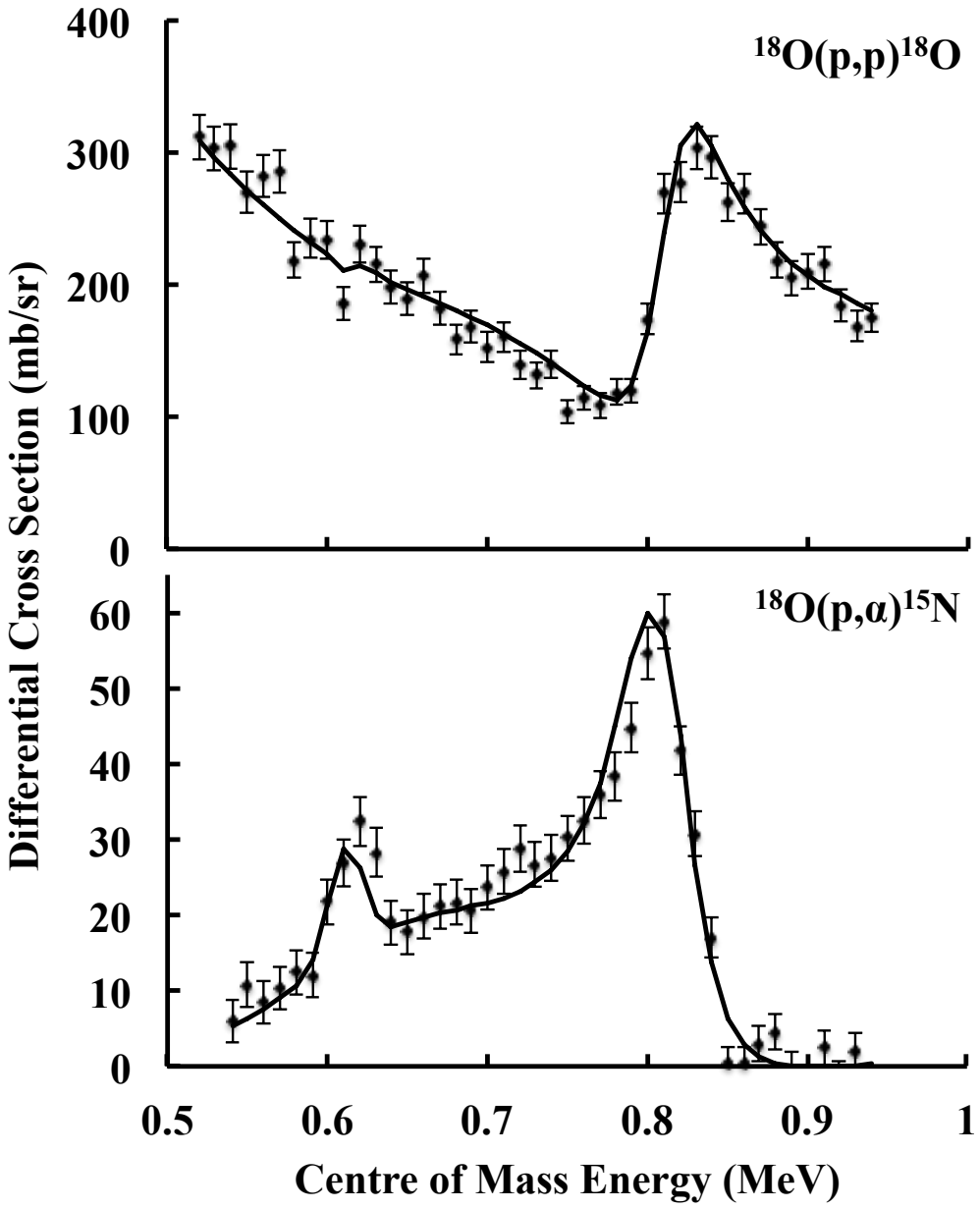

Figure 4.16 *Differential cross sections of both $^{18}O(p,p)^{18}O$ and $^{18}O(p,\alpha)^{15}N$ reactions as a function of centre of mass energy. A simultaneous R-matrix fit is shown by the solid black line. The combined fit has a $\bar{\chi}^2$ of 2.101*

that the resonance must be narrower than originally found by Lorenz-Wirzba *et al.* [75] and the widths are now relatively well constrained. The resonance energy, however, remains poorly constrained over this region.

Finally, the resonance at around 800 keV is considered. This work again finds the state to be higher in energy than measurements prior to the Tilley *et al.* report [71], at E_x = 8.812 MeV, or 817 keV above the proton threshold. This is, however, consistent with the measurement made by La Cognata *et al.* [78]. The widths measured here are consistent with those reported by Tilley *et al.* [71], ruling out the broader measurement by La Cognata *et al.* [78].

4.2.5 Astrophysical Implications

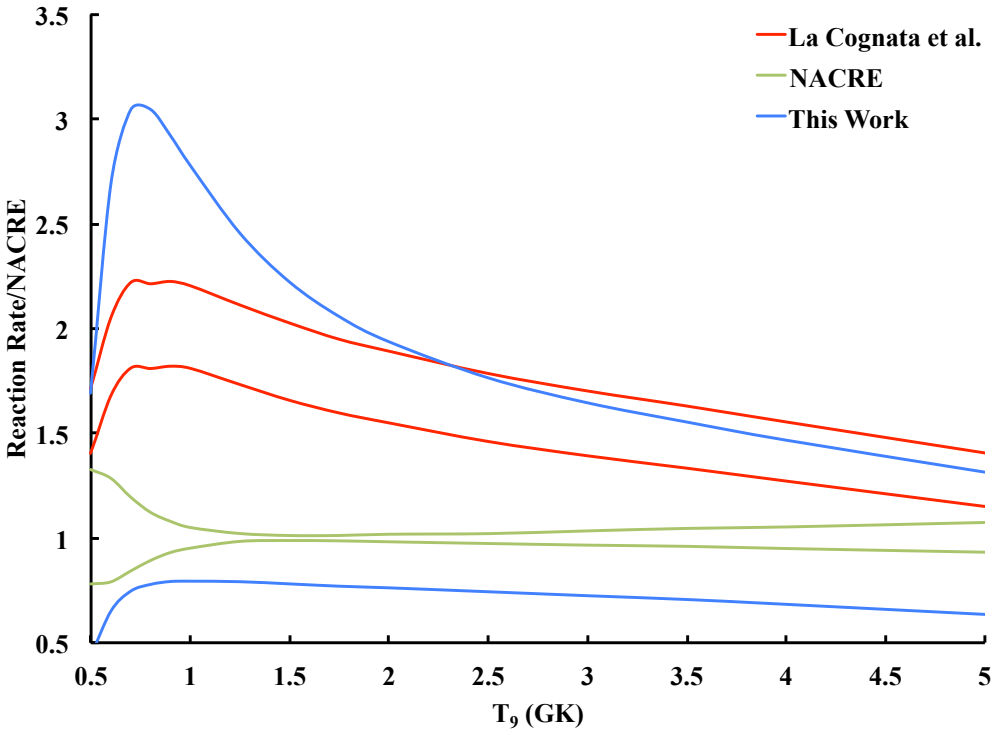

Figure 4.17 *The $^{18}O(p,\alpha)^{15}N$ reaction rate ranges as a ratio to the adopted NACRE rate [67]. The red line is the upper and lower limits as calculated by La Cognata* et al *[78] based on the parameters extracted through their Trojan Horse measurements, the green line is the upper and lower bounds of the NACRE reaction rate [67] and the blue lines are the limits based on the parameters extracted here, calculated using* `AZURE2`.

The results of La Cognata *et al.* significantly increased the reaction rate of the $^{18}O(p,\alpha)^{15}N$ reaction above T_9=0.5 GK, as shown in figure 4.17. The rate is

increased relative to the accepted NACRE [67, 96] value by a factor of two at some points. This NACRE rate does not take into account the significant uncertainties on any measurements of the broad $^1/_2{}^+$ resonance, instead averaging over the resulting rate from Lorenz-Wirzba *et al.* [75] and Yagi *et al.* [73]. This has resulted in a narrow window of possible reaction rates in the $0.5<T_9<5$ GK window. Similarly, the over-precise measurement of La Cognata *et al.* [78], discussed in section 2.2, has resulted in a narrow range of possible reaction rates. As this state underlies two narrower states, accurate direct measurement of its properties is problematic, and as such the error bars are large.

The reaction rate has been calculated based on the parameters extracted in this work using `AZURE2`. The uncertainty over the broad $^1/_2{}^+$ resonance has resulted in a broad range of possible reaction rates, encapsulating both the NACRE accepted and La Cognata reaction rates. At high temperature, the upper limit of the La Cognata rate is ruled out due to the narrower measurement of the higher energy $^1/_2{}^+$ resonance at 817 keV. At present, however, it is not possible to constrain the reaction rate further at lower temperatures.

Chapter 5

Testing the R-Matrix formalism and its implementation

The R-matrix formalism, generalised for nuclear reactions by Lane and Thomas [44], is enjoying a renaissance in nuclear astrophysics studies. The complex formalism both aids the extraction of experimental parameters through fitting of experimental data and allows the cross sections to be extrapolated into low-energy, experimentally challenging, regions which are often of most interest.

5.1 Strong Nuclear Force

The R-matrix formalism seeks to provide a solution to the uncertainty surrounding the strong nuclear force which makes resonant cross section calculations challenging. From experimental observations certain aspects of the strong nuclear force have been derived and empirical relationships found to characterise it, such as the Argonne AV18 potential shown in figure 5.1 [97]. This was obtained from fitting the resulting scattering parameters to p-p and n-p scattering data [98].

Figure 5.1 shows the general form of the strong nuclear potential. The force is repulsive at very short range and attractive beyond around 0.75 fm. It is, in general, a short range interaction, proven by scattering experiments such as those in [98], only taking place at low impact parameters. Therefore, beyond the nuclear radius the strong nuclear force is negligible and a system is dominated by the Coulomb interaction [100]. The motivation behind the derivation of the

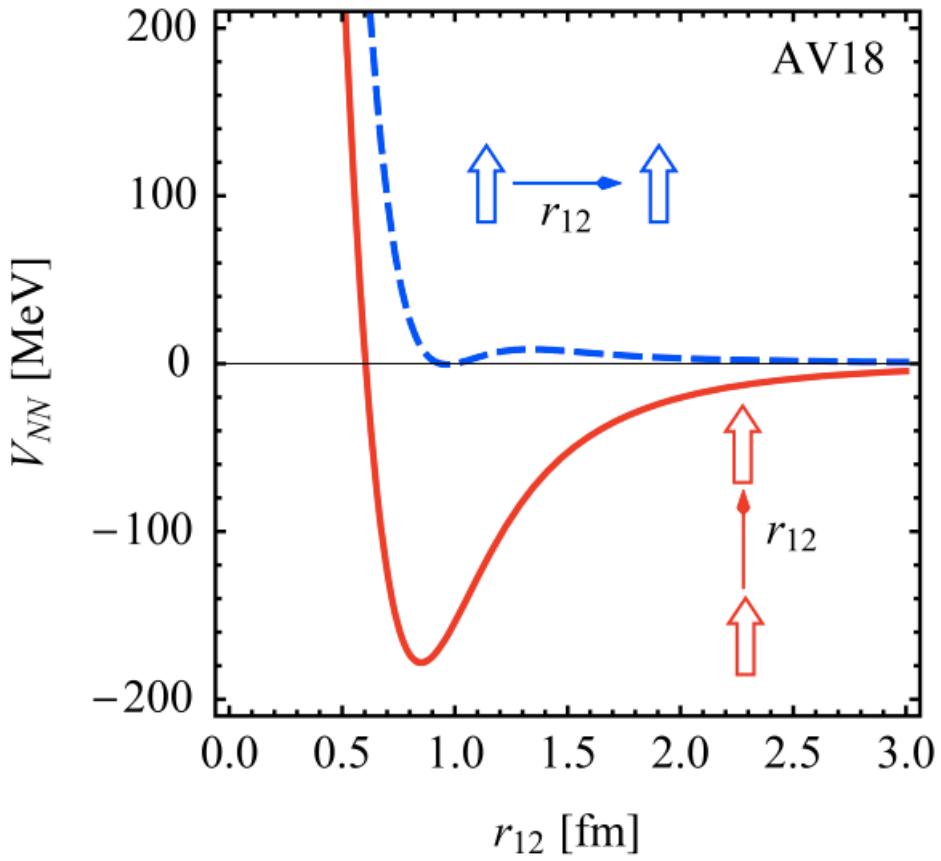

Figure 5.1 *The AV18 Potential for the case where the two nucleons have their spins aligned with the separation vector and the case where the nucleon spins are perpendicular to the separation vector [99]*

R-matrix formalism is to parameterise the nuclear force in terms of the external Coulomb effects and achieve better estimates of nuclear parameters as a result.

5.2 The Phenomenological R-Matrix Formalism

The basis of the R-matrix formalism is that one can separate a compound nuclear reaction system into two distinct regions, specifically, the internal region where the strong nuclear force dominates, and the external region where the Coulomb force dominates. The boundary between these regions is chosen such that the strong nuclear force is negligible outside this radius. Physically, entrance to the internal region can be by numerous channels defined by particle pair, spin coupling and angular momentum transfer, as shown in figure 5.2. Discussed here is the evolution of the phenomenological R-matrix [92, 101, 102], useful for cross-section calculations and the extraction of parameters from experimental data. There also

exists a "calculable" R-matrix which is useful for the prediction of cross-sections and resonance parameters [92].

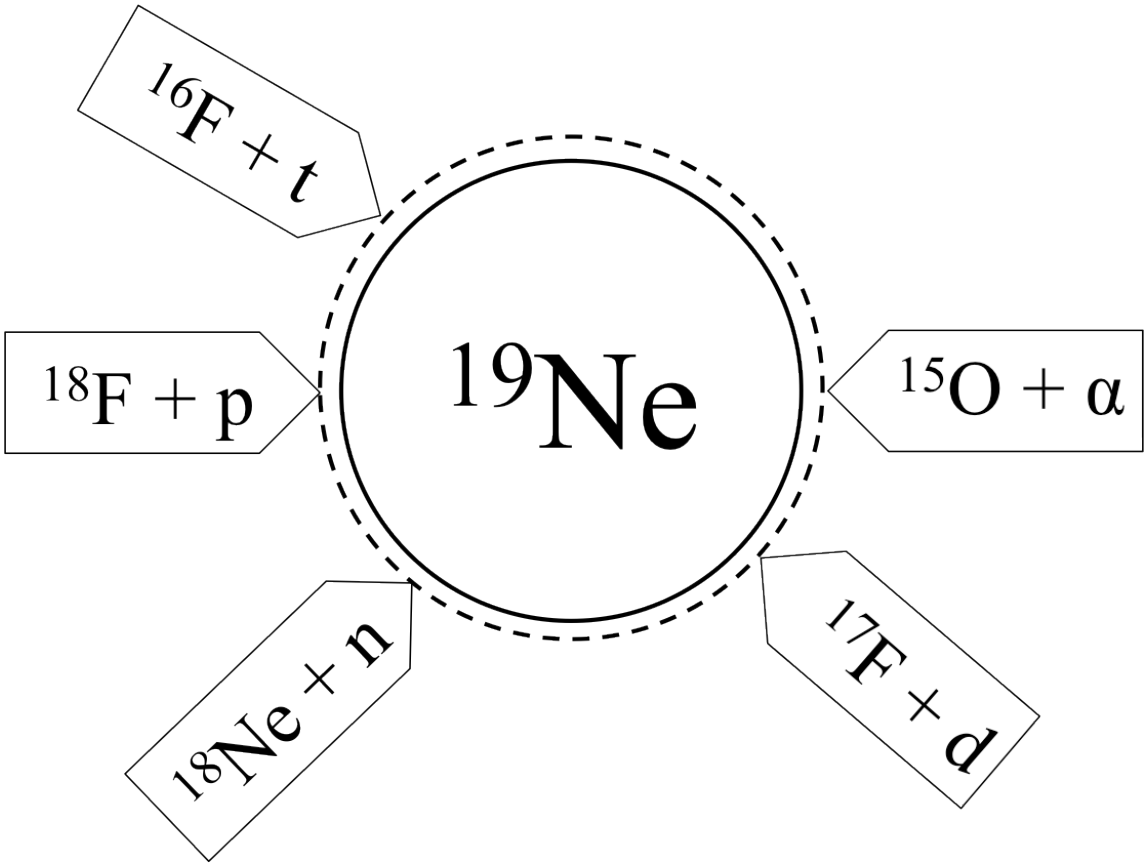

Figure 5.2 *An example of a nuclear reaction system separated into internal and external regions for use in the the R-Matrix formalism. The R-Matrix boundary (dashed line) is defined as the range of the nuclear strong force, with a radius just larger than the compound nucleus.*

Experimental studies of interest to nuclear astrophysics make use of unpolarised ion beams at non-relativistic, low, energies. With this in mind, one can consider the experimental system in the non-relativistic regime. In the internal region, the wavefunction satisfies the Schrödinger equation, but the solution is not known, while in the external region the solution is based upon the well-known Coulomb wavefunctions. The wavefunction in the internal region can be written in a general way as an expansion of all entrance (or exit) channels:

$$\Psi = \sum_c \psi_c \phi_c \tag{5.1}$$

where ψ indicates the angular component and ϕ indicates the radial component of

the wavefunction. This can also be expanded in terms of levels in the nucleus [44]:

$$\Psi = \sum_{\lambda} C_{\lambda}\chi_{\lambda} \tag{5.2}$$

where the coefficients can be given by:

$$C_{\lambda} = \int \Psi\chi_{\lambda}^{*} dV. \tag{5.3}$$

Substitution into Schrödinger's equation, with a Hamiltonian comprising kinetic and potential energy components, and solving the integral through Green's Theorem gives the expression:

$$\sum_{c} \frac{-\hbar^2}{2m_c} \int dS_c \psi_c \chi_{\lambda}^{*} \left[\frac{\phi_c}{\chi_{\lambda}^{*}} \frac{d}{dr}\chi_{\lambda}^{*} - \frac{d}{dr}\phi_c \right] = (E_{\lambda} - E)C_{\lambda} \tag{5.4}$$

making the assumption that the internal region is entirely enclosed by a spherical surface.

Hence, the coefficients can be identified and, by defining the "boundary condition":

$$b_c = \frac{r_c}{\chi_{\lambda}^{*}} \frac{d\chi_{\lambda}^{*}}{dr} \tag{5.5}$$

and the "reduced width amplitude":

$$\gamma_{\lambda c} = \left(\frac{\hbar^2}{2m_c r_c} \right)^{\frac{1}{2}} \int dS_c \psi_c \chi_{\lambda}^{*} \tag{5.6}$$

one obtains an expression for the expansion of the wavefunction in the first form:

$$\phi_c \left(\frac{\hbar^2}{2m_c r_c} \right)^{\frac{1}{2}} = \sum_{\lambda} (E_{\lambda} - E)^{-1} \sum_{c'} \left(\frac{\hbar^2}{2m_{c'} r_{c'}} \right)^{\frac{1}{2}} \gamma_{\lambda c}\gamma_{\lambda c'} \left[r_{c'}\phi'_{c'} - \phi_{c'} b_{c'} \right]. \tag{5.7}$$

One then observes that all spherical components of the wavefunction have been

absorbed by the reduced width amplitudes, logarithmic derivative, ϕ', and boundary condition. Here, λ denotes the energy level while c and c' denote the entrance and exit channels.

Hence, one can identify the "R-matrix":

$$R_{cc'} = \sum_{\lambda} \frac{\gamma_{\lambda c}\gamma_{\lambda c'}}{E_\lambda - E} \tag{5.8}$$

which is defined for each partial wave and has a matrix element for each channel pair. For example, in the earlier study in this work of the ^{18}F(p,α)^{15}O reaction, elastic scattering data were also analysed with resonances in five different spin-parity groups. Hence, the overall calculation would have required five 2×2 R-matrices.

Now, in the external region of the system, the complete wavefunction can be expressed as the combination of the incoming and outgoing waves, I and O, which depend on the Coulomb wavefunctions F and G [103]. This eventually allows the radial portion of the external wavefunction to be expressed as:

$$\phi_c = \frac{1}{v_c^2}\left(A_c I_c - \sum_{c'} U_{cc'} A_{c'} O_c\right) \tag{5.9}$$

where $U_{cc'}$ is the scattering matrix, on which the scattering cross section strongly depends.

Substituting this expression into the equation for the internal radial wavefunction at the boundary (*i.e.* matching the wavefunctions), we can rearrange for the scattering matrix in terms of the outgoing wave, the incoming wave and the R-matrix and present it in matrix form:

$$U = \rho^{\frac{1}{2}} O^{-1}(1 - RL)^{-1}(1 - RL^*) I \rho^{-\frac{1}{2}} \tag{5.10}$$

defining $L = \rho\frac{O'}{O} - b$ and $L^* = \rho\frac{I'}{I} - b$.

Defining the Coulomb and hard sphere phase shifts as $\Omega = \left(\frac{I}{O}\right)^{\frac{1}{2}}$ and given that

the penetrability comes from $P = \frac{\rho}{IO}$, the scattering matrix can be rewritten as

$$U_{cc'} = \Omega_c \Omega_{c'} \left(\delta_{cc'} + 2iP_c^{\frac{1}{2}} P_{c'}^{\frac{1}{2}} [(1 - RL)^{-1} R]_{cc'} \right). \tag{5.11}$$

Hence, the inelastic cross section comes from the sum over all channels with the appropriate angular coefficients:

$$\sigma_{\alpha\alpha'} = \frac{\pi}{k_\alpha^2} \sum_{Jsls'l'} \frac{2J+1}{(2I_1+1)(2I_2+1)} |U_{cc'}^J|^2. \tag{5.12}$$

For elastic scattering, an additional term must be included to account for Rutherford scattering.

Although the R-matrix notation has been used in the analyses presented in previous chapters, the simplest way to relate the formal R-matrix parameters to the observed experimental parameters (resonance energy and strength) is to define a new notation, known as the A-matrix:

$$\sum_{\lambda\mu} \gamma_{\lambda c} \gamma_{\mu c'} A_{\lambda\mu} = [(1 - RL)^{-1} R]_{cc'}. \tag{5.13}$$

The A-matrix notation allows systems with many channels but only a few levels to be considered more efficiently, a useful modification for the single resonance approximation used to transfer to the physical parameters.

Eliminating $(1 - RL)^{-1}$ from the right hand side of the equation and rearranging gives the definition of the A-matrix, by its inverse:

$$A_{\lambda\mu}^{-1} = (E_\lambda - E)\delta_{\lambda\mu} - \sum_c \gamma_{\lambda c} \gamma_{\mu c} (S_c - b_c) - \frac{i}{2} \sum_c \gamma_{\lambda c} \gamma_{\mu c} P_c. \tag{5.14}$$

Appropriately modifying the scattering matrix and, hence the cross section, while considering only inelastic scattering and a single resonance gives:

$$\sigma_{cc'} = \frac{\pi}{k_\alpha^2} g_J \frac{4P_c P_{c'} \gamma_{\lambda c}^2 \gamma_{\lambda c'}^2}{(E_\lambda - E - \sum_c \gamma_{\lambda c}^2 (S_c - b_c))^2 + \frac{1}{4}(\sum_c 2P_c \gamma_{\lambda c}^2)^2}. \tag{5.15}$$

Through the Thomas approximation [104], one can now define the physical widths

to be $\Gamma_{\lambda c} = \frac{2P_c\gamma_{\lambda c}^2}{1+\sum_c \gamma_{\lambda c}^2 \frac{dS(E_\lambda)}{dE}} = 2\gamma_\lambda^2 P_c$ and substituting these into the equation for the cross section then recovers the Breit Wigner form of the reaction cross section:

$$\sigma = \frac{\pi}{k_\alpha^2} g_J \frac{\Gamma_{\lambda c}\Gamma_{\lambda c'}}{(E_\lambda - E)^2 + \frac{1}{4}\Gamma_\lambda^2}. \tag{5.16}$$

As this calculation has made the approximation of a single narrow resonance, solutions obtained through this method are unlikely to be truly physical for resonances which vary greatly from this form. The calculation remains, however, a valid approximation which proves very powerful when making estimates of physical parameters from experimental excitation spectra. By varying the R-matrix parameters of E_λ and the many $\gamma_{\lambda c}$ the best fit cross section can be found and the parameters transferred back to their physical estimates.

The parameter transformations above follow the work of Carl R. Brune [105], who simplified the process. Previously a further transformation, such as the Barker transformation [106], was required to move between formal and observed parameters in addition to experimental and R-matrix parameters. This is discussed in detail in the description of the `AZURE` code [94].

5.3 Implementation of the Phenomenological R-Matrix

Given the importance of the R-matrix formalism to the field of nuclear astrophysics, not least for the extraction of resonance parameters and the extrapolation to experimentally challenging regions, it is important to compare the available codes to provide confidence in the results they provide. The R-Matrix calculations made in the earlier analysis of the ^{18}F(p,α)^{15}O reaction made use of a code written in Visual Basic, with Microsoft Excel as its framework, provided by Pierre Descouvemont and referred to as "`DREAM`".

A JINA collaboration, led by R.E. Azuma, have designed and implemented a code in the FORTRAN programming language, named `AZURE` [94]. This has been available for download from the JINA website for some time and has been used by many collaborations. In recent times, a new collaboration also within the JINA framework, have been working to upgrade this code to a new C++ implementation. I was tasked with the comparison of these three codes having

been invited to visit the University of Notre Dame in early 2012.

All three codes have a variety of options for the R-Matrix calculation: comparing the output to data (either through minimising to fit to the data or simply calculating the output from a set of input parameters), making a calculation from a set of input parameters within a defined energy region (useful for extrapolation purposes) and calculating either the cross section or s-factor. One additional option in the JINA codes is the ability to calculate the reaction rate from the input parameters.

The initial difference between the codes is in the input of the data. While `DREAM` requires all experimental data to be input in the centre of mass frame, `AZURE` requires it to be in the forward kinematics laboratory frame of reference. This includes experimentally calculated excitation functions.

In addition, while the `DREAM` code considers all Coulomb contributions up to the highest spin-parity group present regardless of any resonant contributions, `AZURE` does not. The user is therefore required to input so called dummy resonances of zero partial width for each unpopulated spin parity group so that the code will make a full calculation of the Coulomb and hard sphere contribution to the reaction.

The work on the ^{18}F(p,α)^{15}O reaction presented here and published by Mountford *et al.* [1] provides an ideal opportunity to do this. Making use of the data fitted, the parameters extracted and the calculations made in that work, three crucial aspects of the codes can be investigated.

5.3.1 Cross Section Calculation

In order to compare the three calculations, the recently published parameters of Mountford *et al.* [1] have been input to each of the three codes. Upon extraction of the differential cross section at $\theta_{c.m.} \sim 176^\circ$ it can be seen that the elastic scattering cross section is in very close agreement, as shown in Figure 5.3.

There is some disagreement around very narrow states of $J^\pi = {}^3/_2{}^+$ at $E_{c.m.} \sim 0.8$ and 1.1 MeV. The total width of these states is around 4 keV. This is likely due to the differentiation of the shift function, S in the `DREAM` code. The close agreement across all other resonances implies the use of the same Coulomb functions in each code, upon which the shift function depends.

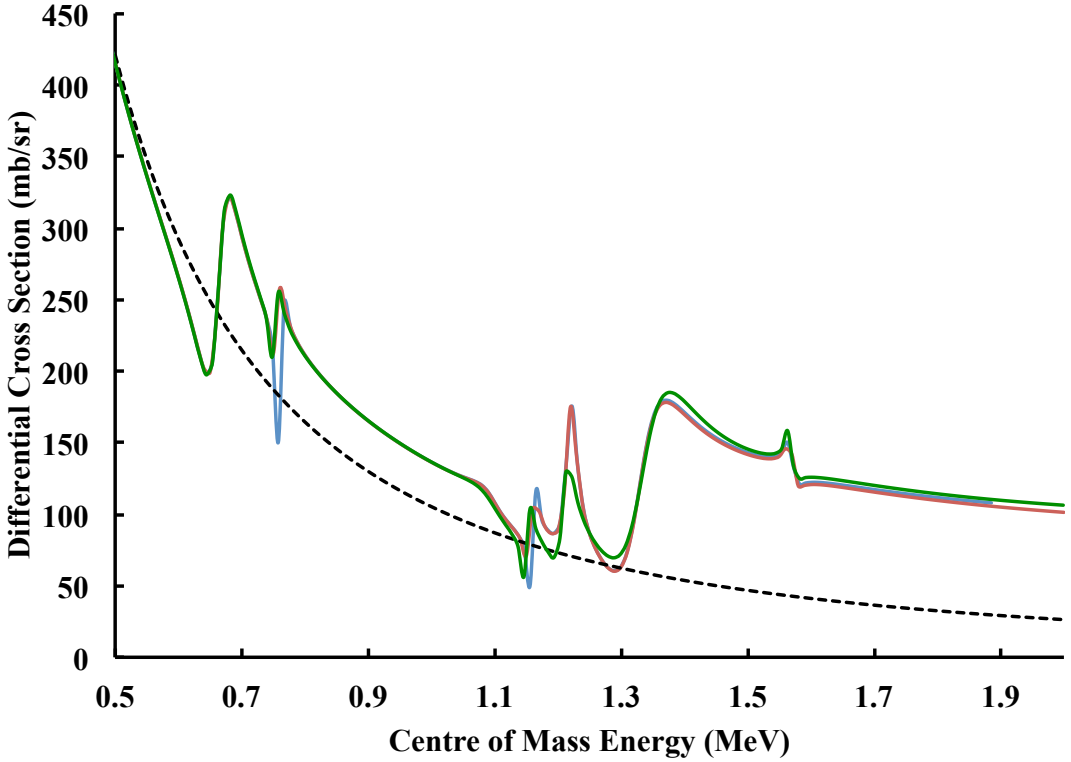

Figure 5.3 *Differential cross section of the $^{18}F(p,p)^{18}F$ reaction as calculated by the JINA C++ code (blue), the code of P. Descouvemont (red) and the original JINA FORTRAN code,* `AZURE` *(green). Note that the red and blue lines overlie each other perfectly at most energies and as such the JINA C++ calculation is obscured.*

In `DREAM`, however, the differentiation of this shift is calculated numerically as:

$$\frac{dS}{dE} = \frac{S(E_\lambda + \Delta E) - S(E_\lambda)}{\Delta E} \tag{5.17}$$

where ΔE is set to 0.001 MeV. For a resonance of partial width around 4 keV, or partial width around 2 keV, this could have the effect of smoothing the cross section and weakening the effect of the resonance. `AZURE` instead makes use of the LAPACK [107] package and the new C++ code makes use of GNU Scientific Libraries [108] to carry out differentiations. Thus, the JINA codes are likely to be more reliable in the calculation of experimental parameters.

While there is close agreement in the elastic channel, there is poor agreement in the differential cross section in the (p,α) channel, as can be seen in figure 5.4.

To find the source of this discrepancy, the cross section for each J^π group was plotted individually and compared, with identical cross section curves being

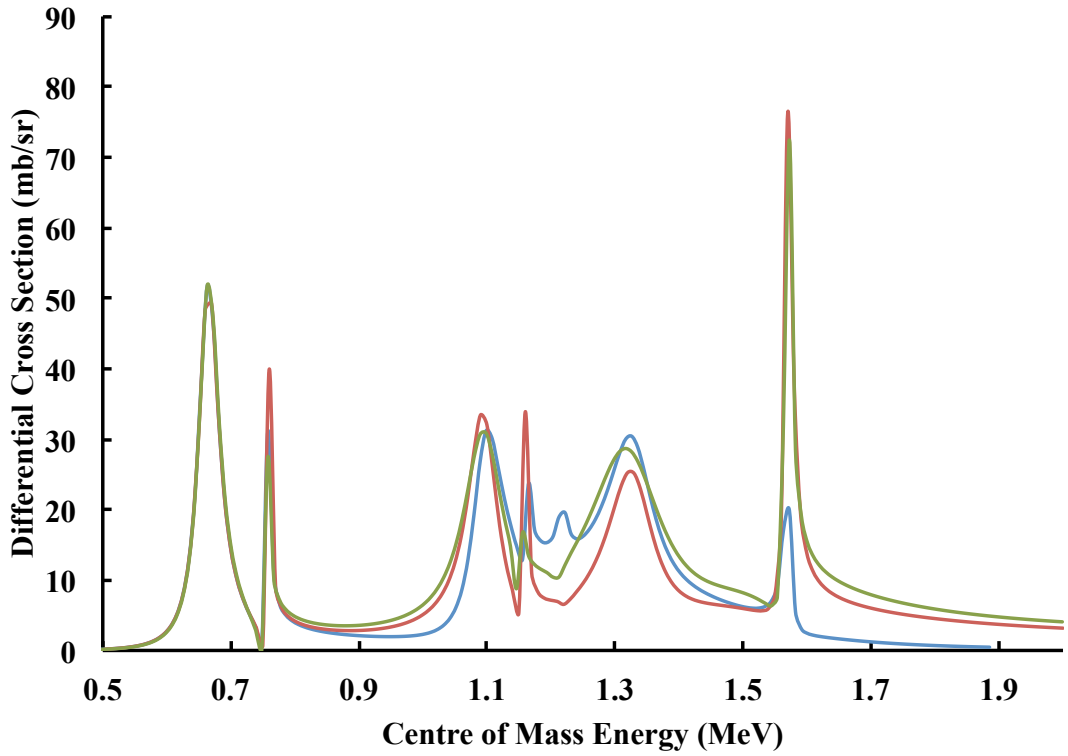

Figure 5.4 *Differential cross section of the* $^{18}F(p,\alpha)^{15}O$ *reaction as calculated by the JINA C++ code (blue), the code of P. Descouvemont (red) and the original JINA FORTRAN code,* `AZURE` *(green).*

produced for all groups, see figure 5.5. This implies that the calculations agree as far as the scattering matrix, since there is one scattering matrix for each J^π group. This was confirmed by comparing the total integrated cross section, which is shown to be consistent in figure 5.6, although `AZURE` produces additional strength in the region of $E_{c.m.}$ ~1.1-1.5 MeV with a consistent shape. The cause of this is under investigation.

The next step was to check each combination of two J^π partial waves, all of which agreed bar the combination of $^5/_2^+$ and $^1/_2^+$. This implied a discrepancy unique to this combination which was unlikely to be caused by the angular coupling coefficients being incorrectly calculated in either code. Furthermore, upon checking, the coupling constants, a combination of Racah and 6j coefficients, were found to be identical.

Figure 5.7 shows the differential cross-section as calculated from the $^1/_2^+$ and $^5/_2^+$ resonances in the Visual basic code and the new C++ code. For comparison, the contributions of each resonance group is included, added incoherently. Hence, it can be seen that the two codes appear to be applying alternative interference

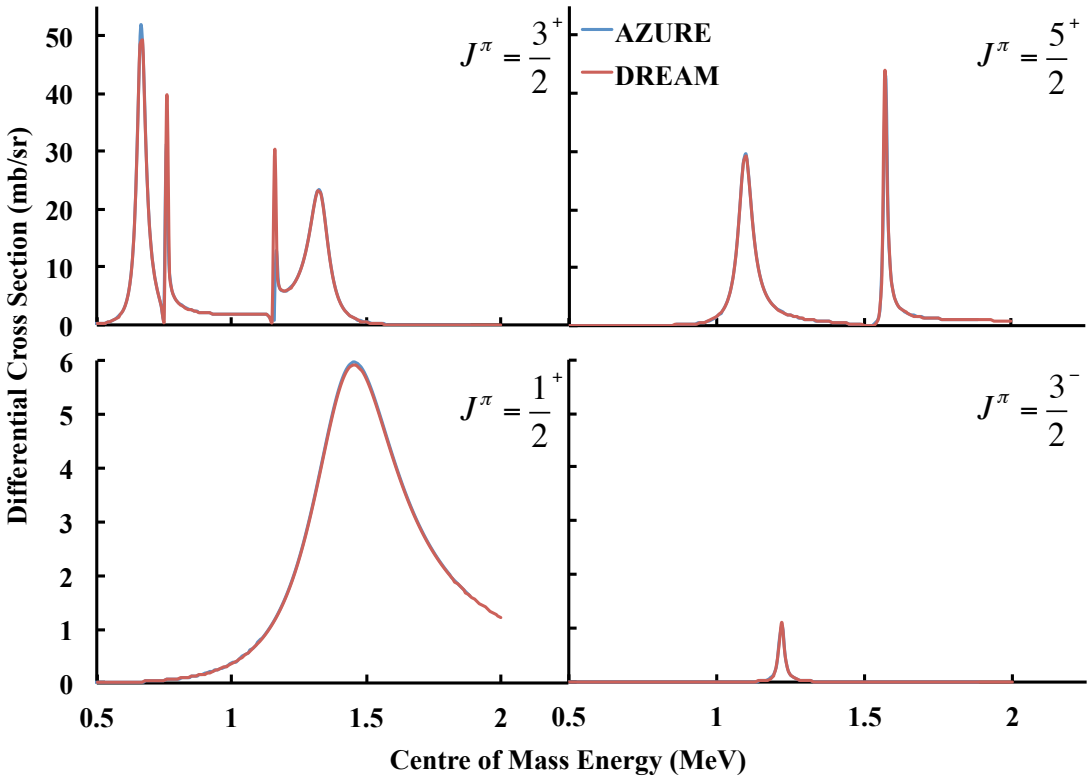

Figure 5.5 *Differential cross section of the $^{18}F(p,\alpha)^{15}O$ reaction as calculated by the JINA C++ code (blue) and the code of P. Descouvemont (red) for each spin-parity group in the calculation. The two lines overlie each other perfectly and so the C++ calculation is obscured.*

effects relative to the two partial waves.

Reversing the relative interference term of the broad $^1/_2{}^+$ resonance with respect to the $^5/_2{}^+$ pair appears to almost completely resolve the discrepancy between the calculations, as shown in figure 5.8 showing that the output cross sections remain consistent.

To find the source of this discrepancy, comparisons were made at each step in the calculation between the relative R-Matrices, scattering matrices and cross sections. It was eventually discovered that hard sphere scattering effects for non-elastic scattering were not included in `DREAM`, *i.e.* the non-diagonal elements of the scattering matrix.

`DREAM` calculates the cross section from the reaction phase shift, *i.e.* the shift of

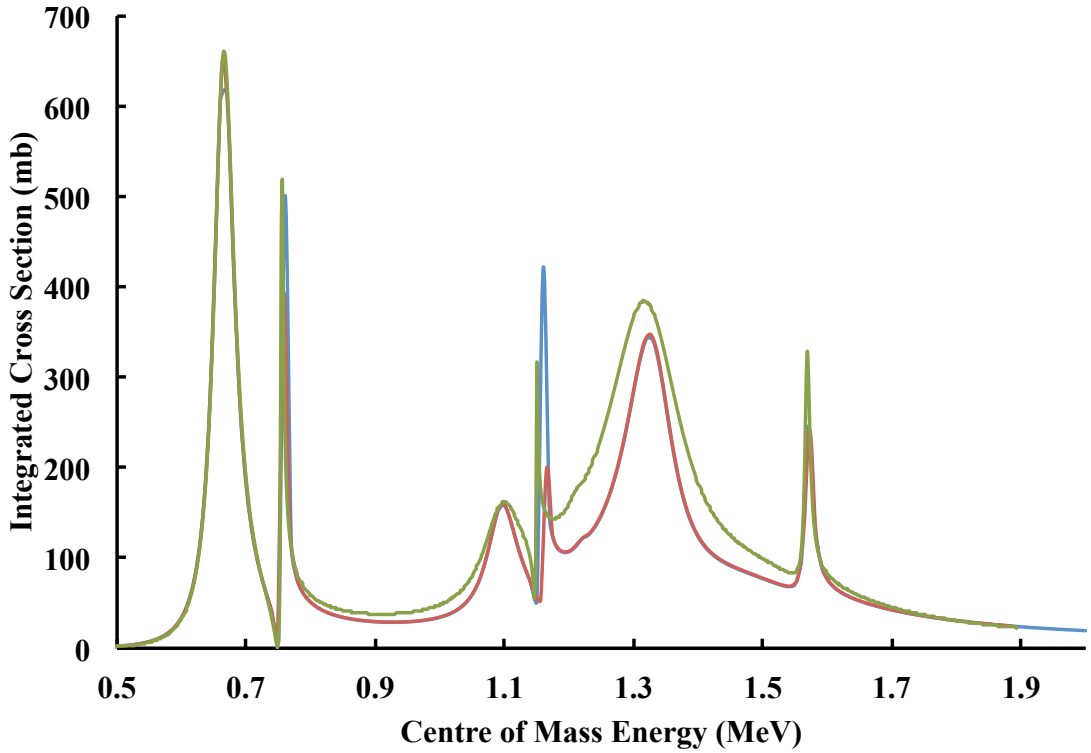

Figure 5.6 *Total integrated cross section of the $^{18}F(p,\alpha)^{15}O$ reaction as calculated by the JINA C++ code (blue), the code of P. Descouvemont (red) and the original JINA FORTRAN code,* `AZURE` *(green). Again the red and blue lines overlie each other perfectly at most energies and as such the JINA C++ calculation is obscured.*

the complex scattering matrix as in equation 5.18,

$$\delta = tan^{-1}\left(\frac{Im(U)}{Re(U)}\right). \tag{5.18}$$

The hard sphere phase shift should not have a significant effect on non-elastic scattering, however with the high width of the $^1/_2{}^+$ resonance it is possible that this has pushed the phase into the wrong domain of the $\tan^{-1}$ function, resulting in an opposite relative interference.

5.3.2 Data Fitting

The above study compared the output calculation from a given set of parameters. It is also important that the codes under investigation provide consistent results when presented with the same set of data. In order to test this, the data

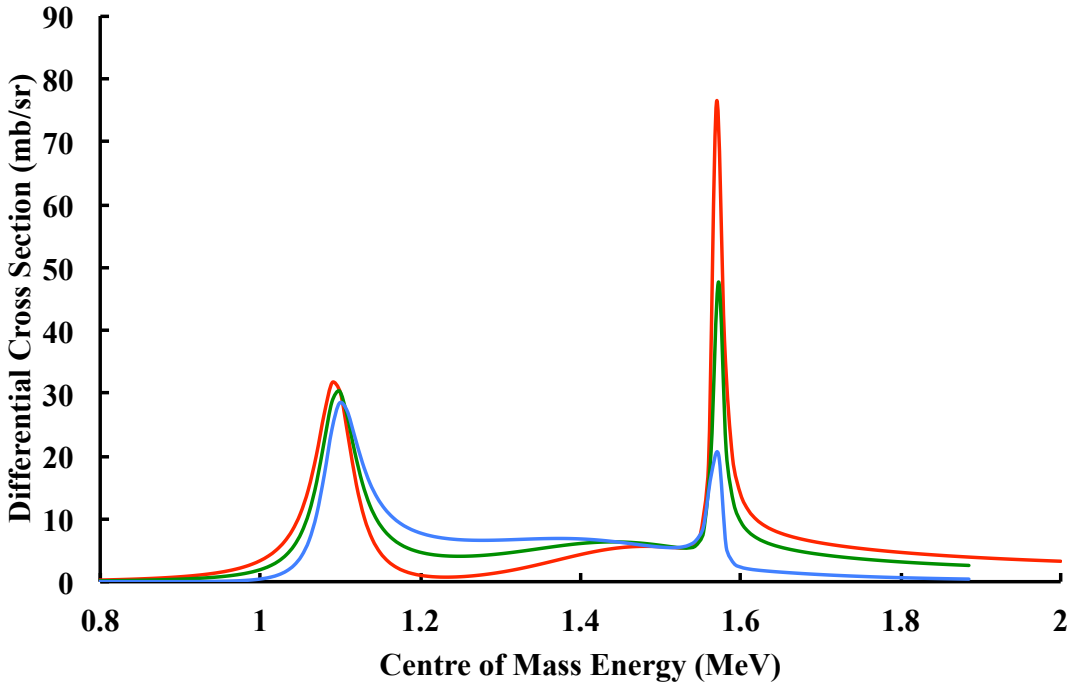

Figure 5.7 *Differential cross section for two partial waves of* $J^{\pi} = 1/2^{+} and 5/2^{+}$ *as produced by the JINA C++ code (blue), the code of P. Descouvemont (red) and the effect of incoherently adding the cross section associated with the individual partial waves (green).*

from Mountford *et al.* [1] were re-analysed within the *R*-matrix formalism as implemented by the two JINA codes.

With the statistical impact of the high energy data points reduced as in chapter 4, all parameters were set free to vary, with the broad $1/2^{+}$ state set to have an alternative relative interference to that extracted in the results of Mountford *et al.* [1].

As before, normalisation of the data is taken from the well-known 665 keV resonance in the ^{18}F(p,α)^{15}O reaction. This is possible within the C++ code's framework as the normalisation factor can be included as an unconstrained parameter. In order to make this new analysis consistent with that carried out in Mountford *et al.* [1], an iterative process was employed. The data were added to the C++ code and all parameters not associated with the 665 keV resonance or normalisation allowed to vary.

The data were then curtailed to only include points around $E_{c.m.}$ = 665 keV and all parameters constrained except the normalisation. This was repeated with the energy offset until two constant values were found. The parameter

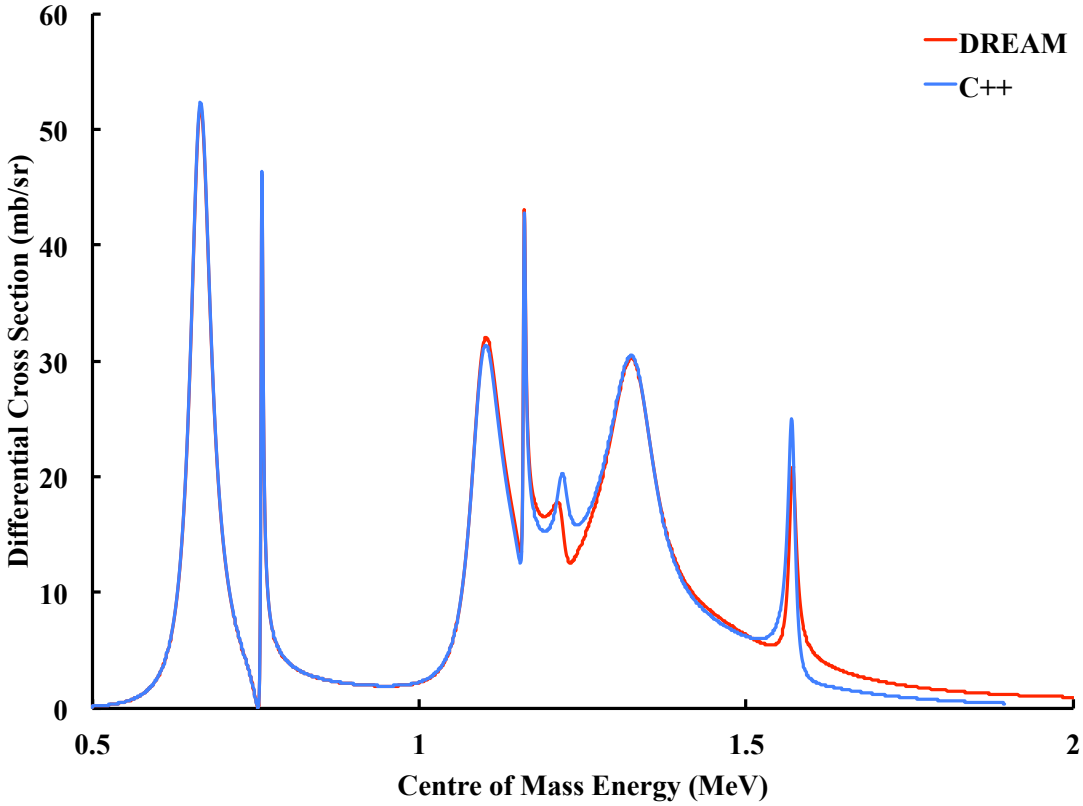

Figure 5.8 *Differential cross section of the $^{18}F(p,\alpha)^{15}O$ reaction as calculated by the JINA C++ code (blue) and the code of P. Descouvemont (red) when the relative interference between the $^1/_2{}^+$ and $^5/_2{}^+$ resonances is reversed.*

minimisation was then repeated and so on until the normalisation and offset remained unchanged for two consecutive fits.

It was found that a further normalisation of 0.994 and offset of -0.003 were required in the elastic data and a further normalisation of 1.031 and offset of -0.002 in the inelastic data relative to the final results of Mountford *et al.* [1].

The ability to vary normalisation is an improvement only available in the C++ version of the JINA codes. To demonstrate that the update is consistent with the original `AZURE` code, it was considered appropriate to perform a minimisation on the data as presented by Mountford *et al.* [1], given the negligible change in scaling factor, without any further normalisation.

Again, all parameters not associated with the 665 keV resonance were allowed to vary freely in the original `AZURE` code. The extracted parameters from both codes are reported in table 5.1 and the cross sections calculated as a result are

shown in figure 5.9

The minimisation process in each code, which led to these results, is similar with both codes minimising the χ^2 value to find a best fit. While the Visual Basic code has a procedure written into it, the JINA codes make use of CERN's MINUIT (FORTRAN) and MINUIT2 (C++) packages [95]. While the minimisation processes are similar, the error analysis is quite different in the Visual Basic code.

The error estimation of the Visual Basic code is discussed in chapter 4 and presented in [93]. The JINA codes, however, make use of the MINOS package included within MINUIT. This code performs a search of the parameter space for values of $\chi^2+\Delta\chi^2$ where $\Delta\chi^2$ defines the 1σ contour. In this example with 21 free parameters, three per resonance, $\Delta\chi^2 = 23.5$ (calculated per [93] and references therein), and as a result the errors are significantly larger from the JINA codes as a more thorough search of parameter space is performed.

In addition, should an error become very large in the latest version of MINOS used with the C++ code, it is assumed that the parameter is not well constrained by the data. As such one must consider the parameter assignment tentative and such parameters are denoted by a * in table 5.1.

Despite the difference between the processes employed by each code, most of the extracted parameters are within 1σ of each other and produce almost identical cross section curves. As such, it is shown that the three codes employ consistent data fitting techniques and analysis.

5.3.3 S-factor Calculation and Sub-threshold Resonances

The treatment of sub-threshold resonances within the R-matrix formalism is also of interest. As experimental partial widths are not defined for resonances which lie below a reaction threshold, the parameters must be dealt with in an alternative way. The code of Descouvemont requires sub-threshold resonances to be characterised by their reduced width amplitudes, γ, as defined in the R-Matrix formalism, while the JINA codes make use of asymptotic normalisation coefficients, ANCs, to do this.

To compare the effectiveness of each method, the calculation carried out by Mountford *et al.* [1] can be used. In that work, the effect of the existence of the

Table 5.1 *Tabulation of Results presented in Ref. [1], with the corresponding parameters extracted by the JINA FORTRAN (*`AZURE`*) and C++ (*`AZURE2`*) codes. J^π values are unchanged while a discrepancy arising in the relative interference between states is discussed in the text. An asterisk denotes a parameter which is not well constrained by the data and so no uncertainty could be extracted.*

Mountford *et al.* [1]				`AZURE` Results			C++ Results		
E_{CM} (MeV)	J^π	Γ_p (keV)	Γ_α (keV)	E_{CM} (MeV)	Γ_p (keV)	Γ_α (keV)	E_{CM} (MeV)	Γ_p (keV)	Γ_α (keV)
0.665	$\frac{3}{2}^+$	15.2	23.8	0.665	15.2	23.8	0.665	15.2	23.8
0.759(20)	$\frac{3}{2}^+$	1.6(5)	2.4(6)	0.755(77)	1.7(17)	3.3(33)	0.756(2)	1.7(17)	1.1(5)
1.096(11)	$\frac{5}{2}^+$	3(1)	54(12)	1.097(29)	3.3(20)	71(45)	$1.096(^{+42}_{-63})$	$3.4(^{+34}_{-29})$	$71(^{+71}_{-63})$
1.160(34)	$\frac{3}{2}^+$	2.3(6)	1.9(6)	1.149(14)	2.5(25)	2.1(21)	1.156*	4.5*	1.1(4)
1.219(22)	$\frac{3}{2}^-$	21(3)	0.1(1)	1.211(17)	27(17)	0.2(2)	1.210(5)	$20(^{+12}_{-2})$	0.1(1)
1.335(6)	$\frac{3}{2}^+$	65(8)	26(4)	1.339(23)	65(13)	31(27)	1.338(20)	59*	$30(^{+19}_{-23})$
1.455(38)	$\frac{1}{2}^+$	55(12)	347(92)	1.498(176)	44(23)	313(147)	$1.486(^{+55}_{-48})$	44(9)	304(66)
1.571(13)	$\frac{5}{2}^+$	1.7(4)	12(3)	1.569(30)	1.7(12)	8(6)	1.570(2)	1.8(18)	$6(^{+3}_{-6})$

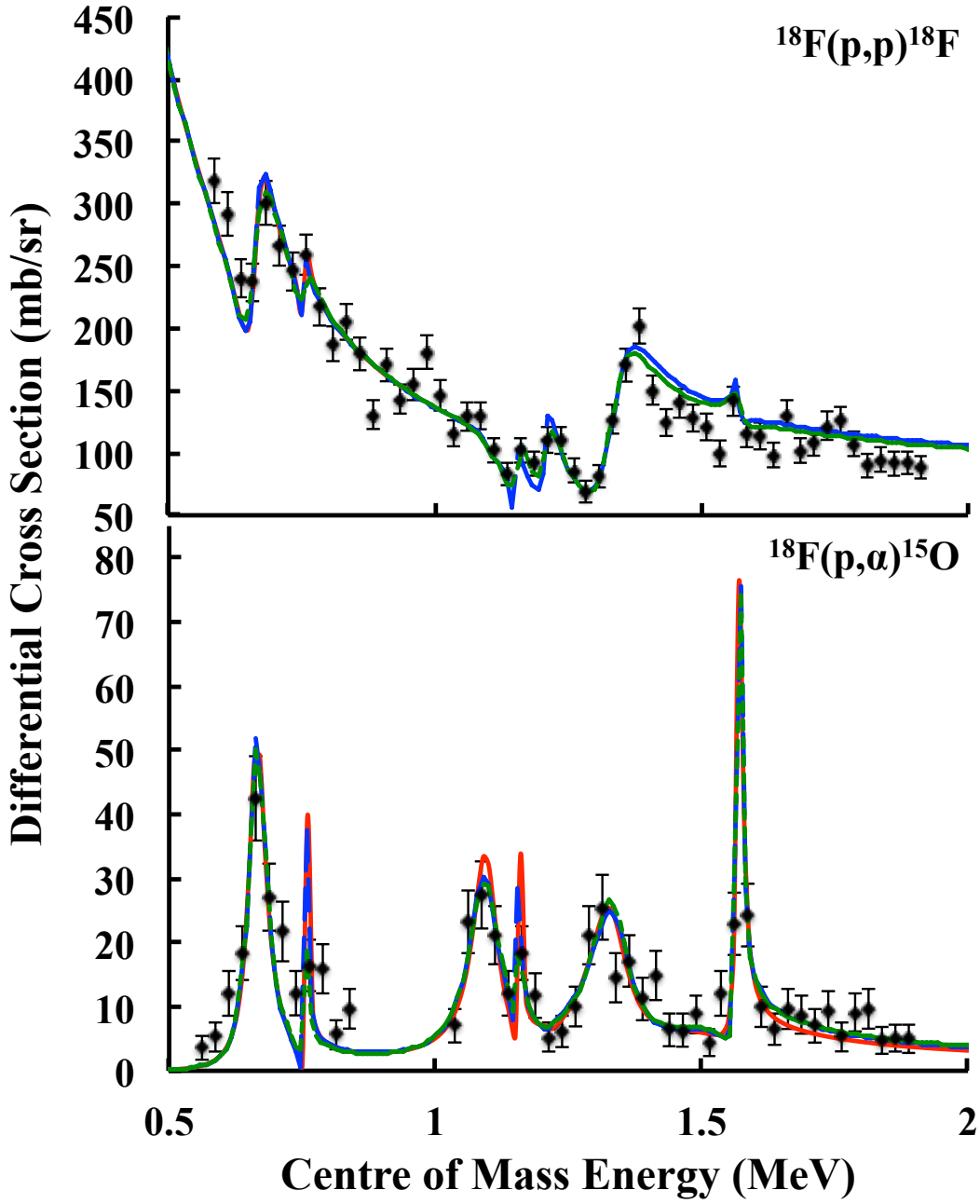

Figure 5.9 *The cross sections from the fit to the data of Mountford* et al. *($\bar{\chi}^2$ = 1.634) by the dual channel R-Matrix code of P. Descouvemont (red solid lines), the* `AZURE` *code ($\bar{\chi}^2$ = 1.435) of the JINA collaboration (blue long dashed lines) and the* `AZURE2` *code ($\bar{\chi}^2$ = 1.569) of the JINA collaboration (green short dashed lines)*

sub-threshold partner to the observed $^1/_2{}^+$ resonance is investigated by plotting the s-factor with and without its contribution.

To compare the codes, the s-factor is calculated for the parameters reported by Iliadis *et al.* [58] with the relative interference between the two resonances of interest aligned. In addition, we include the sub-threshold $^1/_2{}^+$ resonance reported by Adekola[66] with $\gamma_\alpha^2 = 0.306$ MeV and ANC = 73 fm$^{-1/2}$.

The resulting s-factor from each of the three codes can be seen in figure 5.10. The code of Descouvemont and the C++ JINA code are in excellent agreement throughout the Gamow window of interest for nuclear astrophysics, however the better resolution available from the JINA code is again clear as the narrow feature at 25 keV is only visible here.

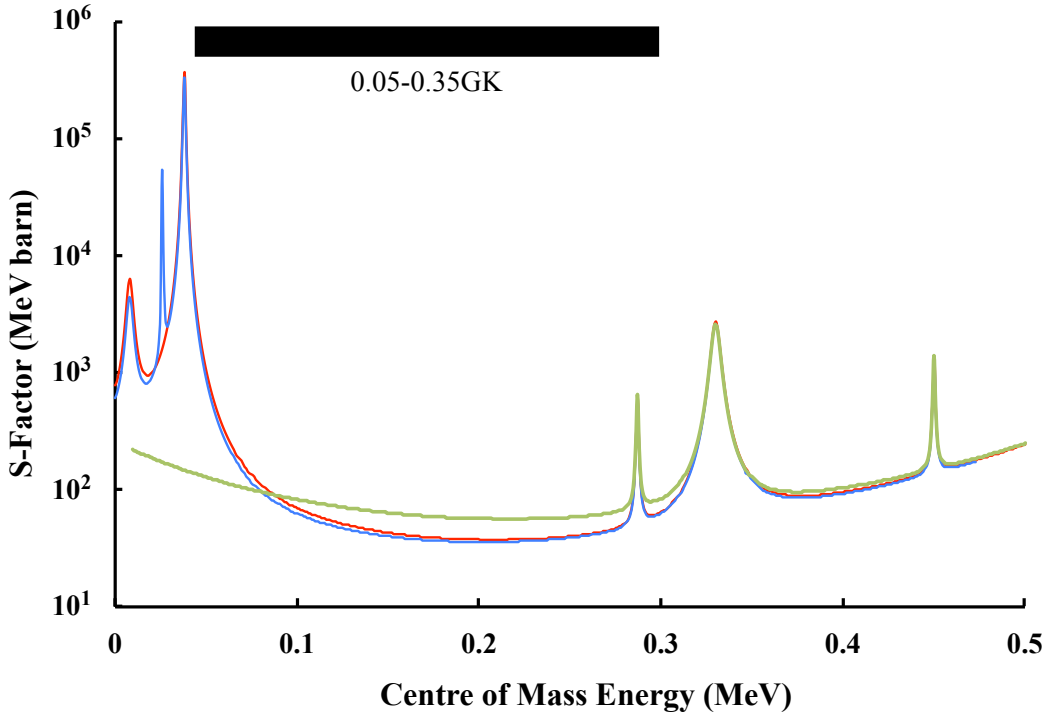

Figure 5.10 *Astrophysical s-factor of the* $^{18}F(p,\alpha)^{15}O$ *reaction based on the parameters of Iliadis* et al. *[58] as calculated by* `DREAM` *(red line),* `AZURE` *(green line) and the JINA C++ code (blue line)*

At this point, `AZURE` becomes more troublesome. Due to the narrow widths of the states at very low energy, `AZURE` is unable to process them and so they have not been included in the calculation. All other resonances are included in the calculation and it can be seen that the broad shape of the curve is consistent. Since the low energy resonances have been removed, however, the

lack of interference has resulted in a significantly higher s-factor through the Gamow window. At low energy there is also a known issue with this code that the shift functions used to transfer from experimental parameters to R-matrix parameters are not reliable. While this transformation may encounter difficulties, the calculation of the cross section from R-matrix techniques is likely to be consistent. This difficulty, however, in transforming from R-matrix parameters to experimental parameters, and vice versa, inevitably results in some accuracy being lost at this level by the calculation, and the deviation of this code from the others is clear. This known issue with the shift functions has been resolved in the updated C++ code, however, as shown by the agreement between this and the Visual Basic code. This is also a possible explanation for the additional strength observed in figure 5.6.

In summary, by comparing the cross-sections from the results of Mountford *et al.* [1], and then repeating the fitting procedure and extracting resonance parameters, three codes implementing the important R-matrix formalism have been compared. The resulting calculations, fits and extracted parameters are shown to be consistent and a minor discrepancy has been addressed. There remains a minor discrepancy between the original `AZURE` code and the `DREAM` and C++ codes which is as yet not fully understood, where additional strength is observed in the cross section shown in figure 5.6.

As a result of this work, the study carried out in [1] and many previous studies which make use of these codes are validated and any future work requiring the R-matrix formalism may be carried out with confidence.

Chapter 6

The role of ^{26m}Al(p,γ)^{27}Si in explosive astrophysics

6.1 Motivation

The destruction of ^{26}Al is of particular interest due to the existence of a metastable $J^{\pi}=0^{+}$ state, in addition to the $J^{\pi}=5^{+}$ ground state, on which radiative capture is also possible. There have been several studies of the ^{27}Si states relevant to the ^{26}Al(p,γ)^{27}Si reaction (see [109, 110] and references therein), culminating in extensive studies by Deibel *et al.* [111], Lotay *et al.* [112–114] and Parikh *et al.* [115] from 2009 to 2011.

Lotay *et al.* indirectly populated the ^{27}Si, nucleus through the ^{12}C(^{16}O,n)^{27}Si fusion reaction, which then emitted γ-rays to be observed by the Gammasphere array [116]. This study was able to determine new spin and parity data for excited states in ^{27}Si across the largest energy range of these three studies, and was able to identify two states likely to make significant contributions to the ^{26g}Al(p,γ)^{27}Si reaction rate; an ℓ_p=0 transition at E_r=127 keV (E_x=7590 keV) and an ℓ_p=2 transition at E_r=68 keV (E_x=7531). The same team then carried out the neutron transfer study of the mirror ^{27}Al nucleus, ^{26}Al(d,p)^{27}Al, with the TUDA scattering chamber [88] at TRIUMF in June 2012 in an attempt to constrain the spectroscopic factors of these states. The analysis of these data is ongoing [117].

Before 2009, all studies had focussed on the ground state reaction and it was

the work of Deibel *et al.* [111] that first included the isomeric destruction as a primary project goal. Excited states in ^{27}Si were populated through two transfer mechanisms; ^{27}Al(^{3}He,t)^{27}Si and ^{28}Si(^{3}He,α)^{27}Si at Yale University. Resonances were populated up to E_x=9856 keV (E_r^m=2165 keV). Most interestingly, a resonance at E_r^m=445(4) keV (E_x=8136(4) keV) was observed with ℓ_p^m=0, appearing to be a prime candidate for radiative capture on the isomeric state in ^{26}Al.

The Gammasphere study discussed above [112] better constrained the parameters of a $^3/_2^-$ state at E_x=8070 keV, previously reported by Endt *et al.* [118], and the state observed by Deibel *et al.*, now at E_r^m=447.7(6) keV (E_x=8139.0(6) keV). This latter resonance was found to have J=$^1/_2$ by Lotay *et al.*, consistent with the ℓ_p^m=0 assignment by Deibel *et al.* Parikh *et al.* [115] populated the ^{27}Si nucleus through the neutron stripping reaction, ^{28}Si(^{3}He,α)^{27}Si, up to around 600 keV above the proton threshold. The three resonances discussed above, which lie below the experimental threshold in [115], were found to be consistently described in both studies.

In the ^{26m}Al + p system, population of the resonances at E_r^m=378 (E_x=8070 keV) and 448 keV (E_x=8139 keV) requires ℓ_p^m=1 and ℓ_p^m=0,1 transitions, respectively. In the ground state system, the angular momentum transfers required to populate these states are ℓ_p=3 and 4,5, hence, these resonances are expected to dominate the rate of the ^{26m}Al(p,γ)^{27}Si reaction at most astrophysical temperatures. At very low temperatures, such as those found in Wolf-Rayet and AGB stars and CO-novae, a further resonance is likely to contribute significantly at E_r^m=146.3 keV, however this is too low in energy for direct measurement.

At the temperatures found in ONe-novae and core-collapse supernovae, 0.2-1 GK, the rate is most likely to be dominated by the 378 keV resonance. The strength of this resonance, however, remains highly uncertain and, therefore, it is not possible to rule out a significant or even dominant contribution from the 448 keV resonance.

An experiment was, therefore, proposed to run on the DRAGON recoil separator which would directly determine the radiative capture strength of these resonances and further constrain the reaction rate for the isomeric reaction. The isomeric destruction of ^{26}Al could make a significant contribution to the overall destruction of the nucleus in stellar nucleosynthesis. As such, this direct measurement will aid the understanding of ^{26}Al content in the solar system.

6.2 Direct Measurement of the ^{26m}Al(p,γ)^{27}Si Reaction

Relatively recent advances in the development of radioactive ion beams have allowed a direct measurement to be made on the ^{26g}Al(p,γ)^{27}Si reaction at TRIUMF in 2006 [110]. The experiment described here, however, was the first resonant capture reaction with an isomeric beam, carried out to perform the first direct measurement of the ^{26m}Al(p,γ)^{27}Si reaction, again at TRIUMF. A 500 MeV proton beam, from the TRIUMF cyclotron, was impinged on a high-purity silicon carbide target [119]. The radioactive ^{26}Al, produced by spallation reactions in the target, was then electrostatically extracted and separated using a mass spectrometer. The beam is then accelerated in two stages, first through a radio-frequency quadrupole accelerator and then a drift-tube linear accelerator [120]. The beam of ^{26}Al ions was delivered to the DRAGON recoil spectrometer where it was impinged upon a windowless target of hydrogen gas.

Table 6.1 *Beam energy and target pressure combinations for the $^{26m}Al(p,\gamma)^{27}Si$ study with the resulting central energy of the beam profile through the gas target.*

Set	Beam Energy (keV/u)	Target Pressure (T)	$E_{c.m.}$ Range (keV)	$E_{c.m.}$ (at target centre) (keV)
1	390	7	360-379	369
2	455.75	7	423-442	433
3	458.5	5	432-445	438
4	459.5	5	432-446	439
5	469.4	5	442-456	449
6	469.4	7	437-456	446
7	469.35	5	442-456	449
8	484.19	4	459-470	465

The beam energy and target pressure were selected to fully envelop the resonance of interest in each case, attempting to place the expected resonance energy at the centre of the target. Table 6.1 gives all energy and pressure combinations used and the resulting central energy, each referred to as a 'set'. Figure 6.1 shows the energy regions covered relative to both the ground and isomeric states in each case. Given that the ions in the beam are formed in both ground and isomeric configurations, two separate energy regions are probed by the beam.

The first of these runs was designed for normalisation and background monitoring purposes, utilising the ground state ℓ_p=1 resonance at E_r ~369 keV

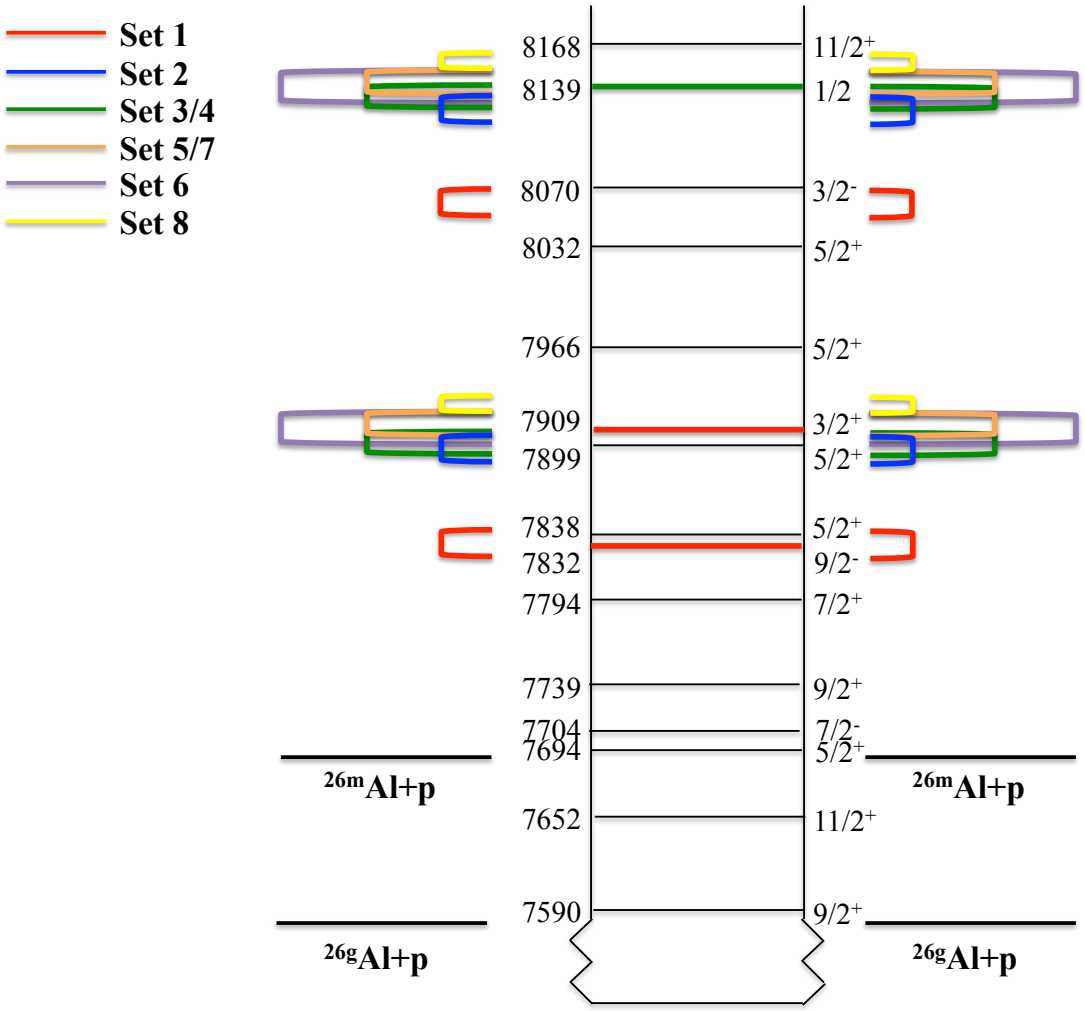

Figure 6.1 *Known levels in ^{26}Al above the ^{26}Al+p threshold. The ground state resonances of interest are shown in red and the isomeric resonance is shown in green. the excitation energy regions probed by each beam energy and target pressure set are shown.*

(E_x=7832 keV). From then on measurements were taken on or around the ℓ_p^m=0,1 isomeric resonance at 448 keV. This resonance was chosen due to the low angular momentum transfer found by both Lotay *et al.* [112] and Deibel *et al.* [111], implying a significant and measurable resonance strength. The chosen energy and target pressure combinations are sufficient to study on this resonance (sets 5 and 6) and estimate possible contributions from two ground state resonances, at ∼446 keV (ℓ_p=4) and ∼436 keV (ℓ_p=2) [112], in sets 3 and 4. Set 6 is likely to have contributions from both isomeric and ground state resonances for completeness. Finally, off-resonance data were taken at sufficiently high energy in set 8.

6.2.1 DRAGON

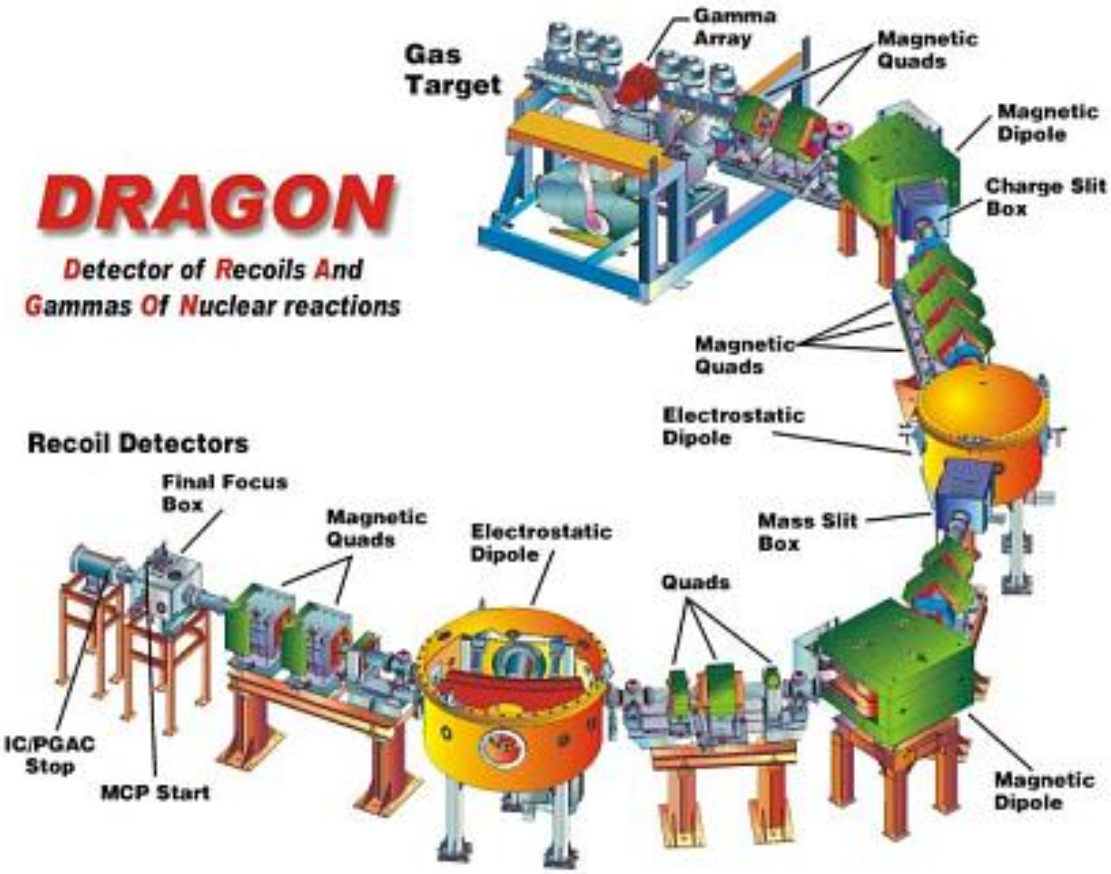

Figure 6.2 *The DRAGON Recoil Separator at TRIUMF.*

The Detector of Recoils and Gammas of Nuclear Reactions, or DRAGON [121], is a recoil spectrometer sited at the TRIUMF laboratory, Vancouver, Canada. It consists of two electrostatic dipoles and two magnetic dipoles for ion-selection with a facility for the final recoil to be detected in either an ionisation chamber or

silicon strip detector. In this experiment an ionisation chamber was used, filled with isobutane gas at a pressure of 13 Torr.

The target chamber consists of a gas cell that was filled with hydrogen gas, and which has two surface barrier detectors, at 30° and 57° to the beam axis for detection of elastically scattered protons for beam normalisation, see figure 6.3.

The gas target is surrounded by 30 BGO detectors for prompt γ-ray detection which are used in coincidence with recoil measurements for event identification. Recoiling ions then continue down the DRAGON beamline and first encounter a magnetic dipole for charge state separation, immediately followed by a set of charge slits where unwanted recoils are dumped. The radiative capture recoil beam is then refocussed through magnetic quadrupoles before mass-selection was performed with an electrostatic dipole. This process is repeated once more prior to final detection. Immediately before the ionisation chamber is an MCP to allow for relative time of flight measurements for additional event identification.

6.2.2 Beam Diagnostics

As the beam consisted of ^{26}Al ions in both the ground and metastable states, it was important to measure the intensity of isomeric ions separately from the total beam intensity.

The intensity of the isomer, ^{26m}Al, was obtained from observations of 511 keV gamma rays due to the β^+ decay of the isomeric state. The beam is deposited in the left slit after the first magnetic dipole component of the DRAGON separator, downstream from the target. The ions in the isomeric state decay by the emission of a positron which is guided up a "horn" to the centre of two sodium iodide detectors. The gamma rays produced by the annihilation of these positrons are then detected by the sodium iodide detectors, as shown in figure 6.4.

A `GEANT4` simulation has been carried out by Charles Akers (University of York) to estimate the combined effect of detector efficiency and acceptance giving a final efficiency for the number of gamma ray coincidences per ion.

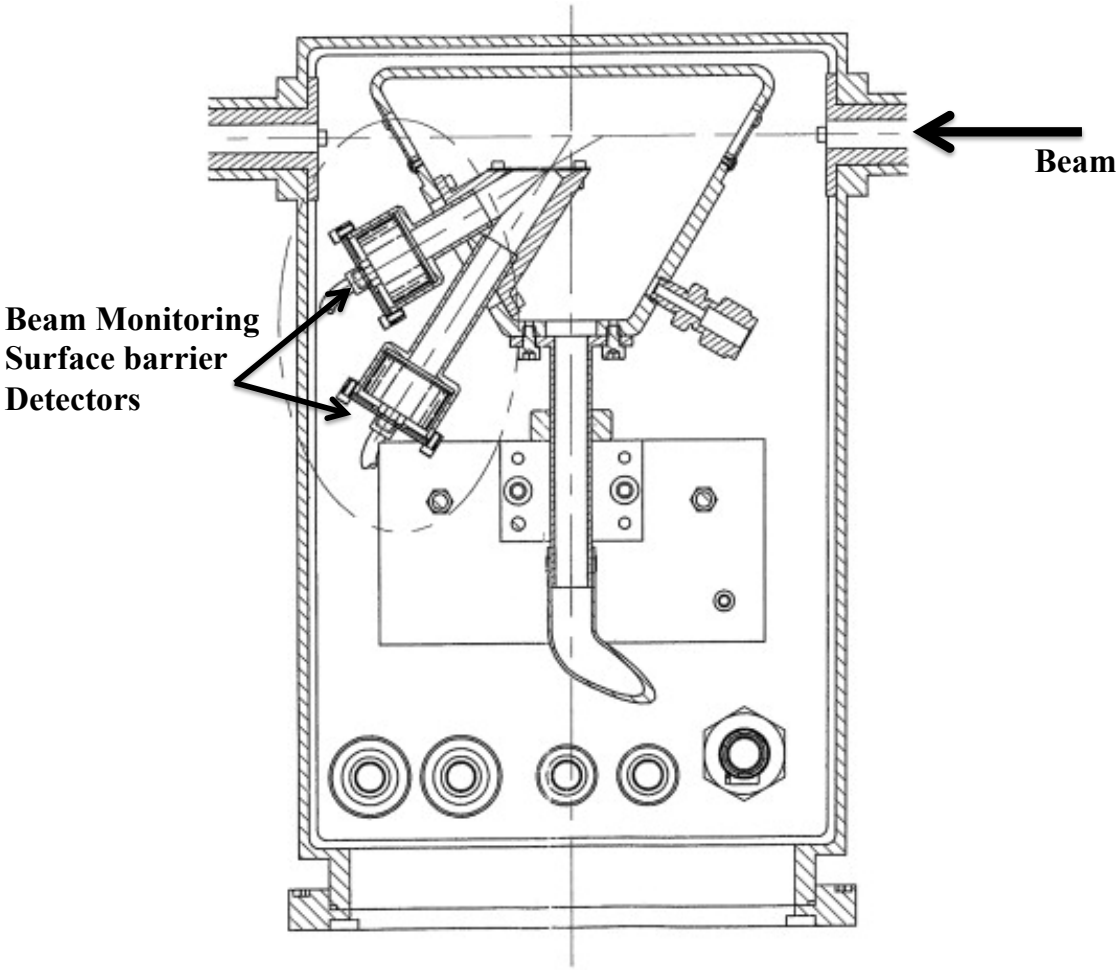

Figure 6.3 *The target chamber of the DRAGON recoil separator. The chamber is filled with a sufficient volume of target gas, hydrogen in this case. The surface barrier detectors for beam normalisation and monitoring are shown. The array of 30 BGO detectors is not shown but would be closely packed and stacked around the target [122], covering a solid angle of ∼90% of 4π [123].*

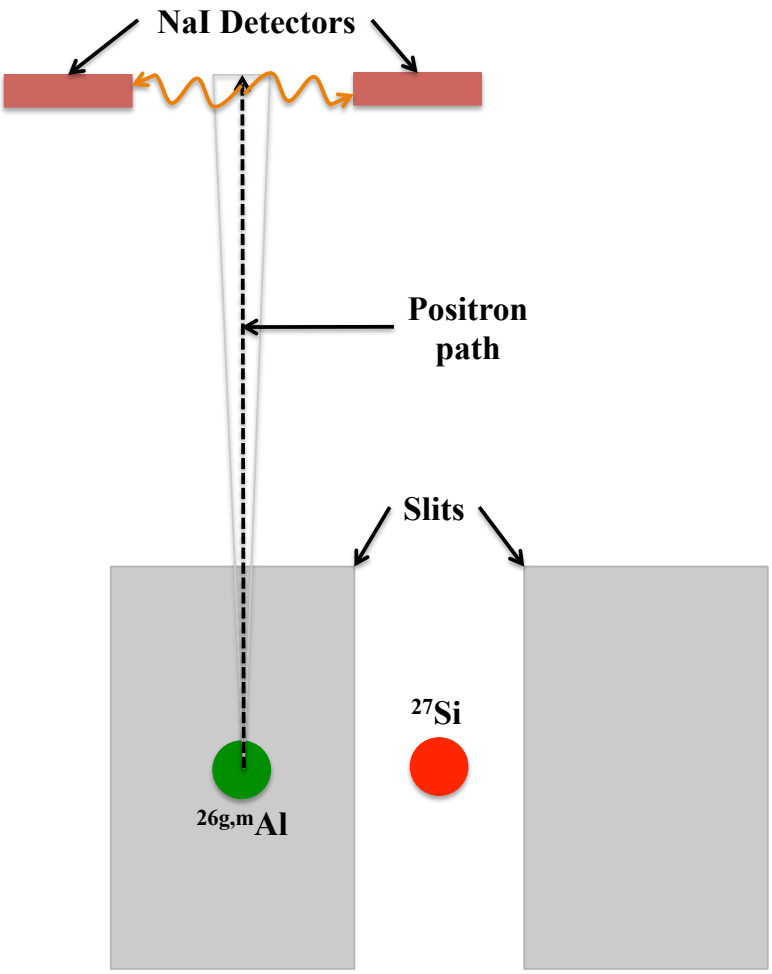

Figure 6.4 *Schematic of the arrangement for counting decays from the isomeric component of a beam of ^{26}Al.*

6.3 Normalisation Calculations

Integrated Beam Intensity

In DRAGON, the total beam intensity is measured and monitored through a process based on Rutherford Scattering of protons in the hydrogen gas target. As shown in figure 6.3, there are surface barrier detectors at 30° and 57° to the beam line to monitor these elastically scattered protons. Hence, the total integrated Rutherford Scattering proton yield can be related to the integrated beam intensity on the experimental target. This is described in the thesis of Shawn Bishop [124].

This relation is known as the R-value and is defined as:

$$R = \frac{I}{qe}\frac{\Delta t}{N}\frac{P}{E_{beam}^2}\epsilon. \tag{6.1}$$

In equation 6.1, I is the beam current reading taken upstream of the target before each run. This is recorded automatically in the DRAGON system by the `Rossum` program, which at the end of the run inserts Faraday Cup 4 (FC4), upstream of the gas target, to measure the beam intensity over time. `Rossum` then analyses the produced curve, omitting any slopes or spikes due to the cup bias response, and provides the average beam current during this reading. This cup is then removed and the Charge Slits Faraday Cup (FCCH) is inserted and `Rossum` repeats the analysis for this measurement. The measurement on FC4 is then repeated before the final Faraday cup (FCF), located prior to the ionisation chamber, is inserted and the average current extracted. FC4 is inserted one more time for a third reading of the beam current and then, once this is removed, the next experimental run is started. The process is shown schematically in figure 6.5.

During the `Rossum` analysis, occasionally the beam will drop during the cup reading (due to momentary loss of primary proton beam, etc), so each reading was inspected by eye and any discrepancies, less than 5% of runs, were omitted. The accepted value for I must be taken as the average of the remaining readings. The `Rossum` programme also provides a reading for each Faraday cup downstream of the DRAGON target, after the first magnetic dipole and after the first electric dipole, allowing a monitor of beam transmission through the DRAGON separator.

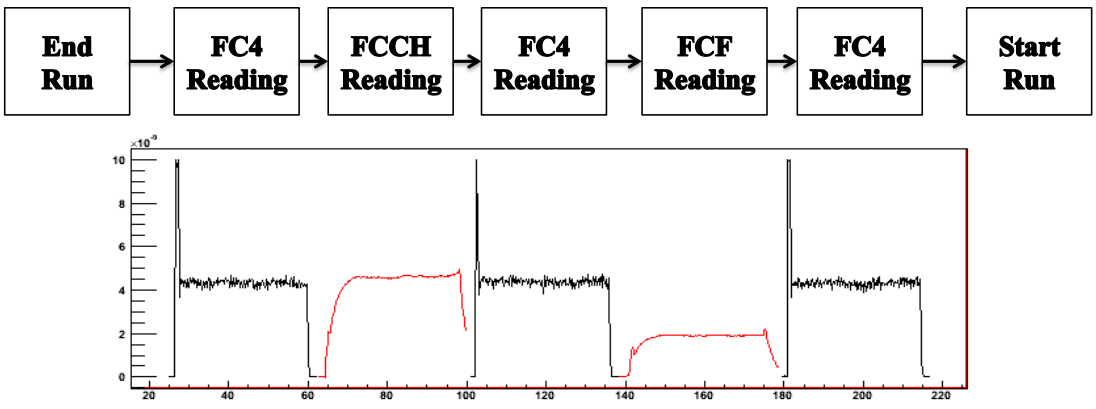

Figure 6.5 *The process of the* `Rossum` *program at TRIUMF which automatically ends runs and takes faraday cup readings to monitor beam intensity. An example of the readout is given below each step.*

The flux of beam ions on the Faraday cup is given by the current divided by the

charge state, q, and the electric charge, e, forming the first part of the R-value calculation. The charge state selected for each run was chosen based upon the charge state distribution for the ^{26}Al beam. The early runs in set 1, aimed at the ground state resonance, used a charge state of six while the remaining runs used a charge state of seven.

The relationship to the number of protons detected is initialised first through the scaler counts in the surface barrier detectors at the start of each run. N is the number of scaler counts for the specified surface barrier detectors in time Δt. For the purposes of normalisation, a time interval of 200 seconds was chosen.

Target pressure, P, in Torr and beam energy, E_{beam}, in keV/u were automatically recorded in the run log for each experimental run while transmission, ϵ, was calculated at each energy change, with no gas in the target, and recorded in the run log. The transmission can then be monitored throughout the run from each `Rossum` reading with the target filled. This allows any significant changes in the transmission to be identified and investigated further, although no such effects were observed here.

Once R-values have been obtained for each run in the experiment, they are studied for outliers and any runs with abnormalities in the R-value calculation are omitted. Such abnormalities can include the Faraday cup readings being unstable or a dropout of events in the surface barrier scalers.

For each set of energy and target pressure, the average R-value is then calculated with its standard error, as shown in figure 6.6. Calculating these R-values based on "good" runs gives an average value of, effectively, beam ions per scattered proton. Hence, the equation can be reversed to calculate the integrated number of ions incident on the target with the scaler number replaced by the total number of elastically scattered protons (N_{peak}) over the whole run, as shown in equation 6.2.

$$N_{Al} = R\frac{E_{beam}^2}{P}N_{peak} \tag{6.2}$$

An example of the elastic scattering peak is shown in figure 6.7 for the 469.4 keV/u runs at a target pressure of 7 Torr. The elastic scattering events are counted up and scaled for live time based on the triggers presented and accepted to find the total N_{peak} for the runs.

The final values for total beam intensity are given in table 6.2.

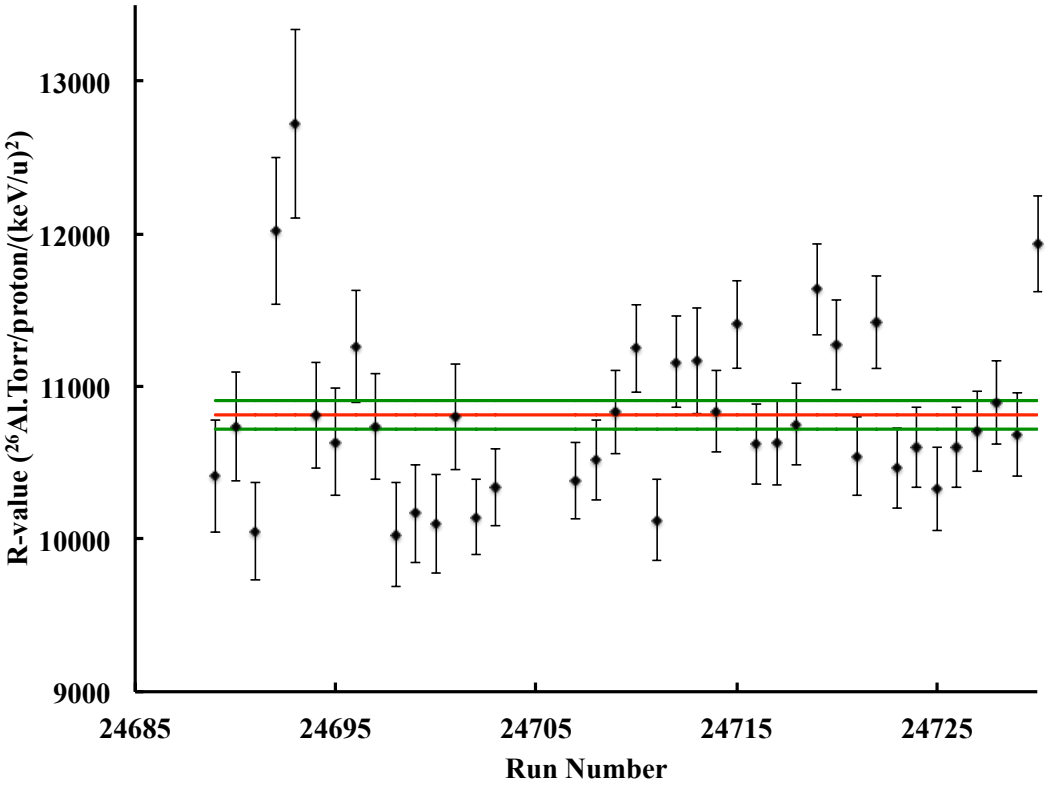

Figure 6.6 *R-values the 469.4 keV/u runs at 5 Torr target pressure. Red line denotes the mean R-value and the green lines show the error on the mean.*

Since the R-value is taken as an average, and the calculated R-values show no significant time dependance, the standard error on the mean may be used for the uncertainty in its value. Combining this, in quadrature, with the uncertainty in the elastic scattering peak gives the error on the number of incident aluminium ions. The beam energy has uncertainty of less than 1 keV/u and the uncertainty in the target pressure is less than 0.01 Torr, both less than 0.3 %, and so these may be considered negligible.

Isomeric Beam

As discussed previously, the isomeric component of the aluminium beam can be identified by its associated β^+ decay to the ^{26}Mg ground state. To count the number of 511 keV gamma rays in the sodium iodide detectors, the spectra were plotted against each other and a gate placed around the 511 keV locus, as shown in figure 6.8. This locus was then integrated and this number divided by the live time, as calculated earlier, to provide the true number of gamma rays produced

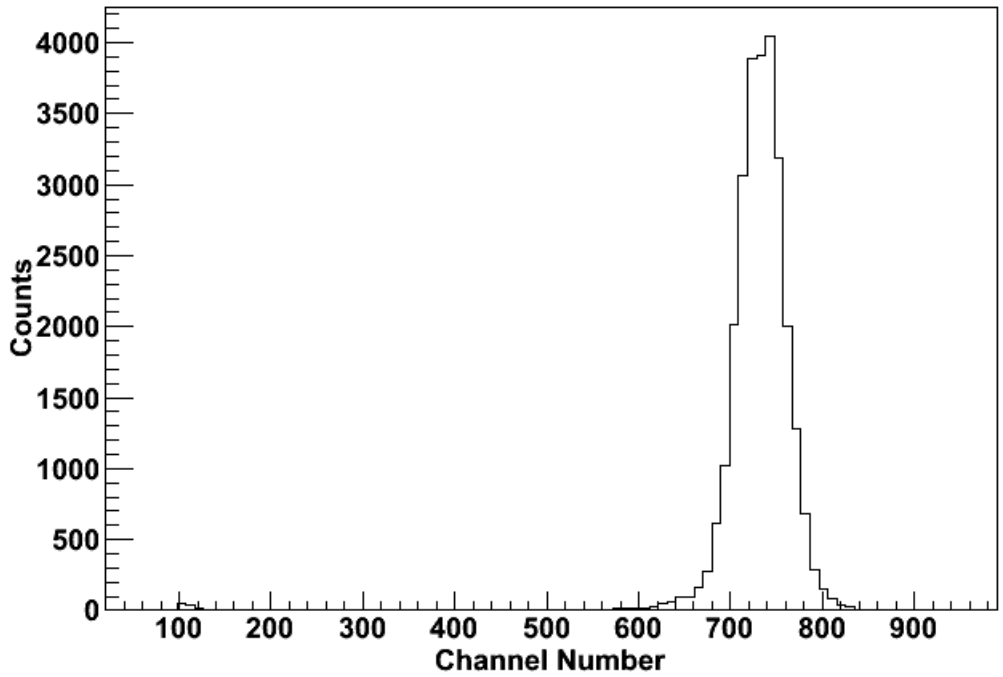

Figure 6.7 *Events due to elastically scattered protons from the DRAGON target at 30° to the beam axis.*

from isomeric ions. This number is divided by the efficiency to give the isomeric beam intensity. The final numbers are given in table 6.2.

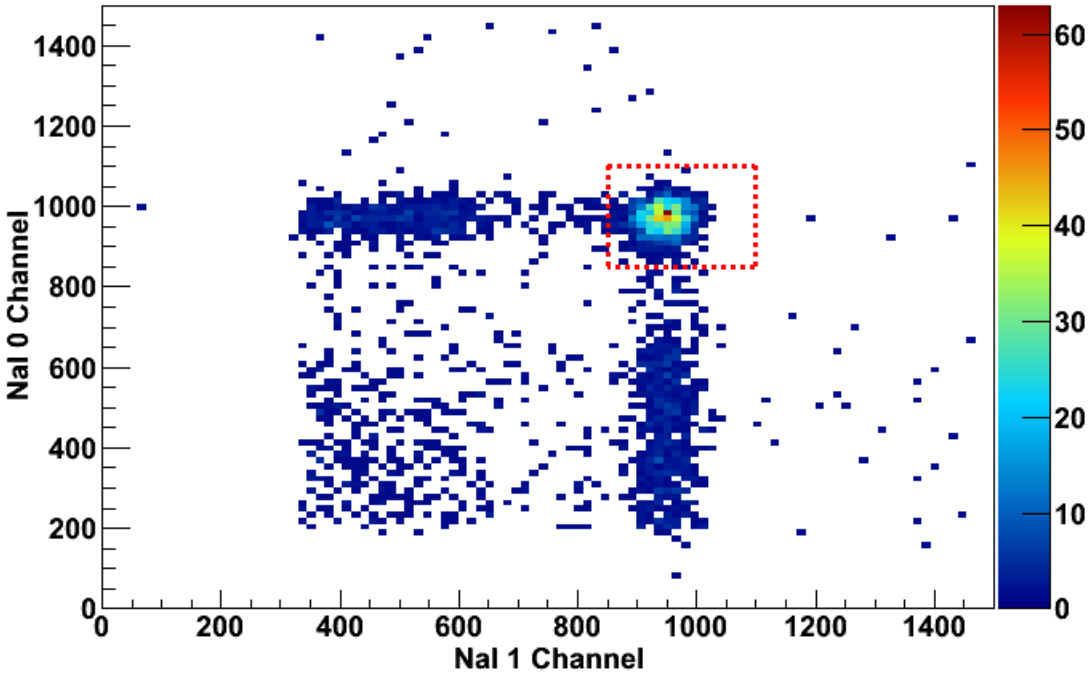

Figure 6.8 *The coincidence spectrum for NaI counts in run 24710. The dashed red line shows the gate used for counting 511 keV gamma events.*

The error on the number of counts in the sodium iodide detectors is again found from Poisson statistics. This is combined with the error on the live time to give an uncertainty on the true sodium iodide 511 keV peak counts. This is then combined, as above, with the error on the efficiency as given from the NaI GEANT4 simulations to give an uncertainty on the number of ^{26m}Al projectiles impinging the target.

As DRAGON is tuned to allow recoiling ions of a specific charge state to continue through to the final detector system, only isomeric ions in this charge state will arrive at the left mass slit. To find the charge state fraction, the calculated charge state distribution for a beam of 469.4 keV/u was scaled to the measured charge state distribution at this energy, as shown in figure 6.9. The scaling factor was calculated for each charge state and then applied to the calculation for all remaining energy groups. The charge state fraction for the selected charge state was then used to find the final number of isomeric ions incident in the run.

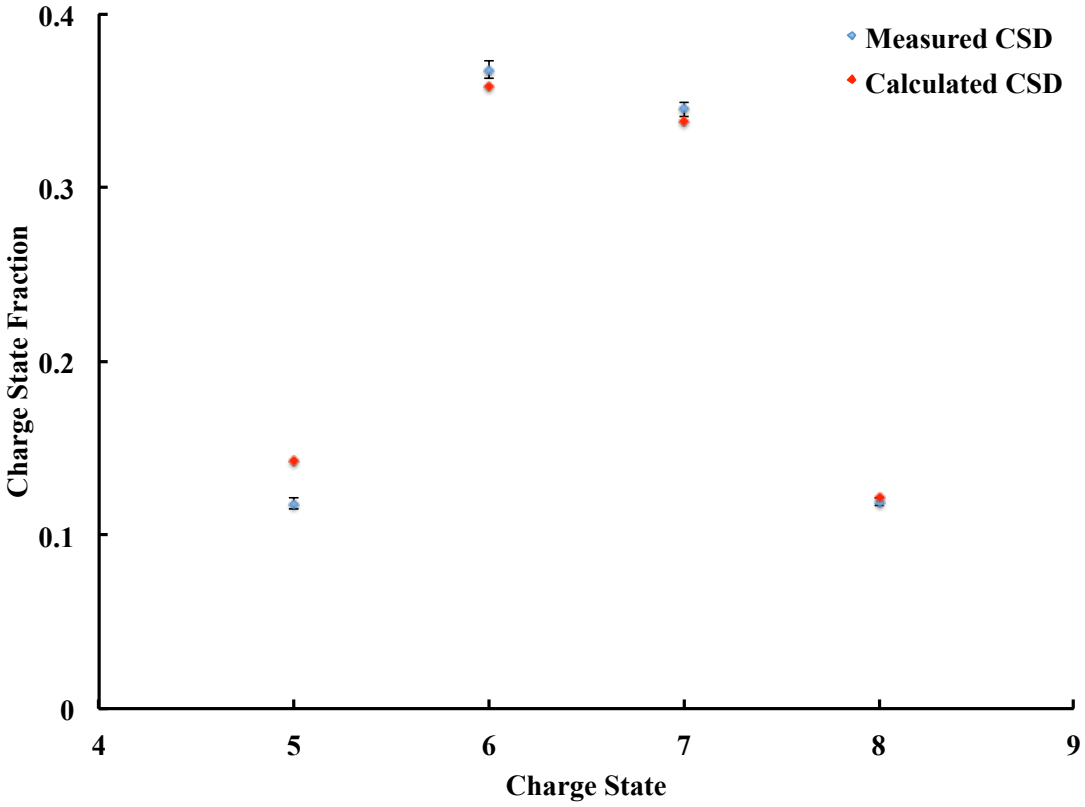

Figure 6.9 *Charge state distribution as measured by DRAGON optics (blue points) and calculated (red points).*

The efficiency of the NaI detectors was calculated through a GEANT4 simulation to be $4.3(2)\times10^{-6}$, assuming an impact point of 1.75 cm from the centre of the slits

and a 3.3 μm implantation depth. The point of impact is thought to be around 1.75 cm from the centre of the slits, however variations from 1.1 to 2.4 cm were investigated. The results were found to be consistent across this range.

Further tests were performed to assess the effect of implantation depth in the slit. Energy loss calculations imply an implantation depth of 3.3 μm into the slit and simulations performed at 1 μm either side of this also showed consistency.

6.4 Results

The final beam intensities are given in table 6.2. It is shown that there are, in general, more ground state ions than isomeric ions in the beam by a factor of around 1-2$\times 10^4$, as it is delivered to the target. Runs were excluded where no counts were recorded in the NaI detectors. These measurements aided the analysis of observed events which suggest a resonance strength of $\sim$400 meV. Given the low relative intensity of isomeric ions in the beam, however, it is possible that the measured counts are dominated by the ground state ℓ_p=4 resonance at E_r=446 keV. As such, further studies are planned to measure the strength of this ground state resonance to clarify the source of the observed events.

Table 6.2 *Number of incident ions of total ^{26}Al and ^{26m}Al for each set of runs with constant beam energy and target pressure. Runs are excluded where there are no counts in either the surface barrier or sodium iodide detectors.*

				^{26}Al		^{26m}Al	
Run Span	Runs Excluded	E_{beam} (keV/u)	Pressure (T)	$N_p(\times 10^{14})$	Intensity (pps$\times 10^9$)	$N_p \times 10^{10}$	Intensity (pps $\times 10^5$)
24592-24598	24595,24598	389.79	7	0.137(1)	1.82		
24795-24814	none	455.75	5	1.911(6)	3.17	1.13(6)	1.87
24733-24753	none	458.5	5	2.133(7)	3.41	1.29(6)	2.06
24777-24792	24777	459.1	5	1.681(7)	3.50	1.05(5)	2.18
24688-24732	24704-24706	469.4	5	4.242(9)	3.28	2.7(1)	2.07
24606-24687	24610,24677	469.4	7	5.235(9)	2.35	3.2(2)	1.42
24758-24776	none	469.35	5	1.996(6)	3.92	1.22(6)	2.40
24815-24862	none	484.19	4	4.760(9)	3.37	3.1(2)	2.22

Chapter 7

Conclusions, Current Status and the Future

7.1 Further Study of the $^{18}\mathrm{F}(\mathrm{p},\alpha)^{15}\mathrm{O}$ Reaction

New data have been obtained in the study of the astrophysically important ^{18}F(p,α)^{15}O reaction, relevant to gamma-ray production in novae. An R-matrix analysis has been performed to deduce the parameters of states causing resonant structures in measured excitation functions. A well-known resonance was clearly identified at $E_{c.m.}$=665 keV (E_x=7076 keV) and the parameters of seven more resonances were extracted, including those populated by low angular momentum transfers which are of most astrophysical importance. The results are consistent with a recent prediction and measurement of a broad $^1/_2{}^+$ state at an excitation of $\sim$7.866 MeV in ^{19}Ne, $E_{c.m.}$=1.455 MeV. The existence of this state supports the Generator Coordinate Method prediction of another broad state at sub-threshold energies, contributing significantly at novae temperatures. The inclusion of this resonant contribution is independent of the unknown strengths arising from several $J^\pi = {}^3/_2{}^+$ states, the interference between which generates a large uncertainty. Hence, the reaction rate at astrophysical temperatures is further constrained to relatively high values, resulting in a lower abundance of ^{18}F in nova ejecta and a consequent reduced detectability distance for these events. This work has been published in the Physical Review C journal [1].

Ultimately, it is crucial that studies of this reaction continue towards the

observation and parameterisation of the sub-threshold resonance predicted by Dufour and Descouvemont [57]; accurate and adequately constrained reaction rates will not be possible until this has been achieved. The observation of the higher-energy predicted resonance here, which has since been confirmed by Adekola *et al.* [125], has inferred its existence and provides the motivation required to begin further sub-threshold studies. Possible routes to this end include the development of higher intensity ^{15}O beams allowing elastic scattering with α-particles, and indeed such a proposal has recently been submitted to the TRIUMF PAC. Neutron pick-up using a beam of ^{18}Ne is also suggested. Alternatively, further direct measurements of the reaction s-factor at low-energy could constrain the reaction rate if run for an adequate period of time.

The importance of this observation has been enhanced further by the recent work of Laird *et al.* [126] where the low energy resonances previously thought to have $J^{\pi}=3/2^{+}$ do not show angular distributions consistent with such an assignment. The resonance previously understood to be $J^{\pi}=3/2^{+}$ and observed at $E_{c.m.}$=38 keV is now observed at $E_{c.m.}$=48 keV with $J^{\pi}=5/2^{-}$. This has eliminated the previous uncertainty over interference effects between $J^{\pi}=3/2^{+}$ resonances in this region. As such, the contribution of the sub-threshold resonance predicted by Dufour and Descouvemont is now of greatest importance of all.

7.2 Present Status of the ^{18}O(p,α)^{15}N reaction

New data have been studied from a direct measurement of the ^{18}O(p,α)^{15}N reaction, relevant to a discrepancy in the observed ^{14}N/^{15}N ratio and occurring during hydrogen burning in the evolution of population I stars. An *R*-matrix analysis has placed constraints on the broad $1/2^{+}$ resonance thought to dominate the reaction rate at these temperatures, as well as two further resonances in the vicinity. These results remain preliminary as further data sets are awaiting analysis at further angles and to higher energies.

While this direct measurement agrees with the new lower energy found in a recent Trojan Horse study [78] of this reaction, doubt is placed on the precision achieved in that work. Further analysis to come is likely to adequately address these doubts. The difficulty in constraining this broad state leaves a significant range of possible reaction rates. A higher rate, as allowed by this study, would result in a greater abundance of ^{15}N and possibly providing better agreement between

the observed $^{14}N/^{15}N$ ratio and predictions from nucleosynthesis simulations.

Furthermore, this reaction has proved useful in the normalisation of similar reaction studies. There are data available up to around 2 MeV above the proton threshold and this will be analysed to constrain the energy level structure of ^{19}F for reference in future experiments.

This work will lead to a publication by Mountford *et al.*

7.3 Consolidation of the R-Matrix Formalism

The R-Matrix formalism is an extremely important tool in the study of nuclear astrophysics, both in extraction of experimental parameters from data and extrapolation of cross sections to an experimentally challenging region. Three codes used to implement the formalism have been tested through the analysis of data obtained in this thesis on the study of the astrophysically important $^{18}F(p,\alpha)^{15}O$ reaction [1]. It has been demonstrated that the parameters extracted from these codes are broadly consistent, as well as the excellent agreement between cross-section and S-factor calculations. A minor discrepancy relating to the interference of a broad $^1/_2{}^+$ resonance with $^5/_2{}^+$ resonances in the vicinity has been resolved. Given the importance of the formalism in the extraction and interpretation of experimental parameters, this is a welcome development for research in this area, adding further confidence to results from the past and those to come in the future.

A publication of this work is in progress by Mountford *et al.*

7.4 Present Status of the $^{26m}Al(p,\gamma)^{27}Si$ Analysis

The first direct measurement of the $^{26m}Al(p,\gamma)^{27}Si$ reaction has been carried out at the TRIUMF laboratory to provide constraints on its rate for the interpretation of its contribution to stellar destruction of ^{26}Al. In this thesis the integrated intensity of the isomeric component of the ^{26}Al beam has been measured through the counting of γ-rays characteristic of the β^+ decay to the ground state of ^{26}Mg. It has been found that around one to two in every 10^4 ions was in the isomeric state.

This information is now being used by the collaboration leader to estimate the strength of a resonance thought to dominate the reaction rate. This further analysis is currently on hold while an additional study of the contributions from the ground state channel is performed.

Upon completion of these further measurements a publication will follow by Lotay, Mountford and Ruiz *et al.*

Appendix A

Energy Loss and Conversion Tables

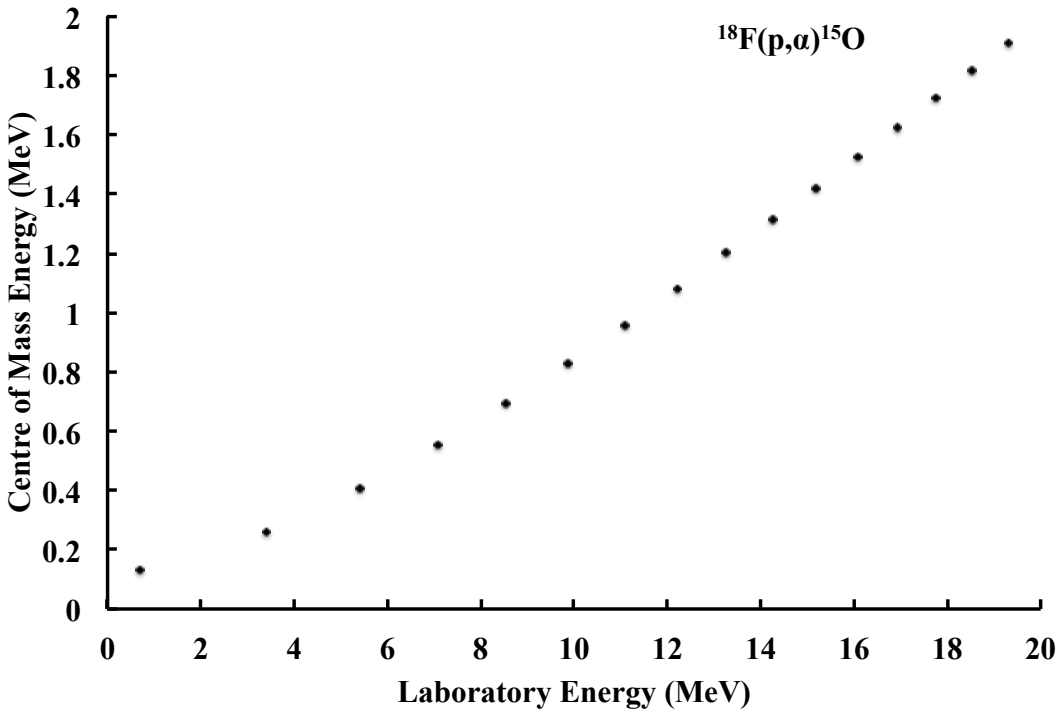

Figure A.1 *Beam energy in the centre of mass frame as a function of α-particle event energy in the $^{18}F(p,\alpha)^{15}O$ reaction for events detected at 4.08° to the beam axis.*

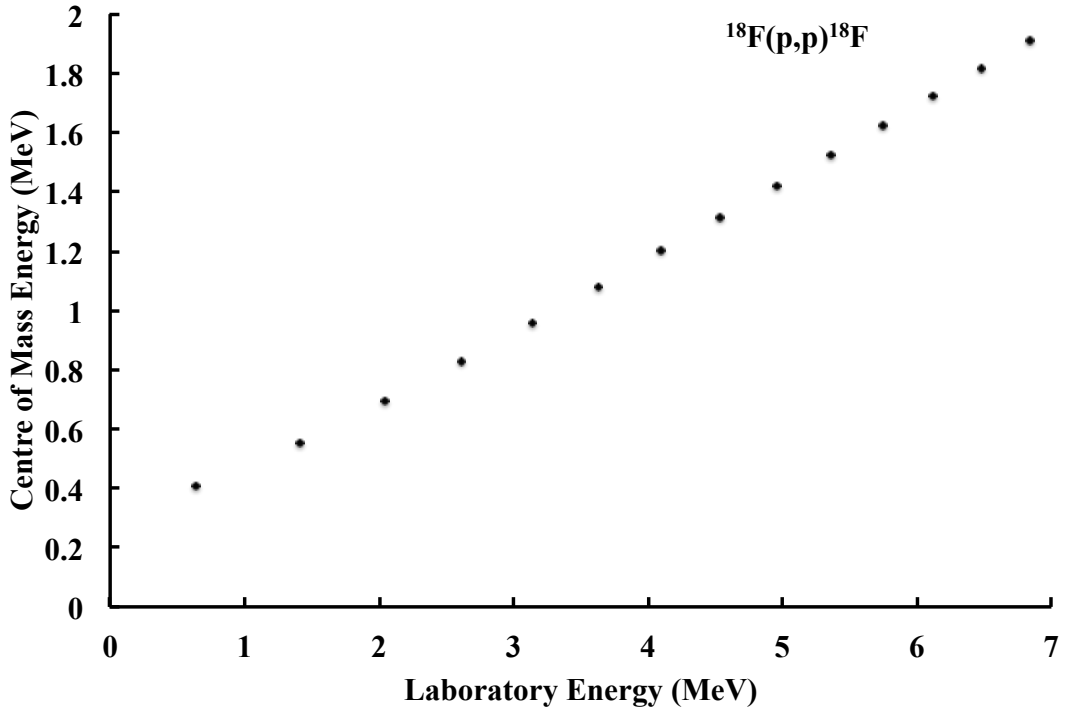

Figure A.2 *Beam energy in the centre of mass frame as a function of proton event energy in the $^{18}F(p,p)^{18}F$ reaction for events detected at 4.08° to the beam axis.*

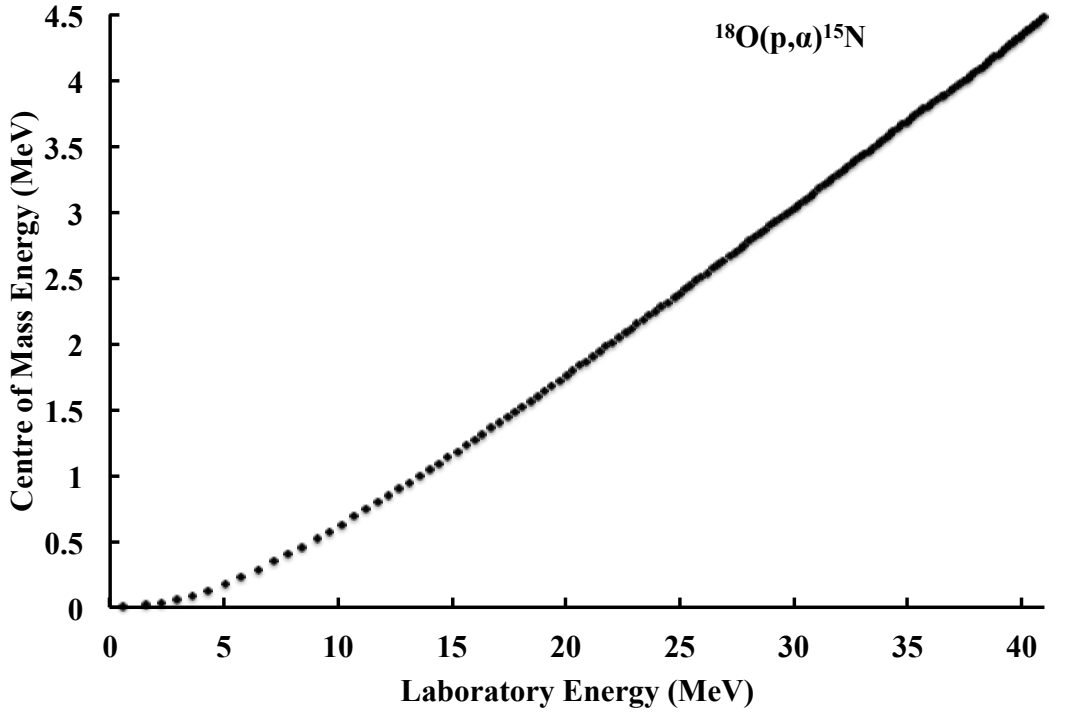

Figure A.3 *Beam energy in the centre of mass frame as a function of α-particle event energy in the $^{18}O(p,\alpha)^{15}N$ reaction for events detected at 8.44° to the beam axis.*

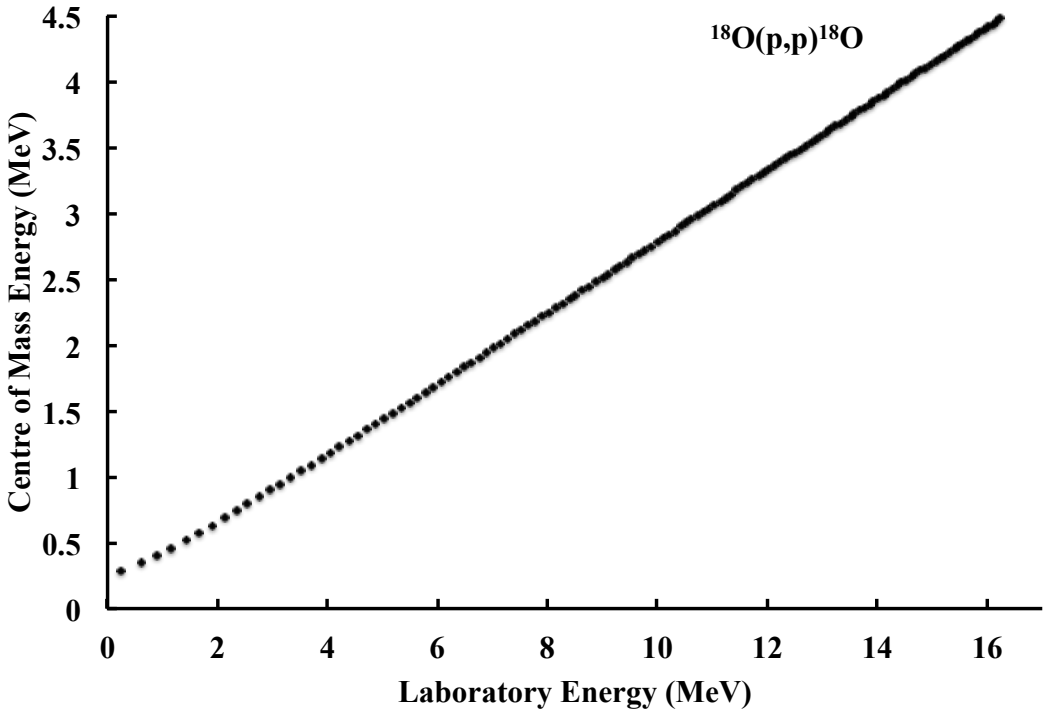

Figure A.4 *Beam energy in the centre of mass frame as a function of proton event energy in the $^{18}O(p,p)^{18}O$ reaction for events detected at 8.44° to the beam axis.*

Appendix B

Silicon Strip Detectors

B.1 Semiconductors

Materials can be labelled according to how current flows through them when an electric field is applied. Insulators do not allow current to flow, conductors allow current to flow freely while semiconductors allow current to flow in certain conditions. This can be explained by the band structure of solids.

B.1.1 Band Structure

The band structure, as shown in figure B.1, defines the location of electrons in a lattice in terms of their ability to flow in a current. The valence band is the location of the most external shell of electrons in an atom, defined by the group of the periodic table in which the material appears. If the electron is in the conduction band, that is, it is free to move in the presence of an electric field, a current can flow. In the case of metals, these bands overlap and a current can always flow, while in the case of insulators there is a large band gap (E_g) between the valence and conduction bands. Hence, the electrons are bound to the lattice and cannot flow in the presence of an electric field. The Fermi level defines the maximum energy level available to an electron at absolute zero temperature.

A semiconductor exists as something of an in-between. There exists a band gap, meaning that in the absence of an external energy to excite the electron no current can flow. This band gap, however, is relatively small compared to insulators and

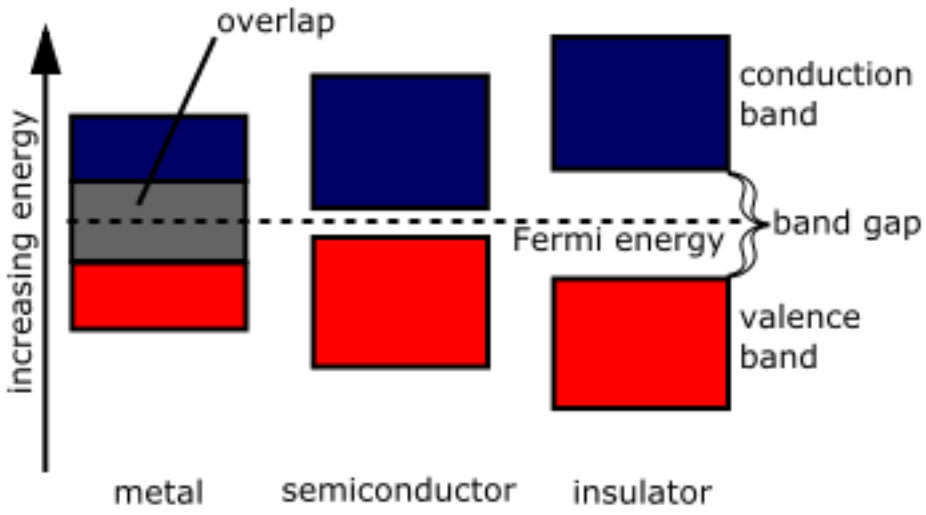

Figure B.1 *The band structure of conductors, semiconductors and insulators [127].*

it is possible that an electron could be excited into the conduction band, leaving a hole behind in the valence band, such that a current could flow. As an example, Germanium has a band gap of 0.67 eV and Silicon has a band gap of 1.12 eV [128]. The probability of an electron being thermally excited into the conduction band is governed by the Boltzmann distribution:

$$P \propto e^{\frac{-E_g}{kT}}. \tag{B.1}$$

B.1.2 Doping

In a pure lattice structure of a group IV material, each atom will be bound to another by four bonds. If one of these atoms were to be replaced by a group V material, there would then be one spare electron less tightly bound to the lattice than previously. This is referred to as n-type doping and has the effect of creating an additional band around 0.01 eV below the conduction band meaning less ionising energy is required to excite the electron into the conduction band.

Alternatively, if the lattice is doped by a group III material, the lattice becomes p-doped. In this case the dopant must 'borrow' an electron from another atom in the lattice, leaving an unfilled hole somewhere in the lattice. As such, an 'acceptor' band appears around 0.01 eV above the valence band.

B.1.3 Depletion Zone and Biasing

When p-type and n-type material are brought into contact, the donor electrons in the n-type material diffuse across to the acceptors in the p-type material. As this diffusion takes place, the electric field from the already moved carriers offsets its effect, leaving behind a depletion zone, as shown in figure B.2. This zone is (almost) completely devoid of free charge carriers, leaving behind only the atomic cores in the lattice and is within a 'built-in potential' formed between the p and n-type regions. Any charge carriers in the depletion zone will be swept out by this potential.

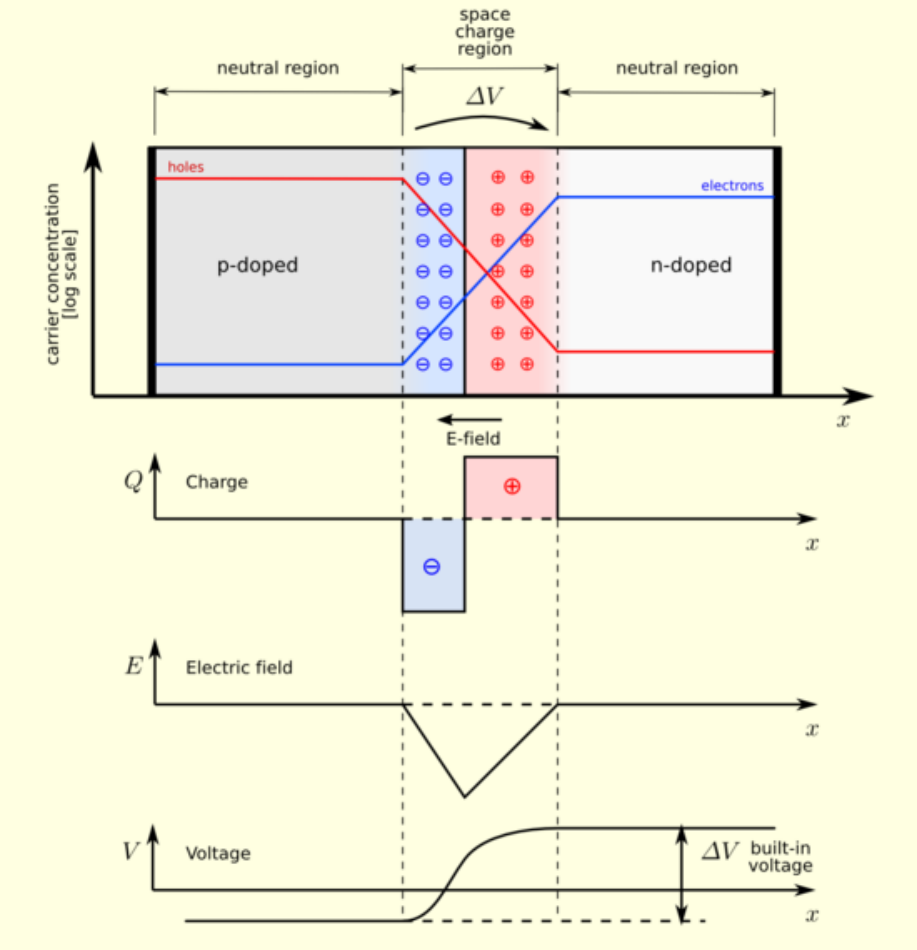

Figure B.2 *The formation of a depletion zone in a pn-junction and the associated built in electric field. [129]*

Placing a bias across the junction can then have one of two effects. If the positive anode is applied to the p-type material and the negative cathode is placed on the n-type material then the free holes and electrons will move back to their original positions due to the electric field. This has the effect of closing the depletion zone

and making the formation of electron-hole pairs more likely.

Alternatively, reversing the bias into 'reverse bias mode' has the opposite effect. As the bias is increased more and more charge carriers diffuse across the junction, increasing the size of the depletion zone. This reduces the flow of charge carriers in the depletion region, reducing the current and making it less likely that an electron-hole pair could be randomly excited into the depletion zone by the environment. Incident radiation of high enough energy then excites an electron hole pair which is quickly swept out by this applied bias providing a current to the anode and cathode. The number of electron-hole pairs formed is then related to the energy of the incoming radiation.

Quenching

Quenching refers to the effect of some of the energy deposited by an incoming charged particle not contributing to the energy signal. This energy can be "lost" through a few processes including recombination of the electron-hole pairs prior to being swept out by the applied bias or nuclear stopping effects not contributing to the yield of electron-hole pairs [130]. Different particles are quenched at different rates, dependant upon their charge. In the two cases discussed in this thesis, the studies of ^{18}F(p,α)^{15}O and ^{18}O(p,α)^{15}N, detectors were calibrated using α-particles, which are quenched more than protons. As a result, a factor of 0.986 is applied to the detected energy of the protons, accounting for this effect, to find the true energy of the incident particle [131].

B.2 Silicon Detectors

The most commonly used detectors throughout this thesis were silicon detectors provided by Micron Semiconductors Ltd. [82]. The bulk of the detector is a silicon crystal wafer, usually with impurities making it slightly n-type.

B.2.1 Single Sided

An example of a single sided silicon detector is the LEDA detector used in the study of the ^{18}O(p,α)^{15}N reaction [89]. Typically, the silicon wafer is first cleaned

and the front side coated in a thermal oxide which is etched to open a clean silicon surface in the required design. In the case of LEDA, the wafer is a segment of a circle and the etched areas are rings on that circle. The wafer is then doped; Phosphorus on the back to provide n-type doping and boron in the etched areas on the front to provide p-type doping. The etched areas on the front and the whole back surface are then aluminised for electrical contacts.

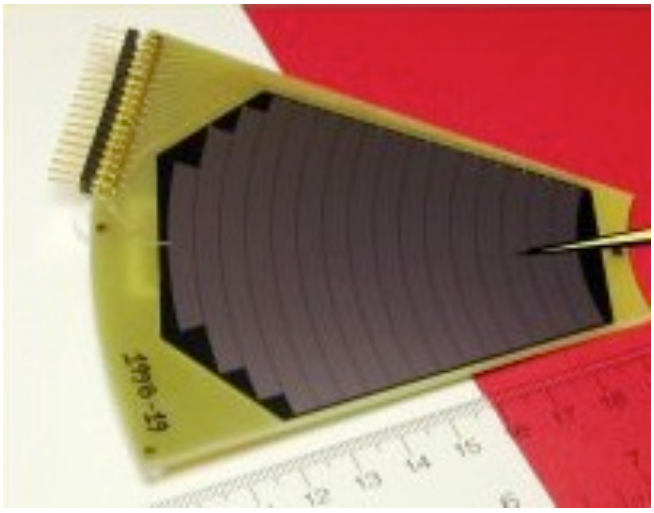

Figure B.3 *The MSL type-YY1 detector, a single LEDA segment [132].*

The depletion layer is formed in the bulk material while the aluminised and doping layers are considered dead layers, where the incident particle loses energy but does not contribute to the signal.

B.2.2 Double Sided

An example of a double sided silicon strip detector is that used in the study of the ^{18}F(p,α)^{15}O reaction presented here, the MSL type-W detector [82], shown in figure B.5. The manufacturing process is similar to that for single sided detectors but the backside of the bulk is also etched with the n-type doping only applied to the etched areas. In the case of the type-W used here the etching is in strips on both sides perpendicular to each other. This gives a pixelated effect when taking signals from the detector.

As the n-doped back side will form an n^+-n-n^+ structure when etched, additional isolation must be provided to avoid a current passing between strips. Usually a p-region is introduced in between the n-type strips to provide this isolation, as shown in figure B.4.

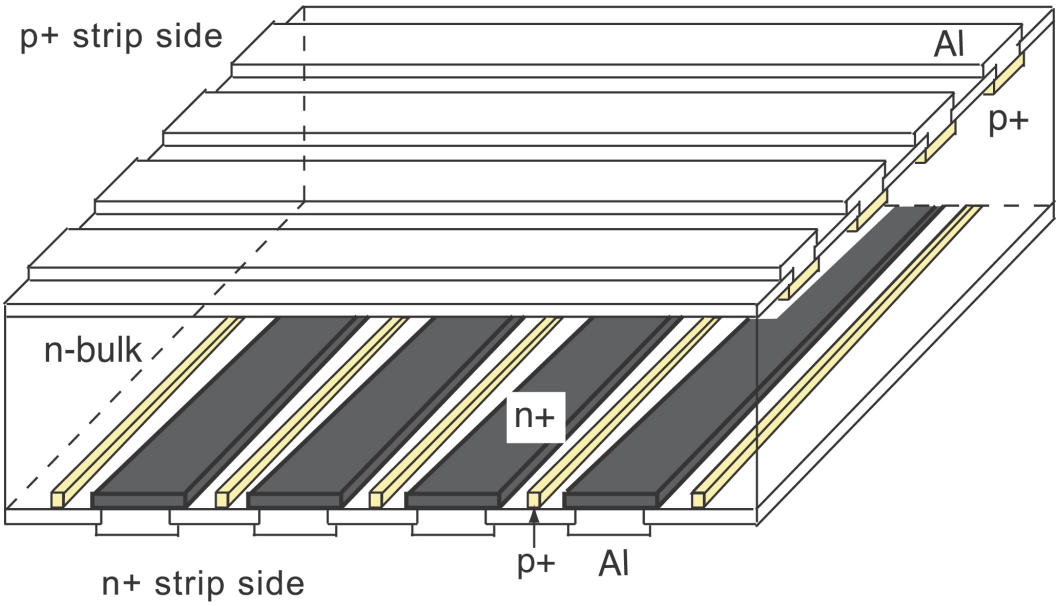

Figure B.4 *Schematic diagram of a double sided silicon strip detector. [133]*

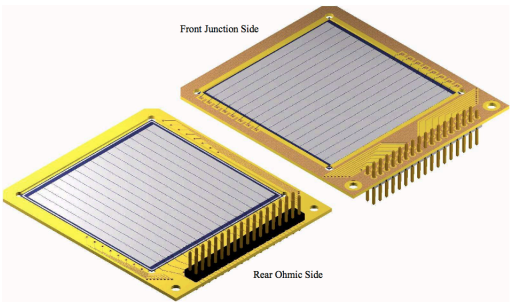

Figure B.5 *The MSL type-W detector.[134]*

Bibliography

[1] D. J. Mountford *et al. Physical Review C*, 85:022801, 2012.

[2] D. D. Clayton. *The Astrophysical Journal*, 280:144–149, 1984.

[3] A. Coc *et al. Astronomy and Astrophysics*, 357:561–571, 2000.

[4] W. A. Mahoney *et al. The Astrophysical Journal*, 262:742, 1982.

[5] H. N. Russell. *Popular Astronomy*, 22, 1914.

[6] http://chandra.harvard.edu/graphics/edu/formal/variable_stars/HR_diagram.jpg.

[7] R. A. Alpher *et al. Physical Review*, 73:803–804, 1948.

[8] http://cosmology.berkeley.edu/Education/CosmologyEssays/images/BBNS_vs_t.gif.

[9] http://www.einstein-online.info/images/spotlights/BBN_physI/reactions.gif.

[10] J. José and C. Iliadis. *Reports on Progress in Physics*, 74:069601, 2011.

[11] C. E. Rolfs and W. S. Rodney. *Cauldrons in the Cosmos: Nuclear Astrophysics*. University of Chicago Press, 1988.

[12] C Iliadis. *Nuclear Physics of Stars*. Wiley-VCH, 2007.

[13] D. Prialnik. *An Introduction to the Theory of Stellar Structure and Evolution*. Cambridge University Press, 2009.

[14] J. H. Williams *et al. Physical Review*, 51:888–889, 1937.

[15] H. A. Bethe. *Physical Review*, 55:434–456, 1939.

[16] J. B. Marion and W. A. Fowler. *The Astrophysical Journal*, 125:221, 1957.

[17] http://www.nndc.bnl.gov/nudat2/.

[18] F. Hoyle. *The Astrophysical Journal Supplement*, 1:121, 1954.

[19] C. W. Cook *et al. Physical Review*, 107:508–515, 1957.

[20] M. Chernykh *et al. Physical Review Letters*, 98:032501, 2007.

[21] Hans O. U. Fynbo and Martin Freer. *Physics*, 4:94, 2011.

[22] E. M. Burbidge *et al. Review of Modern Physics*, 29:547–650, 1957.

[23] http://astronomyonline.org/Stars/Images/EvolutionNormalStar_th.jpg.

[24] S. Chandrasekhar. *The Astrophysical Journal*, 74:81, 1931.

[25] http://www.scienceinschool.org/repository/images/issue5fusion2_large.jpg.

[26] J. S. Gallagher and S. Starrfield. *Annual Review of Astronomy and Astrophysics*, 16:171–214, 1978.

[27] http://astronomy.swin.edu.au/cms/cpg15x/albums/userpics/rochelobe1.jpg.

[28] http://www.nasa.gov/images/content/62486main_Making_a_Nova.jpg.

[29] http://apod.nasa.gov/apod/image/novaCygni_hst.gif.

[30] M. Kromer *et al. The Astrophysicial Journal*, 719:1067, 2010.

[31] http://sci.esa.int/science-e media/img/51/Integral%20wallpaper.jpg.

[32] http://integral.esac.esa.int/integ_spectrometer_annotated.gif.

[33] M. Hernanz *et al. The Astrophysical Journal Letters*, 526(2):L97, 1999.

[34] J. José *et al. Nuclear Physics A*, 777:550 – 578, 2006.

[35] R. Diehl *et al. Astronomy and Astrophysics*, 298:445, 1995.

[36] R. Diehl *et al. Nature*, 439:45–47, 2006.

[37] E. Zinner. *Annual Review of Earth and Planetary Sciences*, 26:147, 1998.

[38] http://mis.triumf.ca/science/experiment/view/95.

[39] S. Palmerini *et al. ApJ.*, 764:128, 2013.

[40] G. Gamow. *Zeitschrift fur Physik*, 41:204, 1928.

[41] G. Breit and E. Wigner. *Physical Review*, 49:519–531, 1936.

[42] M. Aliotta. In *International Workshop on Nuclear Astrophysics*, 2011.

[43] Thomas Rauscher. *Physical Review C*, 81:045807, 2010.

[44] A. M. Lane and R. G. Thomas. *Review of Modern Physics*, 30(2):257–353, 1958.

[45] A. D. Roberts *et al. Nuclear Instruments and Methods in Physics Research B*, 103:523–528, 1995.

[46] R. Coszach *et al. Physics Letters B*, 353(2-3):184 – 188, 1995.

[47] K. E. Rehm *et al. Physical Review C*, 52:R460–R463, 1995.

[48] K. E. Rehm *et al. Physical Review C*, 53(4):1950–1954, 1996.

[49] D. W. Bardayan *et al. Physical Review C*, 63(6):065802, May 2001.

[50] F. Ajzenberg-Selove. *Nuclear Physics A*, 475(1):1 – 198, 1987.

[51] S. Utku *et al. Physical Review C*, 57(5):2731–2739, 1998.

[52] J. S. Graulich *et al. Nuclear Physics A*, 626(3):751 – 759, 1997.

[53] D. W. Bardayan *et al. Physical Review Letters*, 89(26):262501, 2002.

[54] C. D. Nesaraja *et al. Physical Review C*, 75(5):055809, 2007.

[55] H. T. Fortune and R. Sherr. *Physical Review C*, 73(2):024302, 2006.

[56] A. StJ. Murphy *et al. Physical review C*, 79(5):058801, May 2009.

[57] M. Dufour and P. Descouvemont. *Nuclear Physics A*, 785(3-4):381 – 394, 2007.

[58] C. Iliadis *et al. Nuclear Physics A*, 841(1-4):251 – 322, 2010.

[59] D. W. Bardayan *et al. Physical Review C*, 70(1):015804, Jul 2004.

[60] M. Dufour and P. Descouvemont. *Nuclear Physics A*, 750:218 – 231, 2005.

[61] J. C. Dalouzy *et al. Physical Review Letters*, 102(16):162503, 2009.

[62] N. de Séréville *et al. Nuclear Physics A*, 758:745 – 748, 2005.

[63] K. Y. Chae *et al. Physical Review C*, 74(1):012801, 2006.

[64] N. De Séréville *et al. Physical Review C*, 79(1):015801, Jan 2009.

[65] C. E. Beer *et al. Physical Review C*, 83(4):042801, Apr 2011.

[66] A. S. Adekola *et al. Physical Review C*, 83(5):052801, 2011.

[67] C. Angulo *et al. Nuclear Physics A*, 656(1):3 – 183, 1999.

[68] M. Wiescher *et al. Nuclear Physics A*, 349(12):165 – 216, 1980.

[69] C. Schmidt and H.H. Duhm. *Nuclear Physics A*, 155(2):644 – 658, 1970.

[70] A.E. Champagne and M.L. Pitt. *Nuclear Physics A*, 457(2):367 – 374, 1986.

[71] D.R. Tilley *et al. Nuclear Physics A*, 595(1):1 – 170, 1995.

[72] R. R. Carlson *et al. Phys. Rev.*, 122:607–616, 1961.

[73] K. Yagi *et al. Journal of the Physical Society of Japan*, 17:595, 1962.

[74] H.-B. Mak *et al. Nuclear Physics A*, 304(1):210 – 220, 1978.

[75] H. Lorenz-Wirzba *et al. Nuclear Physics A*, 313(3):346 – 362, 1979.

[76] M. La Cognata *et al. The Astrophysical Journal*, 708:796, 2010.

[77] M. La Cognata *et al. Journal of Physics G: Nuclear and Particle Physics*, 35:014014, 2008.

[78] M. La Cognata *et al. The Astrophysical Journal*, 723:1512, 2010.

[79] A Navin *et al. Journal of Physics G: Nuclear and Particle Physics*, 38(2): 024004, 2011.

[80] http://www.ganil spiral2.eu/.

[81] J. F. Ziegler *et al. The Stopping and Range of Ions in Matter*. 1985.

[82] http://www.micronsemiconductor.co.uk/.

[83] A. M. Baldin *et al. Kinematics of Nuclear Reactions*. Pergamon Press, 1961.

[84] http://www.ftssystems/rschillerback.htm.

[85] M. Duval *et al. IEEE Transactions on Magnetics*, 32(4):2194 –2196, 1996.

[86] http://www.hamamatsu.com/.

[87] C. Angulo *et al. Physical Review C*, 67:014308, 2003.

[88] http://tuda.triumf.ca/, .

[89] T. Davinson *et al. Nuclear Instruments and Methods in Physics Research A*, 454(23):350 – 358, 2000.

[90] O.B. Tarasov and D. Bazin. *Nuclear Instruments and Methods in Physics Research B*, 204:174–178, 2003.

[91] E. Steinbauer *et al. Nuclear Instruments and Methods in Physics Research A*, 339(1-2):102 – 108, 1994.

[92] P Descouvemont and D Baye. *Reports on Progress in Physics*, 73:036301, 2010.

[93] P. Descouvemont *et al. Atomic data and Nuclear Data Tables*, 88(1):203 – 236, 2004.

[94] R. E. Azuma *et al. Physical Review C*, 81:045805, 2010.

[95] http://wwwasdoc.web.cern.ch/wwwasdoc/minuit/minmain.html.

[96] http://pntpm3.ulb.ac.be/Nacre/barre_database.htm.

[97] R. B. Wiringa *et al. Physical Review C*, 51:38–51, 1995.

[98] V. G. J. Stoks *et al. Physical Review C*, 48:792–815, 1993.

[99] R. Roth *et al. Progress in Particle and Nuclear Physics*, 65(1):50 – 93, 2010.

[100] J.S. Lilley. *Nuclear physics: principles and applications*. Wiley-Blackwell, 2001.

[101] P Descouvemont. *Private Communication*, 2011.

[102] E. Uberseder. *Private Communication*, 2012.

[103] M. Abramowitz and I. A. Stegun. *Handbook of Mathematical Functions with Formulas, Graphs, and Mathematical Tables*. Courier Dover Publications, 1964.

[104] R. G. Thomas. *Physical Review*, 81:148–149, 1951.

[105] C. R. Brune. *Physical Review C*, 66:044611, 2002.

[106] F. C. Barker. *Australian Journal of Physics*, 25:341, 1972.

[107] http://www.netlib.org/lapack/.

[108] http://www.gnu.org/software/gsl/.

[109] L. Buchmann *et al. Nuclear Physics A*, 415(1):93 – 113, 1984.

[110] C. Ruiz *et al. Physical Review Letters*, 96:252501, 2006.

[111] C. M. Deibel *et al. Physical Review C*, 80:035806, 2009.

[112] G. Lotay *et al. Physical Review C*, 80:055802, 2009.

[113] G. Lotay *et al. Physical Review Letters*, 102:162502, 2009.

[114] G. Lotay *et al. Physical Review C*, 84:035802, 2011.

[115] A. Parikh *et al. Physical Review C*, 84:065808, 2011.

[116] I-Yang Lee. *Nuclear Physics A*, 520(0):c641 – c655, 1990.

[117] https://mis.triumf.ca/science/experiment/view/S1204.

[118] P.M. Endt. *Nuclear Physics A*, 633(1):1 – 220, 1998.

[119] P. Bricault *et al. Nuclear Instruments and Methods in Physics Research B*, 204(0):319 – 324, 2003.

[120] R.E. Laxdal. *Nuclear Instruments and Methods in Physics Research B*, 204 (0):400 – 409, 2003.

[121] J.M. D'Auria. *Nuclear Physics A*, 701(14):625 – 631, 2002.

[122] D. A. Hutcheon *et al. Nuclear Instruments and Methods in Physics Research A*, 498:109–210, 2003.

[123] C. Vockenhuber *et al. Physical review C*, 76:035801, 2007.

[124] S. Bishop. *Direct Measurements Of The $^{21}Na(p,\gamma)^{22}Mg$ Resonant Reaction Rate In Nova Nucleosynthesis*. PhD thesis, Simon Fraser University, 2003.

[125] A. S. Adekola *et al. Physical Review C*, 85:037601, 2012.

[126] A. M. Laird *et al. Physical Review Letters*, 110:032502, 2013.

[127] http://upload.wikimedia.org/wikipedia/commons/thumb/0/0b/Band_gap_comparison.svg/350px Band_gap_comparison.svg.png.

[128] H. Spieler. *Semiconductor Detector Systems*. Oxford University Press, 2005.

[129] https://upload.wikimedia.org/wikipedia/commons/thumb/f/fa/Pn-junction-equilibrium-graphs.png/550px-Pn-junction-equilibrium graphs.png.

[130] V. B. Ndocko-Ndongue *et al. Journal of Physics C: Solid State Physics*, 11: 1733, 1978.

[131] T. Davinson. *Private Communication*, 2010.

[132] http://tuda.triumf.ca/, .

[133] http://spie.org/Images/Graphics/Newsroom/Imported/0889/0889_fig1.jpg.

[134] http://www.micronsemiconductor.co.uk/pdf/w1.pdf.